Office of Naval Research

Contract N00014-89-J-1023
Contract N00014-89-J-1565
National Sciences Foundation Grant DMR-84-04489
National Sciences Foundation Grant DMR-86-14003
National Sciences Foundation Grant DMR-89-12927

DYNAMICAL PROPERTIES OF TWO-DIMENSIONAL JOSEPHSON JUNCTION ARRAYS

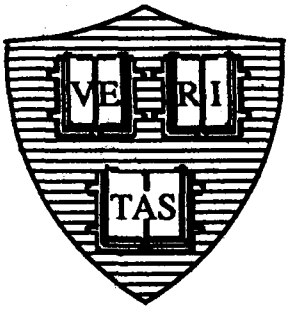

By

Samuel Paul Benz

May 1990

Technical Report No. 29

Division of Applied Sciences
Harvard University · Cambridge, Massachusetts

REPORT DOCUMENTATION PAGE

Form Approved
OMB No. 0704-0188

1a. REPORT SECURITY CLASSIFICATION Unclassified	1b. RESTRICTIVE MARKINGS None
2a. SECURITY CLASSIFICATION AUTHORITY N/A	3. DISTRIBUTION/AVAILABILITY OF REPORT Unclassified/Unlimited
2b. DECLASSIFICATION/DOWNGRADING SCHEDULE N/A	
4. PERFORMING ORGANIZATION REPORT NUMBER(S) Technical Report No. 29	5. MONITORING ORGANIZATION REPORT NUMBER(S)
6a. NAME OF PERFORMING ORGANIZATION Harvard University 6b. OFFICE SYMBOL (If applicable) N/A	7a. NAME OF MONITORING ORGANIZATION Office of Naval Research
6c. ADDRESS (City, State, and ZIP Code) Division of Applied Sciences Harvard University Cambridge, MA 02138	7b. ADDRESS (City, State, and ZIP Code) 800 N. Quincy Street Arlington, VA 22217
8a. NAME OF FUNDING/SPONSORING ORGANIZATION Office of Naval Research 8b. OFFICE SYMBOL (If applicable)	9. PROCUREMENT INSTRUMENT IDENTIFICATION NUMBER N00014-89-J-1023
8c. ADDRESS (City, State, and ZIP Code) 800 N. Quincy Street Arlington, VA 22217	10. SOURCE OF FUNDING NUMBERS PROGRAM ELEMENT NO. / PROJECT NO. / TASK NO / WORK UNIT ACCESSION NO.
11. TITLE (Include Security Classification) Dynamical Properties of Two-Dimensional Josephson Junction Arrays	
12. PERSONAL AUTHOR(S) Samuel Paul Benz	
13a. TYPE OF REPORT 13b. TIME COVERED FROM _____ TO _____	14. DATE OF REPORT (Year, Month, Day) May 1990 15. PAGE COUNT 146
16. SUPPLEMENTARY NOTATION	

17. COSATI CODES			18. SUBJECT TERMS (Continue on reverse if necessary and identify by block number)
FIELD	GROUP	SUB-GROUP	

19. ABSTRACT (Continue on reverse if necessary and identify by block number)

We have investigated the dynamical properties of two-dimensional (2D) Josephson junction arrays at temperatures below the Kosterlitz-Thouless phase transition. We have completed a comprehensive study, based on experiments and simulations, of the effects of large direct (dc) and radio-frequency (rf) bias currents on 2D arrays in the presence of perpendicular magnetic fields. Experiments were performed on large 1000 by 1000 arrays of Nb-Cu-Nb proximity-effect junctions that were fabricated using various photolithographic and thin-film deposition techniques.

We present a complete explanation of the dynamic resistance in arrays as a function of both dc bias current and magnetic field. For certain fields, when the number of flux quanta per array unit cell is the ratio of two integers, the field-induced vortices are commensurate with the array and are arranged in ordered superlattices with qxq unit cells. Prominent peaks in the dynamic resistance are observed for these commensurate magnetic fields, and we relate the currents at these peaks with the

20. DISTRIBUTION/AVAILABILITY OF ABSTRACT ☐ UNCLASSIFIED/UNLIMITED ☐ SAME AS RPT. ☐ DTIC USERS	21. ABSTRACT SECURITY CLASSIFICATION Unclassified
22a. NAME OF RESPONSIBLE INDIVIDUAL	22b. TELEPHONE (Include Area Code) / 22c. OFFICE SYMBOL

19. ABSTRACT (continued)

depinning currents of the vortex superlattices. New exact calculations of the critical current are presented for the cases where f=1/2 and 1/3, which agree well with previous theoretical results and our experimental measurements.

When rf currents are applied to the 2D arrays in commensurate magnetic fields, novel fractional giant steps appear in the current-voltage curves at voltages, $V_n = n(N/q)h\nu/2e$, (where N = 1000 is the number of junctions in the direction of applied current) directly related to the vortex superlattice unit cell size, q. These steps are confirmed through computer simulations on arrays of resistively shunted Josephson junctions. We propose a phenomenological model to explain these novel steps, based on the locking of the motion of the vortex superlattices with the applied rf current, and, using simulations, we show that the detailed motion of the vortices is in agreement with the model.

We also present the results of simulations of positionally-disordered superconducting wire networks. We determined the critical field from the decay of oscillations in the calculated transition temperature as a function of magnetic field. This is found to be in excellent agreement with our experimental magnetoresistance measurements of positionally-disordered Josephson junction arrays.

Office of Naval Research

Contract N00014-89-J-1023
Contract N00014-89-J-1565
National Sciences Foundation Grant DMR-84-04489
National Sciences Foundation Grant DMR-86-14003
National Sciences Foundation Grant DMR-89-12927

DYNAMICAL PROPERTIES OF TWO-DIMENSIONAL JOSEPHSON JUNCTION ARRAYS

by

Samuel Paul Benz

Technical Report No. 29

May 1990

The research reported in this document was made possible through support extended the Division of Applied Sciences, Harvard University, by the Office of Naval Research, under Contracts N00014-89-J-1565, N00014-89-J-1023 and by the National Sciences Foundation Grants DMR-84-04489, DMR-86-14003, and DMR-89-12927.

Division of Applied Sciences
Harvard University · Cambridge, Massachusetts

ABSTRACT

We have investigated the dynamical properties of two-dimensional (2D) Josephson junction arrays at temperatures below the Kosterlitz-Thouless phase transition. We have completed a comprehensive study, based on experiments and simulations, of the effects of large direct (dc) and radio-frequency (rf) bias currents on 2D arrays in the presence of perpendicular magnetic fields. Experiments were performed on large 1000 by 1000 arrays of Nb-Cu-Nb proximity-effect junctions that were fabricated using various photolithographic and thin-film deposition techniques.

We present a complete explanation of the dynamic resistance in arrays as a function of both dc bias current and magnetic field. For certain fields, when the number of flux quanta per array unit cell is the ratio of two integers, the field-induced vortices are commensurate with the array and are arranged in ordered superlattices with qxq unit cells. Prominent peaks in the dynamic resistance are observed for these commensurate magnetic fields, and we relate the currents at these peaks with the depinning currents of the vortex superlattices. New exact calculations of the critical current are presented for the cases where f = 1/2 and 1/3, which agree well with previous theoretical results and our experimental measurements.

When rf currents are applied to the 2D arrays in commensurate magnetic fields, novel *fractional* giant steps appear in the current-voltage curves at voltages, $V_n = n(N/q)h\nu/2e$, (where N = 1000 is the number of junctions in the direction of applied current) directly related to the vortex superlattice unit cell size, q. These steps are confirmed through computer simulations on arrays of resistively shunted Josephson junctions. We propose a phenomenological model to explain these novel steps, based on the locking of the motion of the vortex superlattices with the applied rf current, and, using simulations, we show that the detailed motion of the vortices is in agreement with the model.

We also present the results of simulations of positionally-disordered superconducting wire networks. We determined the critical field from the decay of oscillations in the calculated transition temperature as a function of magnetic field. This is found to be in excellent agreement with our experimental magnetoresistance measurements of positionally-disordered Josephson junction arrays.

TABLE OF CONTENTS

LIST OF FIGURES

LIST OF TABLES

CHAPTER 1

INTRODUCTION TO 2D ARRAYS

1.1 Introduction

Next to the discovery of superconductivity itself, probably the most important contribution to the fields of superconductivity and superconducting electronics was the prediction of the Josephson effect by B. D. Josephson in 1962. Josephson predicted that pairs of electrons could tunnel between two closely-spaced superconductors so that a supercurrent could flow between them of magnitude

$$i = i_c \sin\gamma \,, \tag{1.1.1}$$

where γ is the phase difference between the macroscopic wave functions of the two superconductors, and the critical current, i_c, is the maximum supercurrent that will flow through the junction. He also predicted that the phase difference will change at a rate proportional to that voltage,

$$v = \frac{\hbar}{2e}\frac{d\gamma}{dt} \,. \tag{1.1.2}$$

Equations (1.1.1) and (1.1.2) are known as the Josephson equations, and they determine the superconducting properties of Josephson junctions.

Josephson junctions display interesting cooperative phenomena when they are connected together in a two-dimensional (2D) array. In the past, 2D arrays have been primarily used to study the statistical physics of phase transitions in two dimensions, and in

particular the Kosterlitz-Thouless phase transition (Kosterlitz and Thouless, 1973; Resnick *et al.*, 1981; Voss and Webb, 1982; and Abraham *et al.*, 1982). (For a review of 2D arrays see Lobb, 1984, and Mooij, 1983). With the recent advances in fabrication technology, including the ability to introduce controlled amounts of disorder (Forrester, 1988), 2D arrays have also been used as model systems to understand the behavior of granular superconductors. These particular properties of 2D arrays--the ability to model granular systems and to display the Kosterlitz-Thouless transition--have been used to interpret some of the properties of the newly discovered high transition-temperature copper-oxide superconductors (see Tinkham and Lobb, 1989).

Previous work has focused on the static properties or equilibrium phase transitions of 2D arrays, using small signals and temperatures very close to the phase transition temperature. The body of this report, however, will emphasize the *dynamical* properties of 2D Josephson junction arrays, including a detailed exploration of the collective response of 2D arrays to large dc and rf bias currents in the presence of magnetic fields. In this chapter, we will begin with a brief review of some of the concepts that are essential to understanding the physics of 2D arrays. These concepts include a simple model for a single Josephson junction (Section 1.2), the Kosterlitz-Thouless transition (Section 1.3), and the commensurability of applied perpendicular magnetic fields with the array of junctions (Section 1.4).

In Chapter 2, we will describe the fabrication process for making our SNS arrays, the experimental measurement circuits and setup, and some experimental details that will be important when we interpret the results in the following chapters. The dynamical properties of 2D arrays in the presence of a dc bias current and a perpendicular magnetic field will be described in Chapter 3. The experimental properties of arrays with an additional radio frequency (rf) bias current will be discussed in Chapter 4 and RSJ model simulations of dc and rf current-biased arrays in commensurate magnetic fields will be described in Chapter 5. Chapter 6 describes the results of Ginzburg-Landau calculations of

the T_c of positionally disordered 2D wire networks in a magnetic field and compares them with experimental magnetoresistance measurements on positionally disordered arrays. In Chapter 7 we will summarize the results from Chapters 3-6, and comment on their combined implications for the dynamical behavior of disordered 2D systems, and for possible applications of 2D arrays in high-frequency superconducting electronics.

1.2 The Resistively Shunted Junction Model

In order to understand the dynamics of 2D arrays, it is important to first understand single Josephson junctions. One of the best models for the Josephson junction is the resistively shunted junction (RSJ) model, which was proposed independently by Stewart (1968) and McCumber (1968). The RSJ model takes into account such physically important properties of real junctions as resistance and capacitance. It treats the Josephson junction as a parallel combination of elements: a resistor r_n, a capacitor C, and the non-linear Josephson element with a critical current i_c as described by (1.1.1). If the junction is current biased, the resulting circuit, shown schematically in Fig. 1.1a, can be described by the following equation

$$i_{bias} = i_c \sin\gamma + \frac{v}{r_n} + C\frac{dv}{dt}, \tag{1.2.1}$$

where γ is again the phase difference across the junction. Since the voltage across the junction is related to the rate of change of the phase from (1.1.2), we can rewrite (1.2.1) in dimensionless form as

$$\frac{i_{bias}}{i_c} = \sin\gamma + \frac{d\gamma}{d\tau} + \beta_c \frac{d^2\gamma}{d^2\tau}, \tag{1.2.2}$$

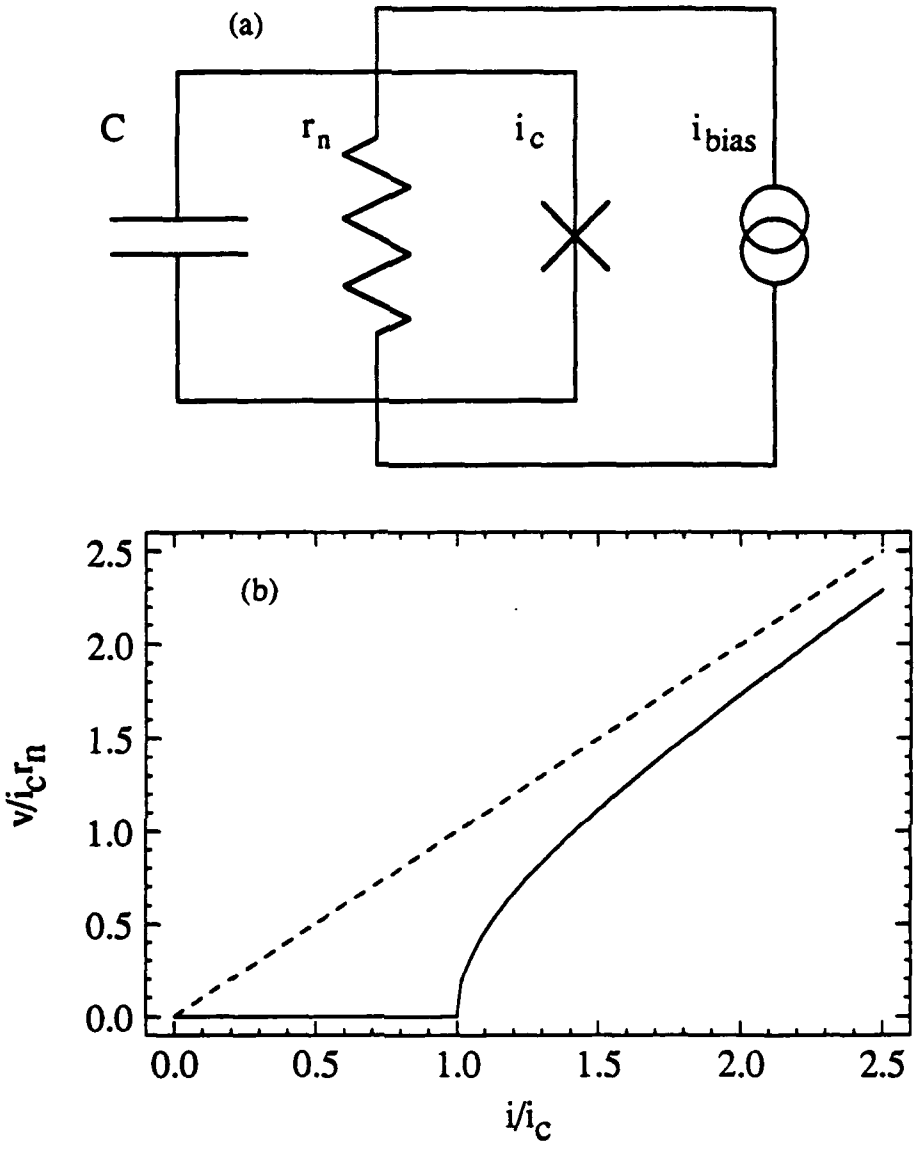

Fig. 1.1. (a) Schematic diagram of the resistively shunted junction model, where the Josephson junction is modelled as a resistance, r_n, and capacitance, C, in parallel with the supercurrent channel with critical current, i_c. i_{bias} is the bias current. (b) Normalized voltage vs. normalized current for a single overdamped junction (for C = 0) from the RSJ model (solid curve). The dashed curve represents the normal resistance, r_n, and illustrates how the junction i-v curve approaches R at higher currents.

where $\tau = 2\pi\nu_c t$ is the dimensionless time, and $\beta_c = r_n^2 C/L_J$ is the McCumber parameter, equivalent to the dimensionless capacitance. These dimensionless parameters are written in terms of the characteristic frequency, $\nu_c = 2ei_c r_n/h$, and the Josephson inductance $L_J = \hbar/2ei_c$. It is important to note that (1.2.2) is analogous to the equation for a damped driven pendulum. When $\beta_c < 1$, the junction is overdamped, *i.e.* there is no resonance frequency in the system and the voltage across the junction is a single-valued function of the bias current. Our SNS junctions have negligible capacitance, so that $\beta_c << 1$ and they will be well-described by the overdamped model. When $\beta_c = 0$, (1.2.2) is reduced to a first-order differential equation, and the corresponding dc voltage is found to be $v = i_c r_n \sqrt{(i_{bias}/i_c)^2 - 1}$. The current-voltage curve for this overdamped case is plotted in Fig. 1.1b, and is representative of our single junctions.

1.3 The Kosterlitz-Thouless Phase Transition

The 2D arrays that we have studied are made of superconducting islands weakly coupled together through a normal metal, *i.e.* SNS Josephson junctions. The coupling strength between each of the islands can be inferred from (1.1.1) (see Tinkham, 1975, p. 211). This coupling energy is $-E_J(T)\cos\gamma$, where $E_J(T) = \hbar i_c(T)/2e$ is the Josephson energy.

In zero magnetic field the arrays will undergo a Kosterlitz-Thouless phase transition (Kosterlitz and Thouless, 1973) to an ordered state, which is dominated by the effects of thermally-induced vortices. The phase transition temperature, T_c, is determined by the temperature above which a free vortex is energetically favorable. In arrays, as shown by Lobb *et al.* (1983) and Mooij (1983),

$$kT_c = (\pi/2)\, E_J^*(T_c)\,, \qquad (1.3.1)$$

where $E_J^*(T)$ is a renormalized coupling energy which includes the effects of fluctuations from spin waves and vortices.[1] Equation (1.3.1) is the junction array form of $\hbar^2 n_s^*(T_c)/2mkT_c = \pi/2$, which is the universal quantity that determines the transition temperature in 2D superfluids, where $n_s^*(T)$ is the superfluid density. Nelson and Kosterlitz (1977) predicted that the superfluid density in an infinite sample would undergo a discontinuous jump to zero when it intersects with this line, and that the slope of this line $(2/\pi)$ is a universal constant. In an isotropic system, $E_J^*(T)$ is identical to the helicity modulus, $Y(T) = E_J^*(T)$, which is a measure of the phase correlations in the system.[2] The helicity modulus for zero magnetic field, as determined from Monte Carlo simulations on finite arrays, is plotted in Fig. 1.2, and shows how the transition temperature of the system can be determined from the universal line of (1.3.1). Note that $kT_c \approx 0.95\ E_J(T_c)$ from these simulations. The helicity modulus for a number of commensurate magnetic fields (see Section 1.4) are also plotted in Fig. 1.2, and also have phase transition temperatures determined by the sharp jump in Y(T) signifying the onset of correlations.

In zero magnetic field, as mentioned above, the phase transition is dominated by thermally induced vortices. For $T < T_c$, all the vortices are bound in dipole pairs, each consisting of two oppositely-signed vortices, *i.e.* their currents flow in the opposite direction. Because these dipole pairs have zero net vorticity, the array will have zero resistance for temperatures below T_c. For $T > T_c$, thermal excitations cause some dipole pairs to unbind, thus giving rise to dissipation when a measuring current is present. A resistive transition results from the thermally-activated vortex unbinding, and the sheet

---

[1] In zero field, $E_J^*(T) = E_J(T)[1-kT/4E_J(T)]/\varepsilon(T,l)$, where the negative term inside the brackets results from spin waves and $\varepsilon(T,l)$ is a polarizability due to vortex-vortex interactions that is a function of both temperature and renormalized length scale $l = \ln(r/a)$ (see Mooij, 1983).

[2] Y(T) determines the increase in the free energy of the system in response to a twist in the phases across the array (see Forrester, 1988, p. 98).

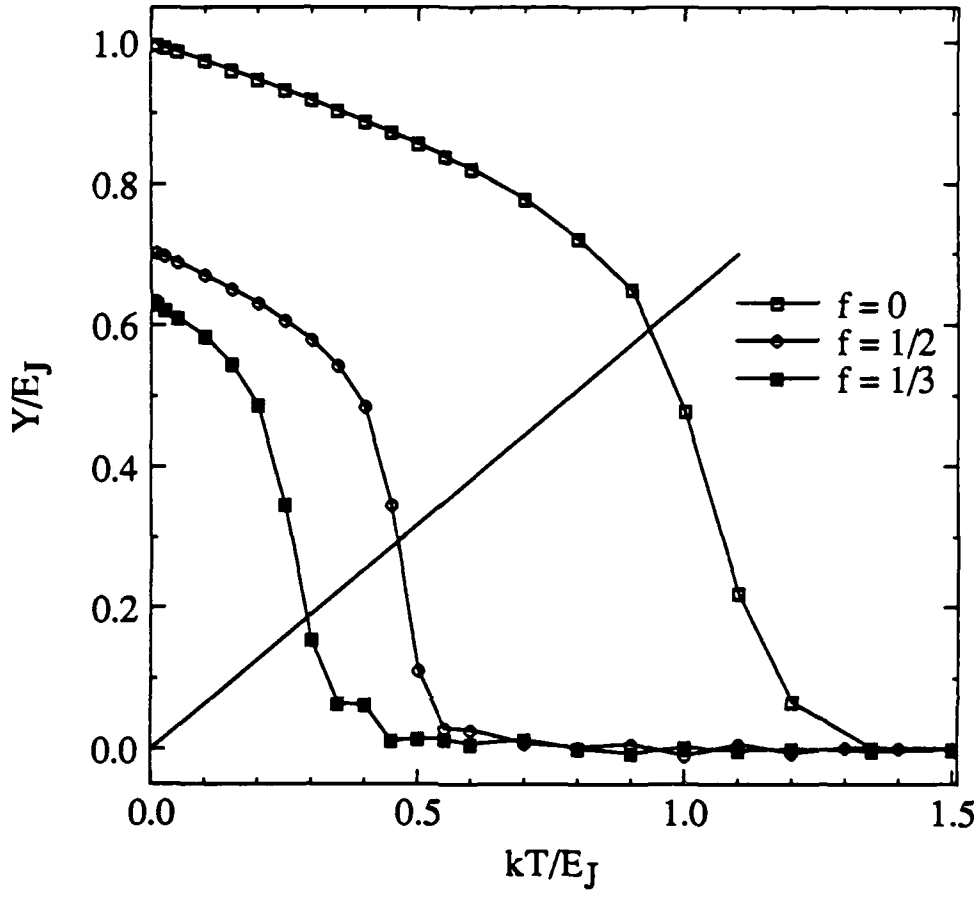

Fig. 1.2. Normalized helicity modulus *vs.* normalized temperature determined from Monte Carlo simulations for various commensurate magnetic fields (see Forrester, 1988, p. 98). The intersection of the helicity modulus with the universal line of slope $2/\pi$ determines the phase transition temperature for f = 0. The temperatures where Y(T) drops sharply for the other commensurate fields indicate their respective phase transition temperatures.

resistance, R(T), which is proportional to the density of free vortices, was shown by Lobb *et al.* (1983) to be

$$R(T) = \frac{r_n b_1 \exp\left[b_2 \left(\frac{kT}{E_J(T)} - \frac{kT_c}{E_J(T_c)} \right)^{-1/2} \right]}{I_0\left(\frac{E_J(T)}{10kT} \right)^2}, \qquad (1.3.2)$$

where I_0 is the modified (hyperbolic) Bessel function, r_n is the normal-state resistance of a junction (see Section 1.2), and b_1 and b_2 are constants.

The resistive transition of one of our arrays is shown in Fig. 1.3. When the temperature decreases from 10K to 8K, a sharp drop in resistance is observed at 8.8K when the Nb islands become superconducting. As the temperature is further lowered, the resistance decreases quickly and then gradually flattens out almost to a plateau at about 4K. This particular region is characterized by proximity effects, where the superconductivity is spreading from the superconducting islands into the normal metal region between the junctions (Abraham *et al.*, 1982). At approximately 4K, dipole pairs begin to form. As we approach $T_c \sim 3.5$K, the resistance drops sharply as described by (1.3.2), and below T_c all the vortices are paired. For temperatures[3] far below T_c, $kT/E_J(T) << kT_c/E_J(T_c)$, very few dipole pairs are thermally excited in the array.

The resistive transition of the arrays in zero field is much different from that of the single junctions from which it is made. As stated previously, the T_c of the array is determined by a 2D vortex-unbinding phase transition and its resistive transition is dominated by the exponential temperature dependence of the number of free vortices. The resistive transition of the single weakly-coupled junctions, however, is determined by the

[3]The normalized temperature $kT/E_J(T)$ must be used when comparing with theory which is derived for a temperature independent coupling energy (see Lobb *et al.*, 1983 and Abraham *et al.*, 1982).

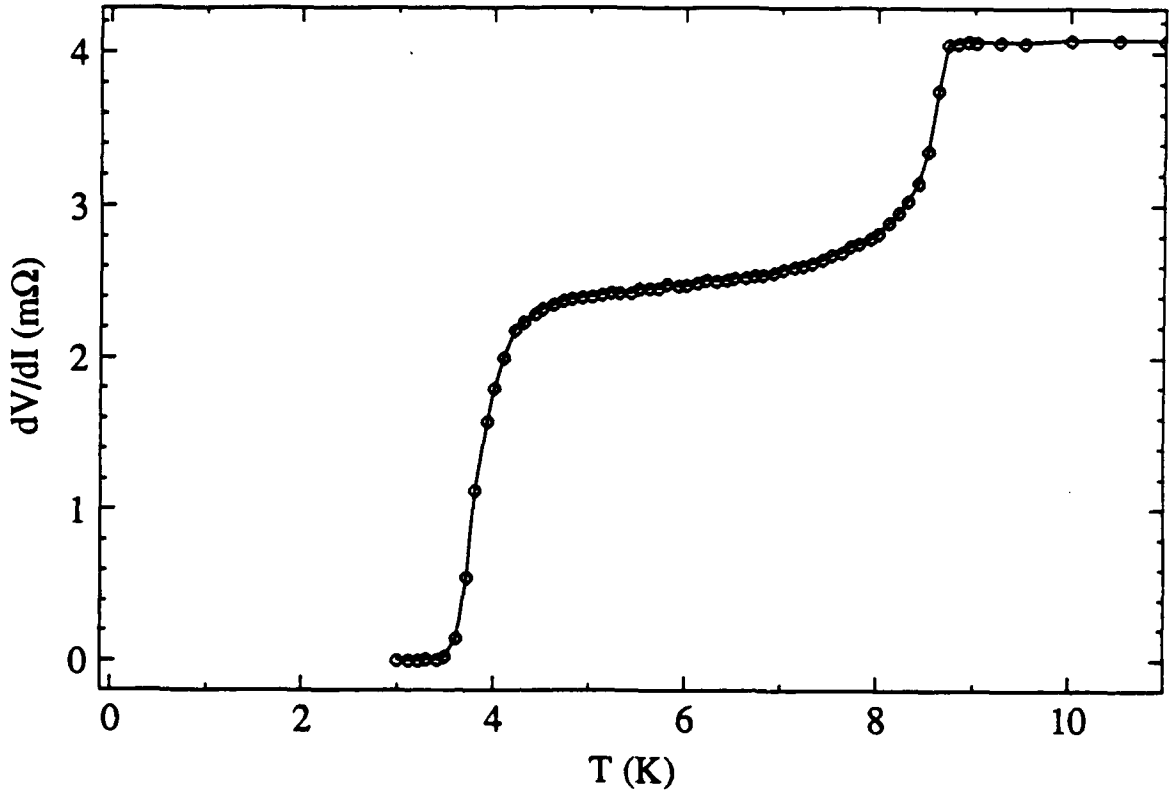

Fig. 1.3. Typical measured resistive transition of a 1000 by 1000 array, showing two transitions. The sharp drop in resistance at ~8.8K is the temperature where the Nb islands becoming superconducting. The drop to zero resistance from 4K to 3.5K is due to the Kosterlitz-Thouless 2D phase transition.

ratio of the Josephson energy to the energy due to thermal fluctuations. As was shown by Ambegaokar and Halperin (1969), the single junction resistance has the form,

$$r(T) = \frac{r_n}{I_0\left(\frac{E_J(T)}{kT}\right)^2}. \qquad (1.3.3)$$

Because of thermal fluctuations, a single junction never truly has zero resistance like that of an infinite 2D array for $T < T_c$. Monte Carlo simulations (see Fig. 1.2 and Teitel and Jayaprakash, 1983a and 1983b) on arrays have determined $kT_c/E_J(T_c) \approx 0.95$ in zero field. At this particular temperature, the single junction has not yet dropped to even one-half of its normal state resistance, according to (1.3.3). Thus, the T_c of the array is much higher than the temperature at which the single junctions approach zero resistance. Critical currents typically become measurable in the single junctions only below $T \sim 1.5K$. We are thus unable to measure the dynamical properties of the single junctions at 1.5K-3.5K, temperatures at which we typically measure the arrays (see Chapter 2).

1.4 Commensurate Magnetic Fields

When a perpendicular magnetic field, H, is applied to a 2D array, currents appear in the form of vortices which are constrained by both the geometry of the 2D network and flux quantization to flow through certain junctions. When the magnetic field applied to a periodic array is such that the average number of flux quanta per unit cell, f, is the ratio of two integers p and q, $f = Ha^2/\Phi_0 = p/q$, where a is the array lattice constant and $\Phi_0 = h/2e$ is the flux quantum, the field is said to be 'commensurate' because the field-induced vortices are arranged in spatially periodic superlattices commensurate with the junction array

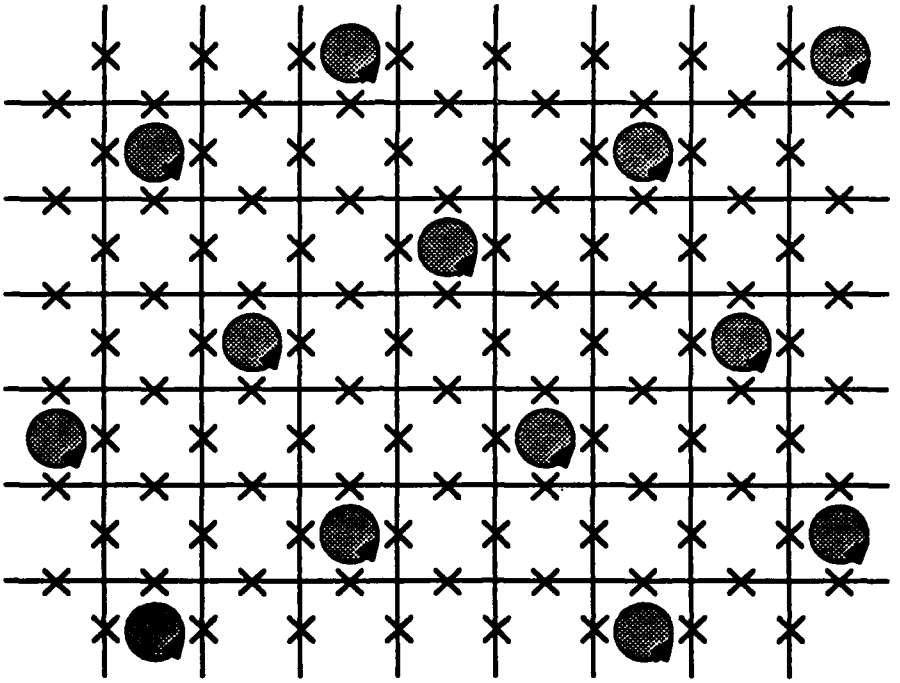

Fig. 1.4. Schematic diagram of a square array of Josephson junctions in a commensurate magnetic field, where the average number of flux quanta per unit cell of the array, f, is one-fifth (f = 1/5). The 'x's mark the positions of the junctions and the direction of the applied field is out of the page. There is one vortex centered on every fifth unit cell as indicated by the filled circles with arrows. The vortices are arranged in a *superlattice* which is commensurate with the underlying array.

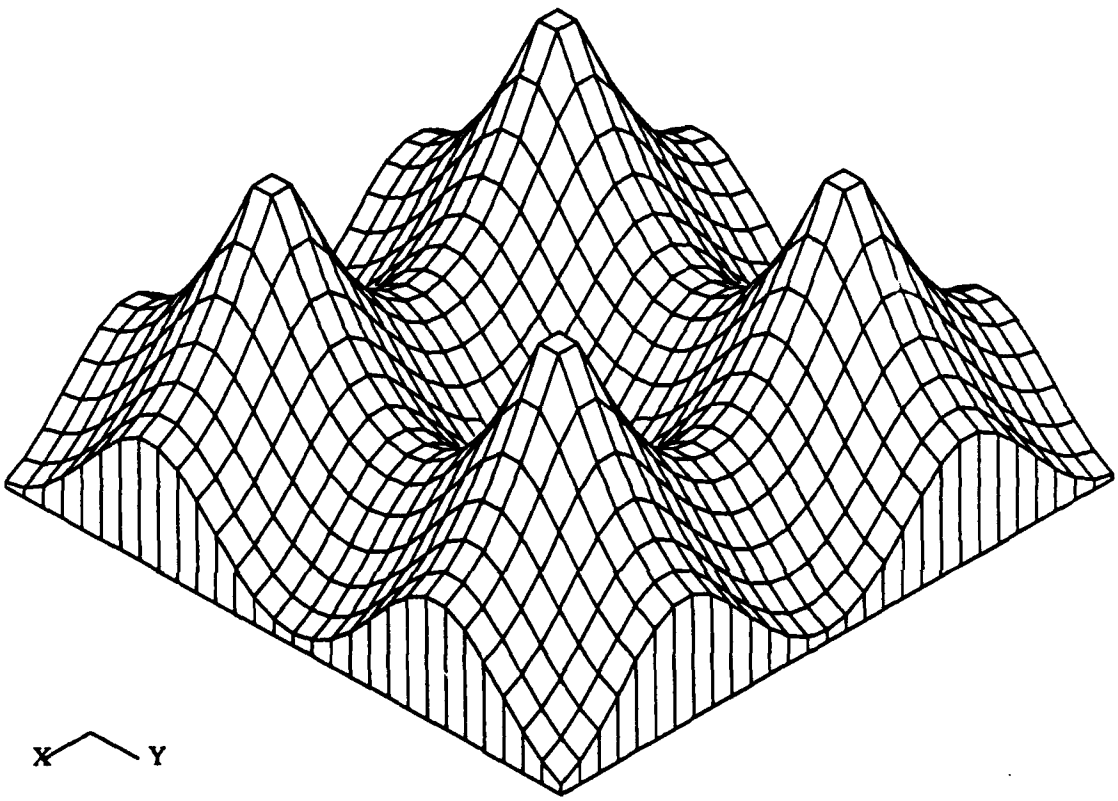

Fig. 1.5. Calculated 2D periodic vortex potential energy as a function of vortex position for a representative area near a single unit cell in a square array (Rzchowski *et al.*, 1990). The peaks correspond to the vertices where the junctions meet. The minimum in the center corresponds to the vortex position being centered on the unit cell. The four higher energy saddle points correspond to the vortex being centered on each of the four junctions, which is an unstable position. The energy barrier from the minimum in the center to the saddle points on the junctions is $0.2E_J = 0.2\hbar i_c/2e$ (Lobb *et al.*, 1983). This potential is identical for all unit cells, making up the entire 2D 'egg-carton' potential seen by a single vortex in the array.

geometry. This is shown schematically in Fig. 1.4 for the specific case where f = 1/5 on a square array.

The vortices arrange in these special superlattices as a result of their mutually repulsive interactions and each individual vortex's interaction with the underlying lattice. An individual vortex sees the array of junctions as a periodic two-dimensional energy potential. The vortex has a minimum energy when centered on an array unit cell and a higher energy when centered on one of the junctions. Thus an energy barrier exists between adjacent unit cells. This energy barrier was calculated by Lobb *et al.* (1983) to be $E_B = 0.2E_J$. Using the same method, Rzchowski *et al.* (1990) calculated the 2D vortex potential energy as a function of vortex position throughout the array. The resulting 2D 'egg-carton' potential for a single unit cell in the array is shown in Fig. 1.5. The minima in this potential act as pinning centers for the vortices.

The vortex superlattices for the commensurate magnetic fields, where f = p/q, were shown by Teitel and Jayaprakash (1983b) to have qxq unit cells. The vortex superlattice unit cells for f = 1/2 and f = 1/3 are shown in Fig. 1.6. The commensurate fields (in a regular array) are periodic for integer f because for an integer number of flux quanta per unit cell there are no field-induced currents and the array behaves as in zero field. There is also a symmetry about f = 1/2, because for this field the vortices are the most closely packed (see Fig. 1.6a), one in every other unit cell; the superlattices for fields above f = 1/2 have the same superlattice unit cells as their symmetric fields below f = 1/2 except that all current directions are reversed. For example, the f = 2/3 superlattice has the same superlattice unit cell as that for f = 1/3 shown in Fig. 1.6b except that the currents flow in the opposite direction. Thus for $1/2 < f < 1$, vortices of current with opposite sign from those for $0 < f < 1/2$ will determine the properties of the array.

Some of the properties of arrays in commensurate magnetic fields have been studied a great deal. The transition temperature, $T_c(f)$, and the critical current, $I_c(f)$, for a square array have been shown theoretically (Teitel and Jayaprakash, 1983; Shih and Stroud, 1983

(a) f = 1/2

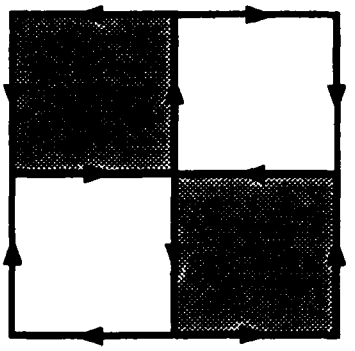

(b) f = 1/3

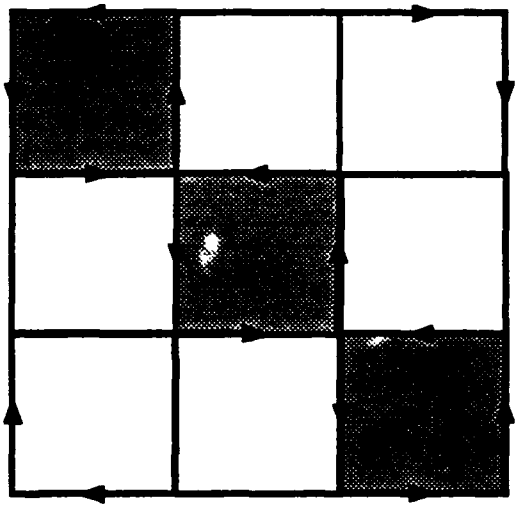

Fig. 1.6. Unit cells for vortex superlattice ground state (T = 0) configurations with zero bias current. Arrows indicate the direction of current flow. The shaded unit cells are regions of positive vorticity. a) f = 1/2, q = 2, with currents equal to $i_c \sin(\pi/4)$; b) f = 1/3, q = 3, with currents equal to $i_c \sin(\pi/3)$.

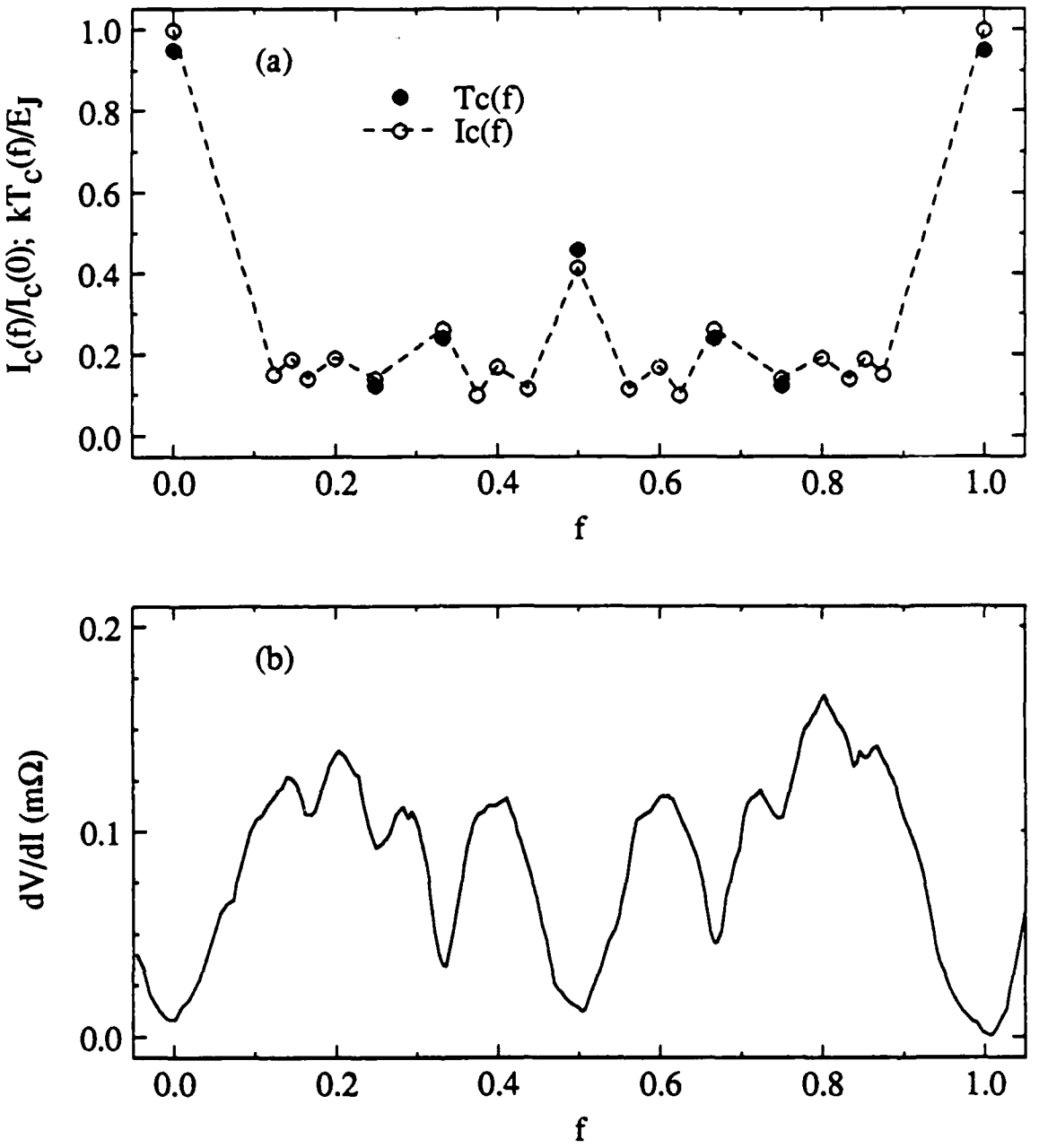

Fig. 1.7. (a) Theoretical calculations (Teitel and Jayaprakash, 1983b) of phase transition temperature $T_c(f)$ and zero-temperature critical current $I_c(f)$ for different commensurate magnetic fields. (b) Experimental measurement of magnetoresistance (see Chapter 3) showing minima near the strongly commensurate fields. Both graphs show the periodicity for integer f and the symmetry about f = 1/2 of these measurable properties of a 2D array in a magnetic field.

and 1985) to be periodic for integer changes in f and symmetric about f = 1/2. These results are plotted in Fig. 1.7a. Experimental measurements of the magnetoresistance (see Section 3.3.2), R(f), also show this particular symmetry, an example of which is plotted in Fig. 1.7b. $T_c(f)$ and $I_c(f)$ have their largest values and R(f) has the sharpest minima for these commensurate fields where the vortex superlattice is the most strongly coupled to the underlying array. This occurs when f is the ratio of *small* integers, namely when f = 0, 1/4, 1/3, 1/2, 2/3, 3/4, and 1, for a square array. We will define these particular fields as 'strongly commensurate' fields. In Chapter 4 we will show that the rf effects in the presence of commensuration have the same symmetry with the magnetic field.

CHAPTER 2

EXPERIMENTAL TECHNIQUES

2.1 Fabrication Methods

The fabrication of 2D SNS arrays in this group has developed considerably over the years. David Abraham (1983) made the first arrays by evaporating lead (Pb) through a fine metal mesh, forming large square-shaped islands on top of a thin copper (Cu) film. In order to reduce the size of the junctions and improve the controllability of the fabrication process, Martin Forrester (1988) developed photolithography techniques for patterning the arrays. These arrays were cross-shaped Pb islands on a copper film, where the islands were created by patterning photoresist islands on a Pb-Cu bilayer and then removing the unwanted Pb by ion beam-etching.

We have further improved on the array fabrication process by using a more robust superconductor, niobium (Nb). The advantages of arrays made of Nb versus Pb are threefold: Nb is a refractory superconductor that is very hard, it has a higher superconducting transition temperature, T_{cs}, and the fabrication techniques that can be used allow greater flexibility, uniformity and control of the junction characteristics. The refractory nature of the Nb allows the arrays to be repeatedly cycled between 4.2K and room temperature with no change in physical characteristics, and without the need for an insulating passivation cap, which was required for the Pb-Cu arrays. The higher $T_{cs} \approx 9K$ for Nb makes the interesting temperature range for studying the arrays more convenient, because the Kosterlitz-Thouless transition temperature can be increased to a more accessible temperature near 4K.

Other advantages for the Nb-Cu arrays are a result of improved fabrication processes. Nb can be reactive-ion-etched (RIE), which is a much lower energy process than ion beam-etching, thereby causing less damage to the junction region. Furthermore, ion beam-etching can not ensure junction uniformity over large (1cm x 1cm) array areas as a result of the narrow beam size, and the reproducibility of the junctions is limited by visual monitoring of the etch process (because the beam is shut off manually when the copper film appears). The junction uniformity in the Nb-Cu arrays is limited solely by the uniformity of the photolithography processing since the reactive-ion-etching automatically stops when it reaches the copper.

One of the disadvantages of our Nb-Cu array process is that the bilayer is not made *in situ*, thus requiring an rf argon ion-etch step to remove the copper oxide that forms in transit. This additional step, however, does not noticeably degrade the junction quality or uniformity.

The change from Pb to Nb required the development of a number of new fabrication technologies, including magnetron sputtering, rf cleaning and etching, reactive-ion-etching, and inverting photoresist. We will briefly describe the fabrication process below and then discuss in detail the design of the magnetron sputtering machine and the rf etching process. A detailed description of the Nb-Cu array fabrication procedure is contained in Appendix I, and an outline of the steps is shown in Fig. 2.1.

Our two-dimensional arrays consist of 1000 by 1000 Nb-Cu-Nb proximity-effect junctions. Sample fabrication is begun by thoroughly cleaning a 1" square and 0.025" thick sapphire substrate which has been polished on both sides. The substrate is then prepared with a photoresist 'trilayer,' consisting of an exposed layer of photoresist, a thin layer of Al, and an unexposed layer of photoresist on top. This trilayer technique is a simple method for creating a thick undercut that will allow the thick Nb-Cu bilayer to lift off easily after deposition. We expose the top photoresist layer using various masks to define the dimensions of the array and the measuring leads. (A number of measurement

1) Photoresist pattern array dimensions, rf clean substrate, evaporate Cu

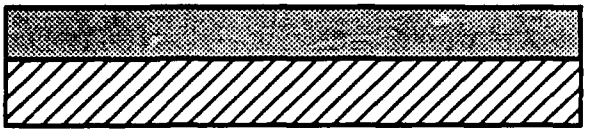

2) Move to sputtering machine, rf Ar ion etch Cu, sputter Nb

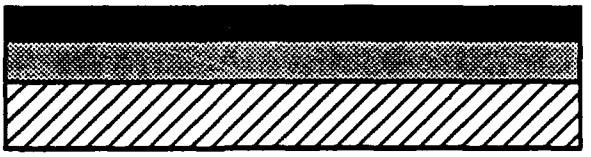

3) Lift-off Nb-Cu bilayer, pattern islands with inverting photoresist

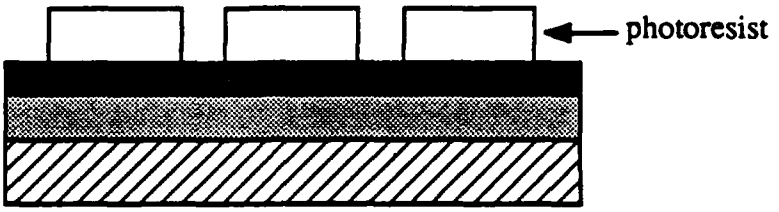

4) Remove Nb between islands with SF_6 reactive ion etch

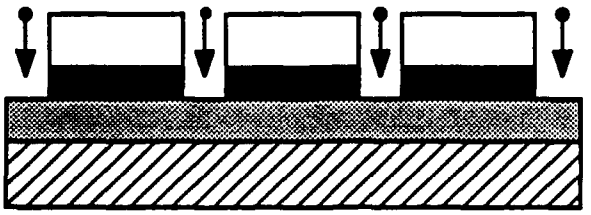

5) Remove photoresist with stripper

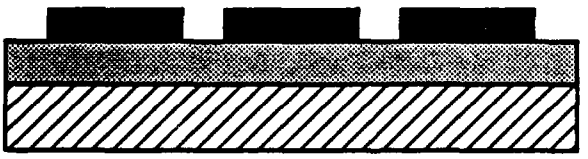

Fig. 2.1. Outline of Nb-Cu array fabrication process.

lead configurations were used, including the superconducting and normal metal contacts shown in Fig. 2.6, requiring slightly modified fabrication steps. These bilayer masks were all made lithographically in our lab.) The photoresist is exposed with 400nm wavelength ultra-violet light on a Karl Suss (model MJB3) contact mask aligner, which can easily expose 1μm minimum features. We then develop the photoresist and complete the trilayer processing to create a 1-3μm undercut around the edges.

The sapphire substrate is then mounted in the evaporator, where it is cleaned with an rf argon (Ar) plasma prior to thermally evaporating the 0.35μm thin-film of high purity copper (99.999%). The rf cleaning step improves the adhesion of the copper to the substrate by removing H_2O molecules bonded on the surface. The substrate is then moved to the magnetron sputtering machine (see Fig. 2.4) and mounted on a 60°F water-cooled substrate holder. The sample is rf Ar ion-etched (see Fig. 2.5) to remove any oxide that may have formed on the surface of the copper. About 50nm of copper is removed and then 0.2μm of niobium is sputtered immediately (within 1 sec) to ensure that a clean interface is formed. The photoresist is then lifted off with acetone, leaving behind on the substrate, a Nb-Cu bilayer in the pattern of the array and measurement leads.

Cross-shaped niobium islands are then formed by patterning photoresist islands with inverting photoresist on the bilayer and then reactive ion etching with SF_6 to remove the unwanted niobium between the islands. An inverting photoresist (AZ-5214E from Hoechst, Inc.) was necessary because the commercially-made mask for the islands of the large 1000x1000 array (by Advance Reproductions, Andover, Mass.) was of the opposite sign (no chrome inside the crosses). To complete the array fabrication process, the photoresist is removed with stripper and rinsed with H_2O, leaving behind an array of Nb islands on top of a copper film with measuring leads.

A 3D schematic of a two-island region of the completed array is shown in Fig. 2.2, and a photograph of a small region of a 1000x1000 Nb-Cu array is shown in Fig. 2.3. The islands have a lattice constant, a, of 10μm and the proximity effect weak links,

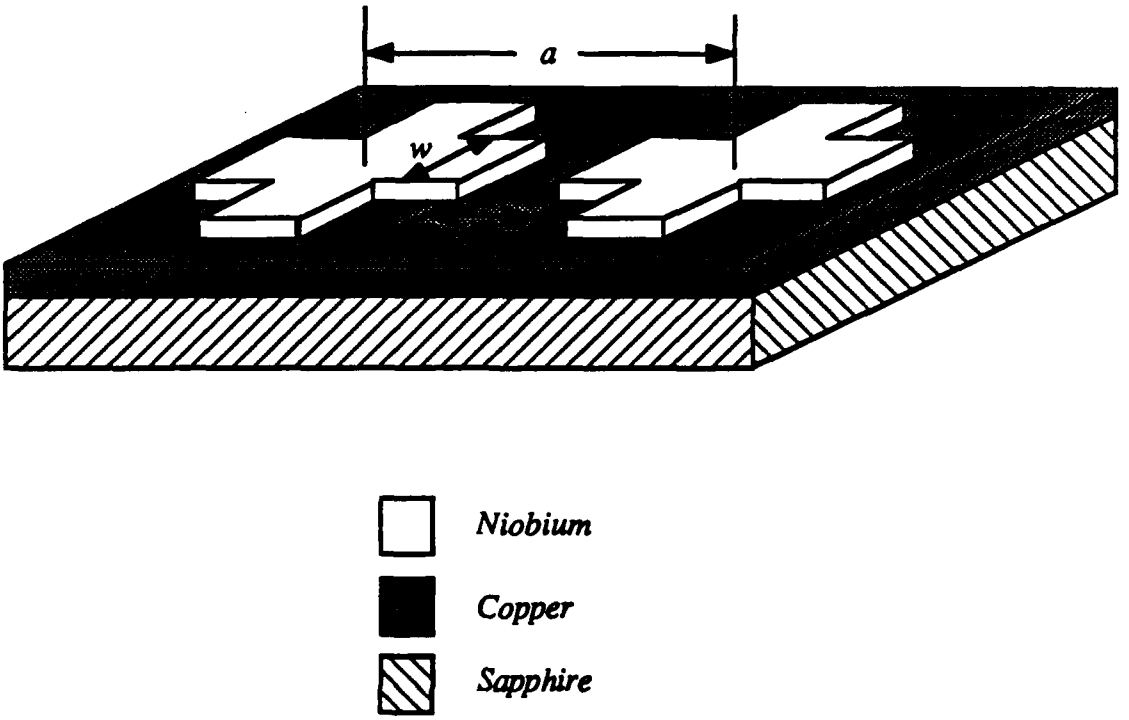

Fig. 2.2. 3D schematic showing a region of the completed array near two of the Nb islands. The relevant sample and junction dimensions are shown. The junction region lies between the tips of the crosses, having length $d = 2\mu m$ and width $w = 4\mu m$. The distance between the centers of the Nb crosses determines the lattice constant of the array $a = 10\mu m$. The thin-film thicknesses are $0.2\mu m$ of niobium and $0.3\mu m$ of copper. The sapphire substrate was generally 0.025" thick.

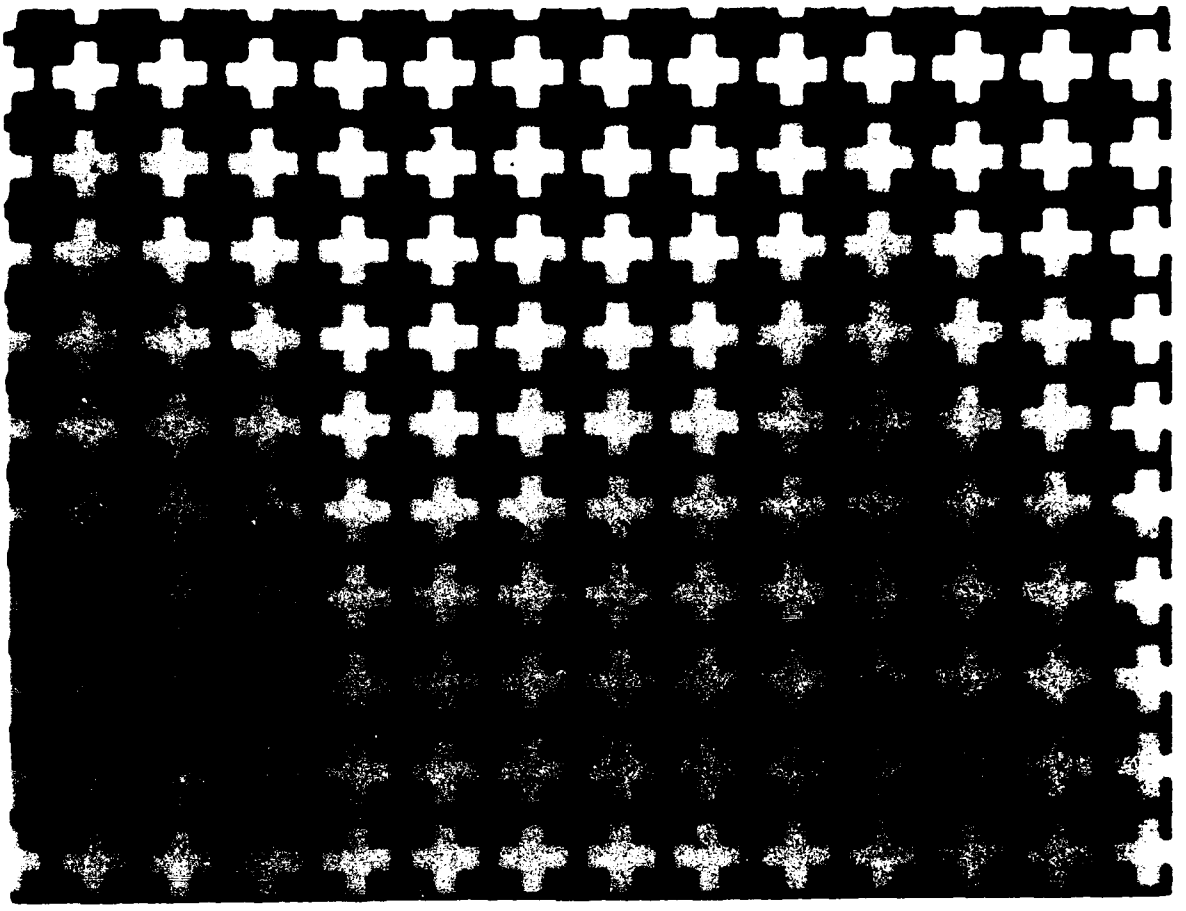

Fig. 2.3. Photograph of a small region of a 1000 by 1000 Nb-Cu array. The crosses are the niobium islands lying on top of the copper underlayer. The periodic lattice spacing between the centers of the islands is $a \approx 10\mu m$. The niobium is 0.2μm thick and the copper is 0.3μm thick.

consisting of the underlying copper between the islands, are defined by the width (4μm) of the arms of the cross and the separation (2μm) between their tips. Two single junctions with the same geometry as the junctions in the array are concurrently made adjacent to the array on the same substrate, and are used for characterizing the single junctions as will be discussed in the following chapters. There are actually 1400x1000 Nb islands in the array (as shown in Fig. 2.6), but we place the voltage leads 1000 junctions apart in order to measure a square 1000x1000 junction array. Because the array is square, it will have the same normal state resistance as the single junctions (typically R_n~2mΩ), determined primarily by the copper.

The magnetron sputtering system was originally dedicated to Nb, although an Al magnetron was added later for making Nb-Al_2O_3-Nb junctions for dc SQUIDs (see Appendix II). Magnetrons are generally the best for making high purity Nb films because the magnets inside the water-cooled target holder enable a higher density plasma to be generated, so that higher sputtering rates can be achieved with lower Ar pressures. The pumping system consists of a 6" diffusion pump, backed by a 35 cfm Welch rotary pump. A large (10 liter, 18 hour holding time) liquid N_2 cold trap with an anti-migration baffle (Cooke Vacuum Products, Inc.) above the diffusion pump is essential for obtaining low base pressures and for keeping most of the pump oil out of the chamber. With this pumping system, the chamber can be pumped down to pressures as low as $2x10^{-8}$T. The gases are controlled (typically 35 sccm) by flow meters and controllers (MKS Instruments, Inc.), and the Ar pressure (6mT) during sputtering is monitored by a capacitance manometer (MKS Instruments, Inc.). The dc power supply for the magnetrons can provide up to 1000V, but is typically operated at 500V, giving a 150mA current for Nb sputtering at the flow rate and pressure mentioned above. The sputtering rate for Nb at the above parameters was ~20nm/min for our small 1-1/2" diameter magnetrons. The chamber design is shown and described in detail in Fig. 2.4. The Ferrofluidic rotary feedthrough

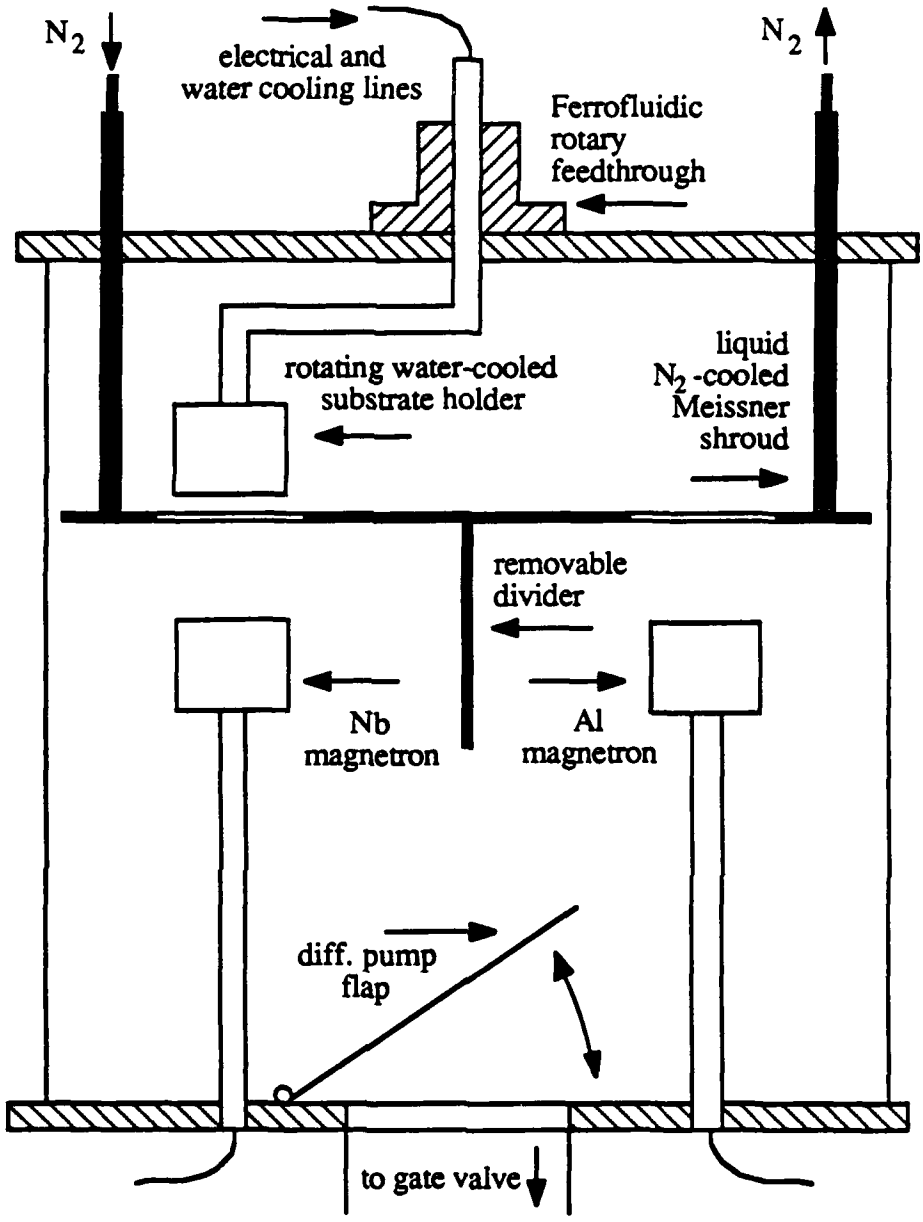

Fig. 2.4. Magnetron sputtering chamber design. The substrate is mounted on a water-cooled holder that can be rotated above two dedicated magnetron targets (Nb and Al). A circular, liquid N_2-cooled Meissner shroud is placed between the targets and the substrate holder to help getter impurities during pre-sputtering and to act as a shield (or fixed shutter) by rotating the substrate holder away from the holes directly above the magnetrons. The diffusion pump flap is used to increase the chamber pressure quickly when igniting a plasma. An rf plasma can be applied to the substrate (see Fig. 2.5) for rf cleaning or ion etching.

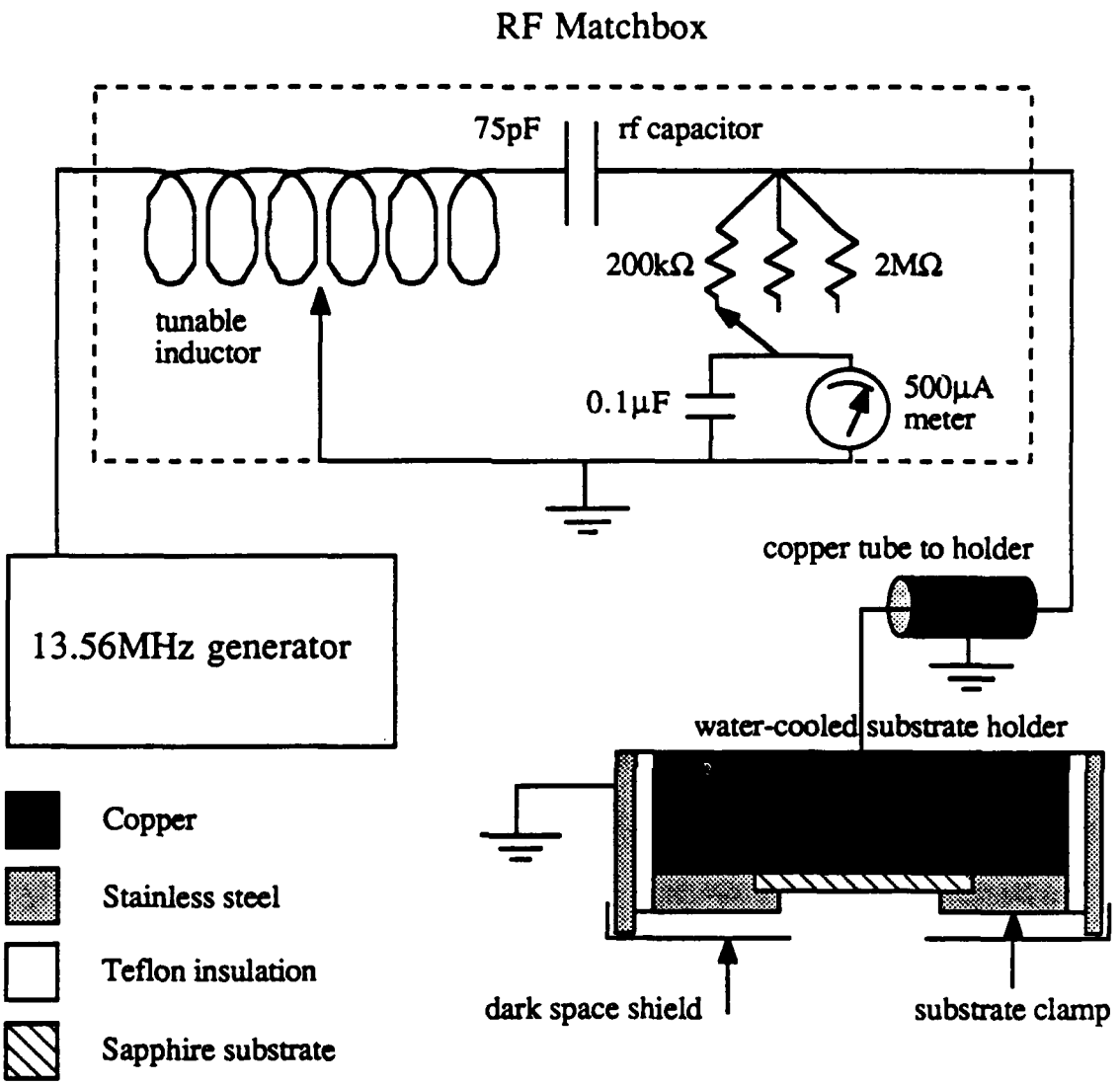

Fig. 2.5. RF argon cleaning and ion-etching circuit for sputtering machine, showing details of the rf matchbox and substrate holder. The dc self-bias voltage of the plasma is measured through the matchbox meter; by selecting the appropriate resistor, 200KΩ, 1MΩ, or 2MΩ, the full scale voltage can be selected to be 100V, 500V or 1kV. The inductor is used to tune the resonance of the circuit in order to match the impedance of the plasma. When the matchbox is used to rf clean in the evaporator or to reactive ion etch, the rf capacitor must also be changed (to 25pF) to help tune the circuit to the very different rf plasma impedance. The height of the grounded dark space shield above the sample is important in determining the plasma characteristics and should be kept at ~1/8-1/4".

was a very important addition to the system, because the previous o-ring rotary feedthrough did not hold a tight vacuum when it was turned.

The other crucial addition to the system was the achievement of good rf coupling at high powers through the long 1"copper tube and down to the substrate holder, which was necessary for the rf Ar ion-etching. A detailed drawing of the rf circuit and substrate holder is shown in Fig. 2.5. An rf 'matchbox' with a variable inductor is used to match the rf impedance of the 13.56MHz (Advanced Energy, Inc., model RFX-600) rf generator to the rf plasma. The matchbox has a meter that monitors the dc self-bias voltage, V_{dc}, across the plasma, which is an important plasma characteristic. For rf cleaning V_{dc} is typically 250V, while for rf etching 600V is generally required.

2.2 Measurement Techniques

The substrates are mounted in a measurement rig (described below), which is placed in a temperature-controlled, μ-metal shielded, ^{4}He cryostat inside a screened room. The μ-metal shielding screens out external magnetic fields to better than ~ 0.1mGauss, as estimated from the array measurements. The screened room is not generally necessary. The sample rig, which has undergone many modifications since it was originally built, is described in detail in Abraham (1983) and Forrester (1988). This rig is essentially a four-point measurement probe with a temperature-controlled substrate block inside a vacuum can. The rig has been modified to reduce the number of solder joints near the sample block, in order to minimize field non-uniformity caused by superconducting solder. The substrate is mounted on the copper block and then a Pb-free "Naval Brass" can is slid over it and sealed with an indium o-ring. This can is evacuated and then back-filled with a very small amount of He exchange gas, so that the sample block can be heated above the temperature of the liquid-He bath. A 10cm long, 5.5cm diameter copper solenoid is mounted outside of this can, and centered around the sample, so that a uniform

perpendicular magnetic field can be applied to the array (~13mA/Gauss). One Φ_0 per unit cell in the array (f = 1) required H ≈ 200mGauss. Using a regulatable pumping system, the pressure in the cryostat can be reduced so that the temperature of the He bath can be controlled down to a minimum of ~ 1.35K. The temperature of the substrate and sample block is controlled with a Lake Shore Cryotronics Temperature Controller (model DRC-91C) through a heating resistor and a calibrated germanium thermometry resistor (Cryocal #4033, 1087Ω @ 4.25K), both of which are mounted on the sample block. The temperature of the substrate in the vacuum can easily be controlled from 1.35K to 10K with a stability of better than 1mK.

The electrical wiring of the low temperature rig uses twisted pairs of 36 and 40 gauge copper wire for the current and voltage leads, respectively. The wires are wound with many turns onto two separate copper block stages at the bottom of the rig to improve the heat sinking of the leads and reduce the effects of thermal emf's on the sample. The wires are connected to the measurement contacts on the substrate using pressed indium-dot contacts. The two different 'four-point' measurement circuits that were used are shown in Fig. 2.6. These circuits enabled a number of different measurements to be taken, including current vs. voltage (I-V), dynamic resistance (dV/dI) vs. current (or voltage), and dynamic resistance vs. perpendicular magnetic field curves. Fig. 2.6a shows how separate pairs of superconducting bus bars were used to current-bias the array and to measure its voltage, with either a lock-in amplifier or a nano-voltmeter. Fig. 2.6b shows the normal metal contact configuration that had better performance at low temperatures, as will be discussed in Section 2.3.

We used a PAR 124A lock-in amplifier at 45.5Hz, with a PAR model 116 1:100 transformer at the input to improve the impedance match from the low-resistance array. The rms amplitude of the ac current through the sample was always chosen at least 100 times smaller than the measured critical current of the array (see Chapter 3). Under these conditions, measurements with a sensitivity better than 1nV could be obtained with lock-in

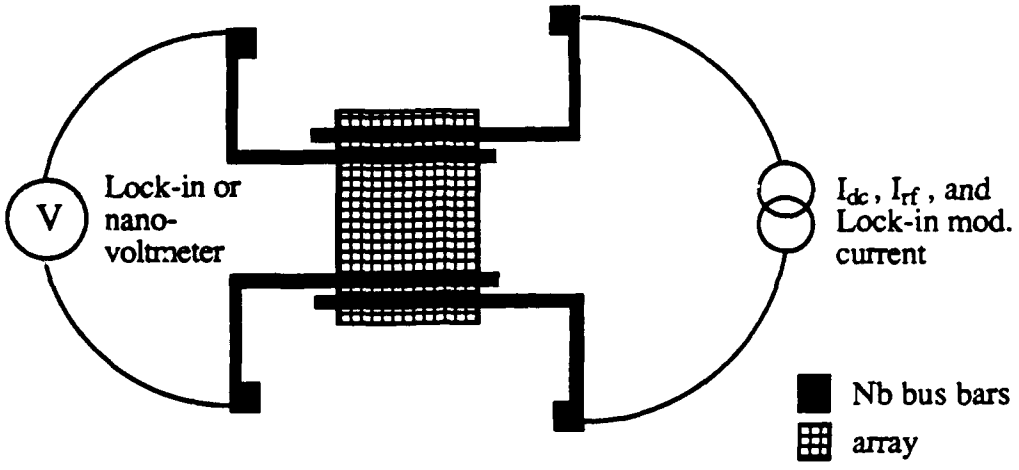

Fig. 2.6. (a) Measurement circuit for sample with superconducting busbars

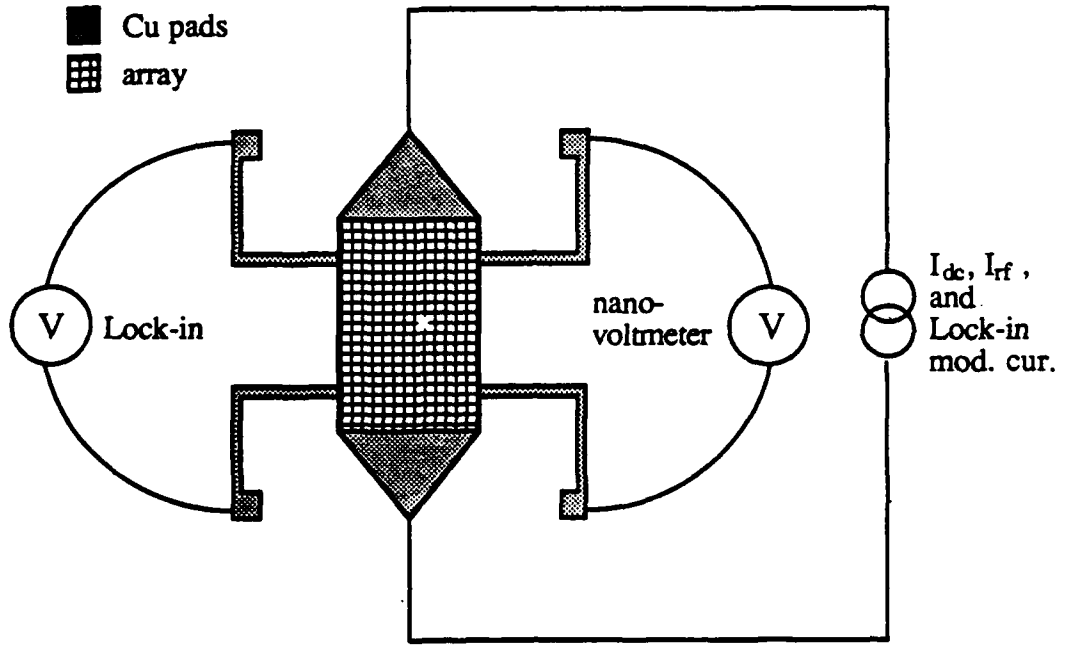

Fig. 2.6. (b) Measurement circuit for sample with normal metal contacts

time constants less than 1sec. A home-made battery-powered supply was the dc current source of choice (for its lower noise characteristics), although an HP 6181B dc current supply had to be used when larger currents (>100mA) were required. The rf signal generator was an HP 8656B signal generator with a frequency range of 0.1-990MHz. The nano-voltmeter was a Keithley Instruments model 148. Its available sensitivity was not fully used for the arrays, typically being operated only in the 0.1-1.0μV scales, because the array voltage was N = 1000 times larger than the single junction voltage, V = Nv. The nano-voltmeter was very useful, though, when measuring the single junctions. Ground loops caused some difficulties in the measurement circuit, but were broken by using a 1:1 transformer on the lock-in modulation signal output and 0.1μF blocking capacitors on the rf signal generator output. The data were initially plotted on an HP 7045B analog XY recorder and then digitized for computer analysis.

2.3 Experimental Details

A number of important sample-dependent characteristics greatly influence, and sometimes limit, the measurability of the arrays. The most influential characteristic, after the Kosterlitz-Thouless transition temperature, is the temperature dependence of the single junction critical current, $i_c(T)$. The junctions that make up our arrays arrays are SNS junctions which are weakly coupled for the temperature range of interest. Their critical current is, therefore, an exponential function of temperature (De Gennes, 1964):

$$i_c(T) = i_c(0)\left(1 - \frac{T}{T_{cs}}\right)^2 \exp\left(\frac{-d}{\xi_N(T)}\right), \qquad (2.3.1)$$

where T_{cs} is the transition temperature of the superconductor, ξ_N is the coherence length of the normal metal barrier and d is the effective separation between the islands (see Fig. 2.2). Our junctions follow this temperature dependence very well for the dirty limit form of ξ_N

(see Deutscher and De Gennes, 1969). This experimental temperature dependence for $i_c(T)$ is very important because it determines the temperature dependence of the junction's characteristic frequency as discussed in Section 1.2, and also the coupling energy that was discussed in Section 1.3.

It is desirable to make measurements at temperatures well below T_c to avoid the effects of thermally excited vortices that are predominant near the Kosterlitz-Thouless transition temperature. Experimentally, the temperature dependence of $i_c(T)$ will limit our ability to effectively measure large arrays at low temperatures, where $i_c(T)$ becomes exponentially large. The bias current required for arrays is proportional to the number of junctions across the width, M, of the array, $I_{dc} = Mi_{bias}$, where i_{bias} is the bias current per junction (Section 1.2). From (1.3.1) we can estimate $I_c(T_c)$ by assuming $E_J^*(T_c) \approx E_J(T_c)$ so that $I_c(T_c)/MT_c \approx 26.7$nA/K. Thus the critical current of arrays is typically $I_c \approx 0.1$mA near T_c (for M = 1000 and $T_c \approx 3.5$K), and becomes as large as 10-100mA for 1-2K lower temperatures according to (2.3.1).

The necessary higher currents at low temperatures limited the usable temperature range for the circuit in Fig. 2.6a. At low temperatures ($T < 2$K), this circuit with superconducting bus bar measurement leads, exhibited a current-dependent magnetic field offset at high-currents ($I > 5$mA). For example, at $T = 1.62$K and $I_{dc} = 9.2$mA ($I_c = 28$mA), an offset field of $0.026\Phi_0$ per unit cell or ~ 6mGauss was observed in magnetoresistance measurements (see Chapter 3). This offset field limited the maximum allowable bias current for this asymmetric current configuration, so that it could only be used at higher temperatures (typically $T > 2$K) where larger currents were not necessary. To avoid this current-induced offset field, which resulted from the asymmetric current-injection leads, we modified the circuit to use large triangular pads at the ends of the array, as shown in Fig. 2.6b. Normal metal pads and leads were chosen, instead of superconducting Nb, to avoid field-screening effects from large superconducting areas, thus improving the uniformity of the applied magnetic field in the array.

Two related sample-dependent properties also limited the temperature range of our measurements: the geometrical inductance of an array unit cell, L, and the kinetic inductance per square of the array, L_K. The kinetic inductance is related to the renormalized coupling energy, $E_J^*(T)$, discussed in Chapter 1, through the following equation

$$L_K(T) = \frac{\hbar}{2ei_c^*(T)}, \qquad (2.3.2)$$

where $i_c^*(T) = 2eE_J^*(T)/\hbar$ is the renormalized critical current per junction. At low temperatures, $i_c^*(T) \approx i_c(T)$ so that the kinetic inductance per square of the array is approximately equal to the Josephson inductance, $L_K(T) \approx L_J(T)$. The geometrical inductance, L, begins to play a role in the response of arrays when $L \geq L_J(T)$, which occurs at low temperatures when $L_J(T)$ becomes small, due to the exponential temperature dependence of $i_c(T)$ in (2.3.1). This change is analogous to the behavior of dc SQUIDs where $\beta_L = L/\pi L_J(T) = 2i_c(T)L/\Phi_0 = 1$ gives a 50% modulation in the maximum critical current between the f = 0 and f = 1/2 fields (see Tinkham, 1975, pp. 215-216). We also see a 50% change in the critical current modulation of one of the arrays for f = 0 and f = 1/2 (see Section 3.4) at a temperature T = 1.65K (for an array with T_c = 3.5K), where i_c = 100μA. If we use the analogy with the dc SQUID, we can estimate the geometrical inductance of the array unit cells to be L ≈ 10pH. We can also estimate L using a numerical determination for the inductance of a flat, thin-film superconducting washer by Chang (see Chang, 1981 and Jaycox and Ketchen, 1981) who found that $L \approx 1.25\mu_0 a$, where a is the diameter of the square washer hole. This gives L ≈ 10pH for a = 10μm, which is in very good agreement with our experimental estimate. Thus, our experimental measurements will be limited to temperatures above 2K, so that we are not dominated by geometrical inductance effects. All the data presented in the following chapters were taken at

temperatures well below T_c in order minimize the effects of thermally-induced vortex pairs, but not so low as to be influenced by the geometrical inductance of the array.

Another sample characteristic that could influence our measurements is the magnetic field-screening length, $\lambda_\perp$. This quantity is also related to the renormalized energy, $E_J^*(T)$, through the proportionality with the kinetic inductance per square, $\lambda_\perp(T) = L_K(T)/\mu_0$. Using the relation in (1.3.1), Lobb *et al.* (1982) showed that $\lambda_\perp(T_c) = (9.82 \text{ mm K})/T_c$, which will always be smaller than our 1cm array size (for N, M = 1000 junctions). For example, when $T_c = 3.5$K we have $\lambda_\perp \approx 2.8$mm. At lower temperatures, the temperature dependence of $i_c(T)$ will further decrease $\lambda_\perp(T)$. This is not a problem, however, for our dynamical transport measurements, as will be discussed in Chapter 3, because we are interested only in the measured properties when the array is in the resistive state and the magnetic fields can penetrate uniformly.

CHAPTER 3

CRITICAL CURRENTS IN FRUSTRATED ARRAYS

3.1 Introduction

In defining the critical current of a superconductor, one must distinguish between the intrinsic critical current I_{co}, which is the maximum supercurrent for which a metastable state exists, and the (lower) current I_{CR}, at which resistance becomes observable because of thermally activated processes.[1] Although I_{CR} has practical importance, it has neither fundamental significance nor a unique value, because it depends on the sensitivity of the experiment that defines it. It is the intrinsic I_{co} which enters into fundamental analyses, *including the theoretical determination of the onset of resistance.* The relation between I_{co} and I_{CR} was worked out long ago for single heavily damped Josephson junctions (by Ambegaokar and Halperin, 1969) and for one-dimensional filaments (by Langer and Ambegaokar, 1967 and McCumber and Halperin, 1970). However, this relationship is much less well understood in two-dimensional arrays of Josephson junctions or other weak links, because of the important and complicating role played by flux quanta in the description of an extended system. This type of system is currently attracting much attention as a model system for naturally occurring granular superconductors, particularly the high temperature superconductors. In this chapter[2] we address the issues of critical

[1]In this chapter, we use I_{co} instead of I_c to emphasize the fundamental nature of the intrinsic critical current. i_{co} is equivalent to the single junction i_c previously discussed in Chapters 1 and 2.

[2]A preliminary account of this work was given by Benz *et al.*, 1989 and much of this chapter has been submitted for publication in Phys. Rev. B, Benz *et al.*, 1990b.

currents and resistance in such arrays from both experimental and theoretical points of view.

In recent work in this laboratory, the rf response of arrays (Benz *et al.*, 1990) and the effects of pinning (Rzchowski *et al.*, 1990) have been investigated experimentally. The analysis of these data depend crucially on knowledge of the Josephson coupling energy E_J of the junctions of the array, or, equivalently, their intrinsic critical currents i_{co}, because the energy barriers to vortex motion and the characteristic frequency of the overdamped junctions are both proportional to this critical current (see Chapter 1). In this chapter we present new experimental measurements of the dynamic resistance at finite voltage as a function of both dc bias current and perpendicular magnetic field (or f) at a temperature far enough below $T_c(f)$ that the effects of thermally induced vortices, domains, and other defects are not important,[3,4] and yet not so low that the flux Li_{co} per cell has become comparable to Φ_0 (see Section 2.3).[5,6] We discuss how intrinsic unfluctuated critical currents *both for single junctions and for the array* may be extracted from these data by using the analogy with thermal activation of an overdamped particle in a periodic potential (Sections 3.2-3.4). These experimentally determined critical currents will be compared with theoretically predicted results in Section 3.5. And in Section 3.6 we will present a

---

[3]The magnetoresistance and I-V characteristics of overdamped arrays have previously been measured only very close to $T_c(f = 0)$: M.Tinkham *et al.*, 1983; Brown and Garland, 1986; Springer and Van Harlingen, 1987; Resnick *et al.*, 1984; Kimhi *et al.*, 1984; Gordon *et al.*, 1987.

[4]Arrays of underdamped junctions exhibit hysteretic I-V curves and behave very differently from overdamped arrays, although the field modulation of the subgap resistance, $R_0(f)$ behaves similarly to the magnetoresistance in underdamped arrays: Voss and Webb, 1982; Webb *et al.*, 1983; and van der Zant *et al.*, 1988.

[5]This is analogous to self-induced fields affecting the magnetic field modulation of the critical current in a dc SQUID: Tinkham, 1969, pp. 215-216 (see Section 2.3).

[6]At these temperatures the penetration depth for a perpendicular magnetic field is smaller than the array size. However, in the highly resistive regime of our measurements, the currents flow uniformly, and this is not an important effect (see Section 2.3).

new exact analytical calculation of the ground state critical current for the fully-frustrated case, f = 1/2, and a precise numerical calculation for f = 1/3.

3.2 Thermal Fluctuations in Single Josephson Junctions

As discussed in section 1.3, the junctions that make up our arrays are highly overdamped.[7] In 1969, Ambegaokar and Halperin theoretically determined the effect of thermal fluctuations on the current *vs.* voltage (i-v) characteristics of single junctions. Figure 3.1(a) shows a number of single junction i-v curves with various amounts of thermal noise as determined by the ratio of the zero-bias-current energy barrier to the temperature, $\Gamma = E_B/kT$, where $E_B = 2E_J = \hbar i_{co}/e$. Figure 3.1(b) plots the dynamic resistance *vs.* current for a single junction with amounts of thermal noise similar to the curves in Fig. 3.1(a). Using this theory it has been shown (Falco *et al.*, 1974) that a peak in dynamic resistance *vs.* current (dv/di *vs.* i) occurs at a current which is within a few percent (< 2%) of i_{co}, the intrinsic critical current in the absence of fluctuations, so long as fluctuation effects are small enough that the peak value of dv/di is at least 1.5 times larger than the high-current limiting value of dv/di. This can be seen in Fig. 3.1(b) for $\Gamma \geq 20$, where the temperature fluctuations are small enough that a prominent peak in the dynamic resistance is apparent.

Thus, for single junctions the position of this peak is a very good measure of the unfluctuated critical current. It is important to note that the *onset* critical current, i_{CR}, defined experimentally as the lowest current giving measurable voltage, would give a much poorer estimate of the *unfluctuated* critical current i_{CO}, because the relation between this i_{CR} and the intrinsic i_{CO}, as determined by Ambegaokar and Halperin, is strongly dependent on

[7]An overdamped junction has $\beta_c = 2ei_cR^2C/\hbar < 1$, where C is the capacitance of the junction. Our single junctions have negligible capacitance so that $\beta_c << 1$ (see Section 1.2).

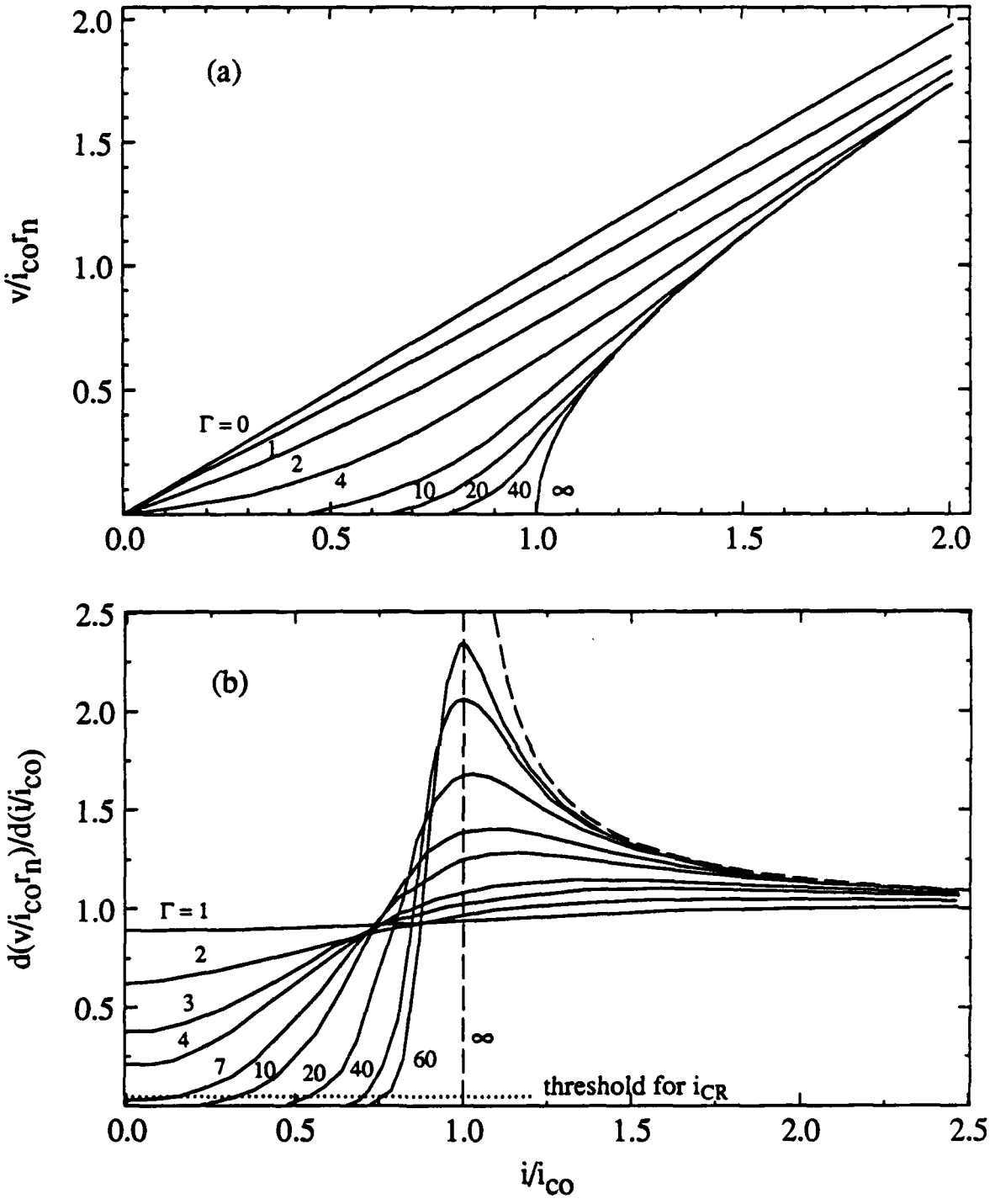

Fig. 3.1. (a) Single junction voltage *vs.* current curves with thermal fluctuation induced rounding as determined by Ambegaokar and Halperin (1969). $\Gamma = E_B/kT = \hbar i_{co}/ekT$ is the ratio of the energy barrier to the temperature, and determines the magnitude of the thermal fluctuations. (b) Dynamic resistance *vs.* current curves with thermal fluctuations similar to the i-v curves in (a) from Falco *et al.*, 1974. For large Γ the peak gives a very good estimate of i_{co}.

the ratio of the the energy barrier to the temperature, $\Gamma = \hbar i_{co}/ekT$. Figure 3.1(b) shows this effect very clearly; for example, the onset critical current, defined at the $0.05r_n$ resistance threshold indicated by the dotted line, will approach zero as thermal fluctuations are increased, *i.e.* as Γ decreases to 10, while the peak in dv/di stays near i_{co}. For higher voltage sensitivities, the onset critical current yields even worse estimates of i_{co}.

3.3 Experimental Array Results

3.3.1 Critical Currents in Strongly Commensurate Fields

Curve (a) in Figure 3.2 shows the dynamic resistance vs. current in zero field for our 1000 by 1000 array. (A description of the experimental measurement circuit can be found in Section 2.2) Notice that a prominent peak appears in this f = 0 curve at about 7mA. This can be understood as follows: In zero field, an N by M array behaves as a series-parallel network of identical single junctions, so that its I-V curve will be the same as that of a single junction, apart from scaling the current by M and the voltage by N, so that I = Mi and V = Nv, where i and v are the single junction current and voltage. The normal-state resistance of the array is related to that of the single junction by $R_n = (N/M)r_n$.

From the analysis on single junctions in Section 3.2, it follows that the measured current where the dynamic resistance of the array in zero field is a maximum should give a good estimate of the intrinsic unfluctuated critical current $I_{co}(T)$ of the *array*. This, in turn, should be related to the single junction critical current, i_{co}, simply by $I_{co} = Mi_{co}$, where M = 1000 is the number of junctions in parallel across the width of the array perpendicular to the current. This conclusion is supported by the fact that $i_{co} = I_{co}/M$ agrees within 10% with the i_{co}'s for the two single junctions fabricated on the same substrate with the array and measured in the same way. Further justification for using the peak to determine the

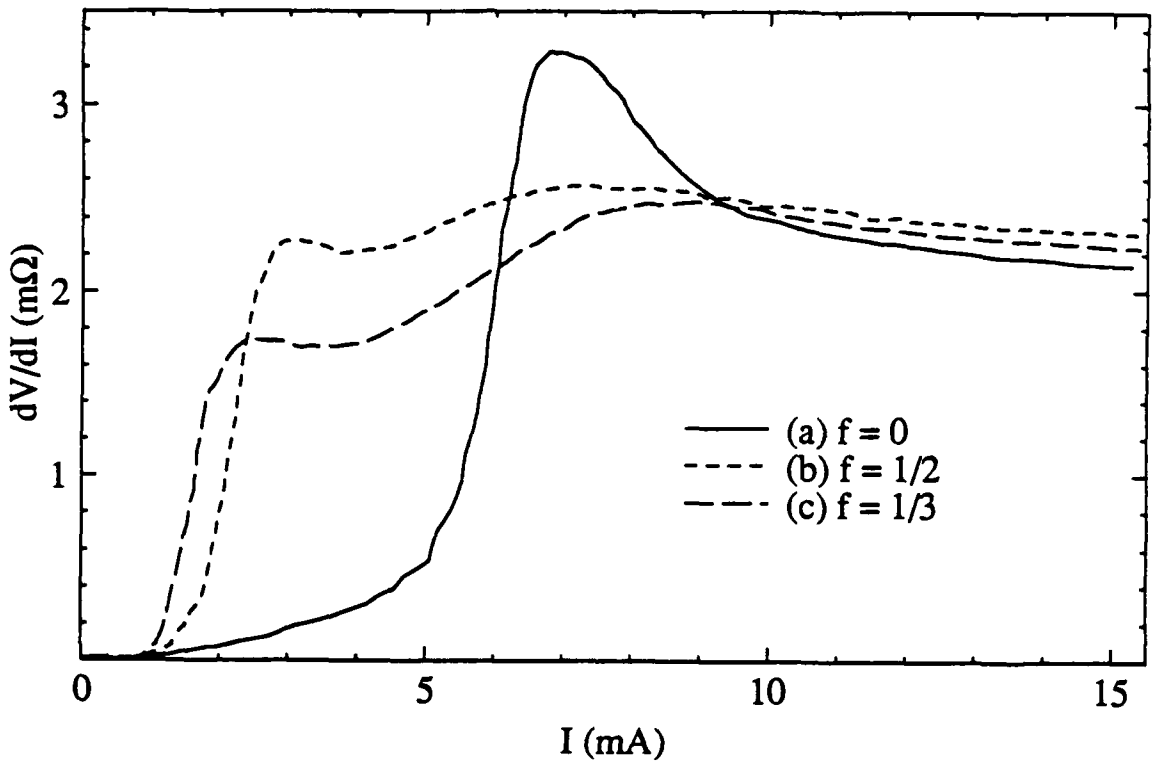

Fig. 3.2. Dynamic resistance *vs.* current for a 1000 by 1000 array at T = 2.09K for three commensurate perpendicular magnetic fields: a) f = 0, b) f = 1/2, and c) f = 1/3. The rms lock-in modulation current was 30μA. The data were taken on an XY recorder and then manually digitized for computer analysis.

unfluctuated array critical current follows from noting that the temperature dependence of the inferred array critical current follows the exponential temperature dependence (2.3.1) expected for the intrinsic critical current of a single weakly coupled SNS junction (De Gennes, 1964).

The dynamic resistance *vs.* current was found to vary greatly for different magnetic fields. Figure 3.2 also shows dV/dI *vs.* I for two commensurate magnetic fields, f = 1/2 and 1/3, at the same temperature as the f = 0 curve. The dV/dI *vs.* I curves for f = 2/3 and 1 (not shown) are nearly identical to the f = 1/3 and f = 0 curves, respectively, thereby establishing the symmetry about f = 1/2 and the periodicity for integer changes in f (see the theoretical predictions in Fig. 1.7(a) of Chapter 1). For these strongly commensurate magnetic fields, weaker local peaks in dV/dI occur at currents lower than that for the peak in zero field. By analogy with the single junction and f = 0 cases, we associate these peaks with the intrinsic unfluctuated critical currents for these f-values, $I_{co}(f)$. For other commensurate fields, where the vortex superlattice is less strongly coupled to the array, such as f = 1/4, 1/6, etc., we observe similar structure in the dynamic resistance at low currents, but the peaks are even less pronounced and have become only rounded inflection points, making it very difficult to make a quantitative inference of I_{co}. This structure will be discussed in more detail in Section 3.4.

3.3.2 Magnetoresistance

To obtain information about the dynamic resistance at fields other than the 'strongly commensurate' fields, the *magneto*resistance (dV/dI *vs.* f) was measured at temperatures well below $T_c(f)$ for various fixed bias currents; three such curves are shown in Fig. 3.3. Curve (a) shows the behavior at a current, 0.7mA, only slightly above the current at which the dynamic resistance first becomes measurable, I = 0.92mA ~ I_{CR}. Relative minima in the magnetoresistance are observed for f = 0, 1/6, 1/4, 1/3, 1/2, 2/3, 3/4, 5/6, and 1, each

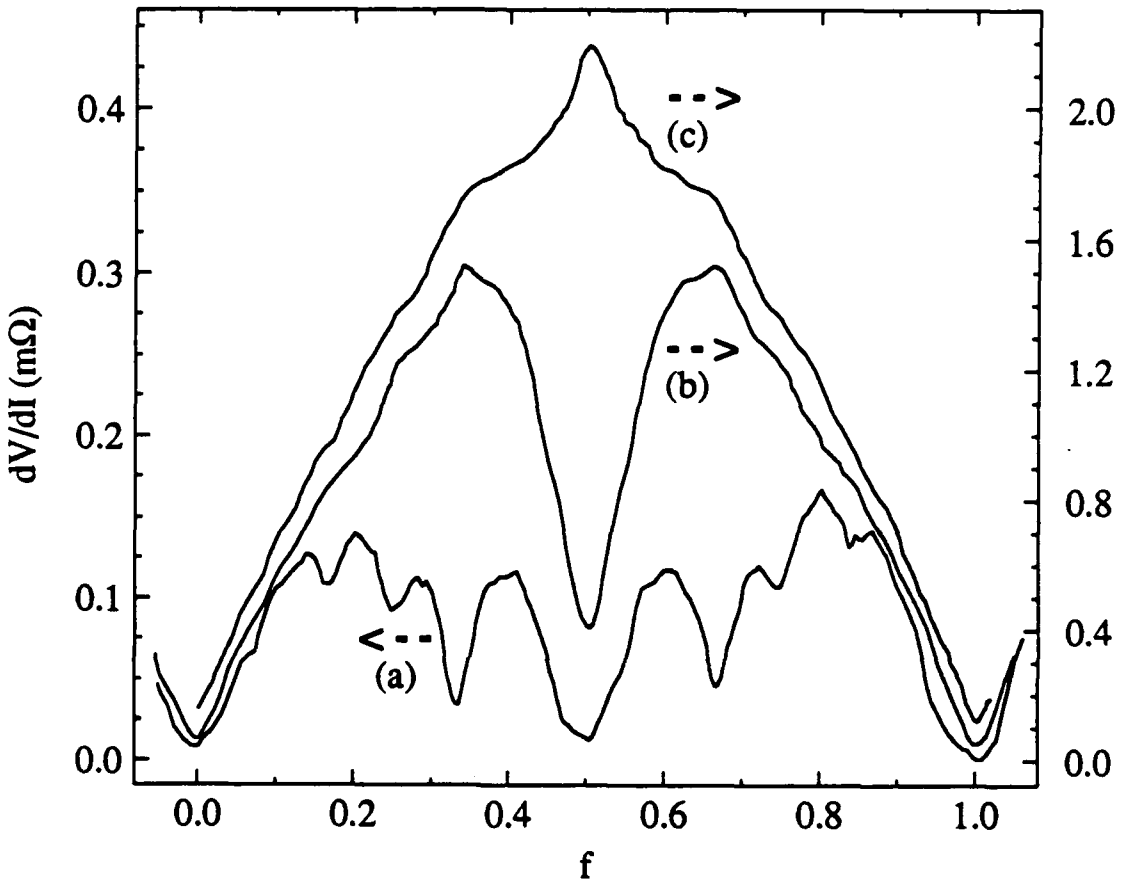

Fig. 3.3. Magnetoresistance at T = 2.09K for three different dc bias currents: a) 0.92mA, b) 1.84mA and (c) 2.79mA. Note that the left and right vertical scales differ by a factor of five. Minima in the dynamic resistance coincide with magnetic fields where the vortex superlattice is strongly commensurate with the array of junctions, namely f = 0, 1/6, 1/4, 1/3, 1/2, 2/3, 3/4, 5/6, and 1.

corresponding to a field where the vortex superlattice is strongly commensurate with the junction array (see discussion in Section 1.2). The symmetry around f = 1/2 is again apparent. As the bias current is increased from ~ I_{CR}, the relative *minima* evolve into relative *maxima*, beginning with the *least* 'strongly commensurate' fields which have the lowest values of $I_{co}(f)$. This is shown in curve (b) of Fig. 3.3 [taken at twice the current as curve (a)], in which weak relative maxima appear near all the commensurate fields except for f = 0, 1/2, and 1, which are the *most* 'strongly commensurate' fields. These subtle relative maxima in the magnetoresistance occur near the same currents and fields where the peaks are found in the dV/dI *vs.* I curves like those shown in Fig. 3.2. Curve (c), taken at still higher current, 2.79mA, shows the dramatic reversal of the dip at f = 1/2 into a maximum, which occurs for $I \sim I_{co}(f=1/2)$. This structure is best revealed when the data are plotted in three dimensions as in Fig. 3.4, which shows dV/dI as a function of both magnetic field and dc bias current.

3.3.3 Dynamic Resistance *vs.* Magnetic Field and *vs.* Bias Current

Figure 3.4 consists of *experimental data*, digitized from dV/dI *vs.* f curves (including those in Fig. 3.3) at small increments of dc current. The dV/dI *vs.* I curves of Fig. 3.2 can be reproduced from this data, as can be seen by comparing the nearest edge of the 3D plot (f = 0) with curve (a) in Fig. 3.2. The symmetry about f = 1/2 is again apparent from this graph. Similar structure is observed between all integer f. However, at substantially higher fields (not shown), a reduction in the array critical current is observed, due to field penetration into the single junctions (Tinkham, 1975, p. 199). The critical current is approximately zero at a field of f = 9, which accurately corresponds to one quantum of flux threading each junction. This, however, is not a substantial effect for the small fields, $0 < f < 1$, shown in Figure 3.4 (see also Forrester, 1988, pp. 59-67).

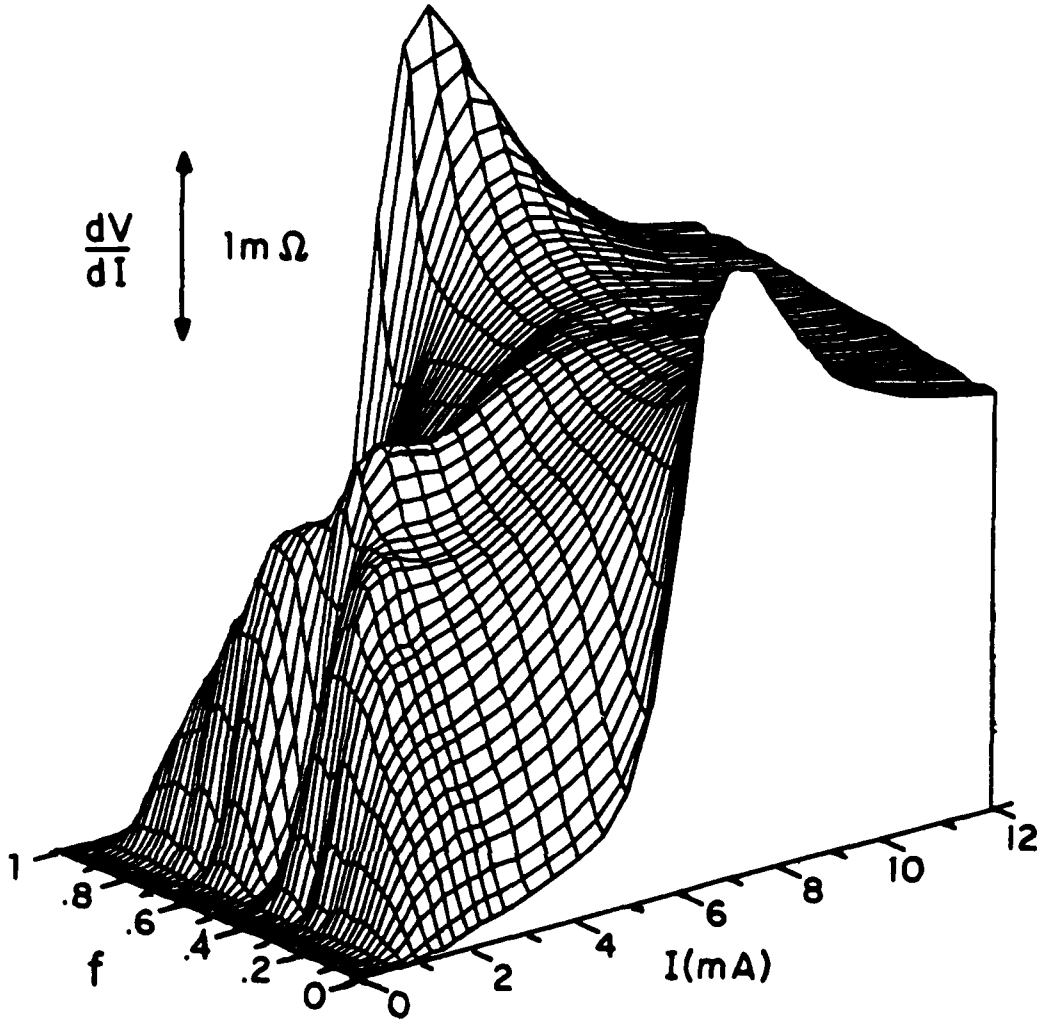

Fig. 3.4 *Experimental* data showing the detailed dependence of the dynamic resistance on both dc bias current and perpendicular magnetic field. The data were taken from dV/dI *vs.* f curves at fixed bias currents, digitized and then interpolated to retrieve points at convenient intervals along the f- and current-axes.

3.4 Discussion of Experimental Results

A number of important features are apparent from the experimental data plotted in Figure 3.4, all of which can be explained qualitatively by considering the array of junctions to generate a periodic 2D 'egg-carton' pinning potential (see Section 1.2), in which, given thermal activation,[8] field-induced vortices can move in response to a Lorentz force proportional to the dc bias current. At 'strongly commensurate' fields, the vortex superlattice is strongly coupled to the array and not easily depinned. In Fig. 3.4 it is seen that the peaks in the dynamic resistance indicating critical current values are associated with the commensurate fields, and that the heights of the peaks get smaller for the less 'strongly commensurate' fields, starting from f = 0 and 1, to f = 1/2, and then to f = 1/3, etc. We identify the current at these peaks, like those shown in Fig. 3.2, with the depinning current of the vortex superlattices from the periodic 2D potential.[9] This identification is reasonable because thermally activated motion of vortices in a periodic potential due to a Lorentz force is qualitatively similar, as shown explicitly by Rzchowski *et al.* (1990), to the thermally activated behavior for a single junction as described by Ambegaokar and Halperin. More simply, it is plausible on physical grounds that the underlying critical current should be found at the current at which the resistive voltage increases most steeply. If we choose the positions of the peaks as estimates for the array critical current for these magnetic fields, and compare with the zero field case, we find $I_{co}(f=1/2) \approx 0.42 I_{co}(f=0)$ and $I_{co}(f=1/3) \approx$

[8]AC response measurements by Leeman *et al.* (1986), have shown effects of thermal activation on pinning at various temperatures.

[9]Our model assumes that the array is uniform and that the entire superlattice depins and moves across the array. For arrays with non-identical junctions or some other form of disorder, the motion may be more complex, including effects such as vortex lattice shear. At higher temperatures close $T_c(f)$ the motion of domains or other thermally induced defects (see Mon and Teitel, 1989) will contribute to the dissipation and may also destroy the superlattice.

$0.34I_{co}(f=0)$. As we shall see in Sections 3.5 and 3.6 of this chapter, these experimental critical currents are in reasonable agreement with theoretically calculated critical currents.

The curves in Fig. 3.3 can now be explained. The Lorentz force, due to the dc current, has the effect of tilting the 2D 'egg-carton' potential. The energy barriers to motion of the vortex superlattice differ for the different commensurate fields, depending on the coupling strength between the vortex superlattice and the array. For fields f near the 'strongly commensurate' fields f_{sc} it has been suggested (Teitel and Jayaprakash, 1983b and Rzchowski *et al.*, 1990) that unpaired, field-induced vortices or some other form of defects dominate the dynamic resistance as they are thermally activated and driven by the Lorentz force. Since the number of these defect vortices is proportional to $|f-f_{sc}|$, the resistance rises approximately linearly on either side of the minimum at f_{sc}. The small *maxima* in the magnetoresistance at commensurate fields f_{sc}, particularly in the higher current plots 3.3(b) and 3.3(c), signify that the bias current is very close to the depinning current, $I_{co}(f_{sc})$, for those particular commensurate fields, *i.e.* the energy barriers to vortex motion have been reduced to near zero by the current.

At very high currents all the barriers to vortex motion are reduced to zero and the array is in a flux-flow regime where all of the field-induced vortices are depinned and flowing down the tilted 2D potential. This regime can be seen in Fig. 3.4 for fixed currents between the f = 1/2 and f = 0 critical currents, where the dynamic resistance is rising nearly linearly as a function of field between f = 0 and f = 1/2 as would be expected in the flux flow regime of a type II superconductor. The slope of this line, $\sim 2.3R_n$, is in good agreement with the value $2R_n$ obtained by considering the viscous drag on each vortex (Rzchowski, *et al.*, 1990). Between f = 1/2 and f = 1 the dynamic resistance *decreases* linearly because now vortices of the opposite sign dominate, as discussed in Section 1.2, and their number is decreasing as f = 1 is approached. Curve (c) in Fig. 3.3 is at a current just below this regime, but still shows the nearly linear behavior on either side of f = 1/2. At currents far above the zero-field critical current, $I_{co}(f = 0)$, the behavior of the array is

dominated by the normal shunt resistance of the copper in the junctions, so the dynamic resistance is essentially independent of both current and magnetic field.

The next interesting feature is that the dynamic resistance is not appreciable for any value of f when the dc current $I \leq 0.1I_{co}(f = 0) \approx 0.7\text{mA}$. We believe this feature is related to the pinning energy of individual vortices in the array as calculated by Lobb *et al.* (1983), $E_B = 0.2E_J$. As verified by simulations (Straley, 1988; Lee *et al.*, 1989; and Rzchowski *et al.*, 1990), the current required to depin a solitary vortex in the absence of thermal activation is $0.1i_{co}$ per junction, which is in agreement with our observed total array current of $0.1I_{co}(f=0)$. The fact that we observe this same minimum depinning current for *all* fields, and not just for small fields near f = 0, suggests that the depinning current for field-induced defects is $\sim 0.1i_{co}$ per junction near other f_{sc} values as well. The differential resistance peak associated with the depinning of these defects is very small because the dissipation due to the motion of a small number of defects, $\propto |f-f_{sc}|R_n$, is very small, thus forcing us to use a resistive onset criterion in this case. At much lower temperatures this zero-dissipation plateau region becomes larger due to self-induced field effects in the array.[10]

3.5 Comparison with Theory

Theoretical estimates for the critical currents of an array in commensurate magnetic fields have been obtained by a number of different methods. Teitel and Jayaprakash (1983b) used Monte Carlo simulations with a twisted-phase method to induce a dc current in order to determine the zero-temperature ground state critical current for various fields. Shih and Stroud (1985) used a molecular-field approximation with the twisted-phase

[10]At these lower temperatures, self-induced fields are generated by the larger currents in the array because of the geometrical inductance, L, associated with the array unit cells (see Section 2.3). The plateau region is approximately 50% of $I_c(f=0)$ at T = 1.65, giving an estimate for $L \approx 10\text{pH}$.

method and found similar critical currents. From their published data we find their critical current estimates for f = 1/2 and f = 1/3 to be $I_c(f = 1/2)/I_c(f = 0) \approx 0.41 \pm 0.01$ and $I_c(f=1/3)/I_c(f = 0) \approx 0.26 \pm 0.01$. We have made exact critical current calculations for both of these fields by calculating the current dependence of the gauge invariant phase difference across each junction. This method is discussed in Section 3.6 in detail for f = 1/2, and sketched for f = 1/3. From these calculations we find analytically $I_{co}(f = 1/2)/I_{co}(f = 0) = \sqrt{2}-1 = 0.41421$ and $I_{co}(f = 1/3)/I_{co}(f = 0) = 0.26789$. Similar results were found numerically by Halsey (1985). The results of the simulations mentioned above are in excellent agreement with these exactly calculated values. For convenience of comparison, the measured, exactly calculated, and simulated critical current ratios are all collected in Table I.

Table I. Comparison between measured, exactly calculated, and numerically simulated critical currents.

f	$I_c(f)/I_c(0)\|_{meas}$	$I_c(f)/I_c(0)\|_{exact}$	$I_c(f)/I_c(0)\|_{sim}$
0	1	1	1
1/2	0.42 ± 0.02	0.414214	0.41 ± 0.01
1/3	0.34 ± 0.02	0.26789	0.26 ± 0.01

The estimated critical current ratio for f = 1/2 from our experimental measurements (~0.42) is also in excellent agreement with the exact critical current, but for f = 1/3 the peak in the dynamic resistance appears at a current (~0.34) that exceeds the theoretical value. The position of the rounded peaks in Fig. 3.4 for the other less 'strongly commensurate' fields also appear to overestimate $I_{co}(f)$ compared to the simulated zero-temperature values. A possible reason for this discrepancy is that the peaks are more rounded for the less

'strongly commensurate' fields, probably due to more thermal activation over their lower energy barriers. In the Ambegaokar and Halperin model (Section 3.2), for smaller values of $\Gamma = E_B/kT$ the peak in dv/di is suppressed in magnitude and shifts toward currents slightly higher than i_{co} (see Fig. 3.1(b) for $\Gamma \leq 10$); the analogous effect in arrays would cause our use of the measured position of the peak to also yield an overestimate of $I_{co}(f)$ for the 'less strongly commensurate' fields due to small values of $E_B(f)/kT$. Non-uniformities in the array may also contribute to the rounding of these peaks because at the 'less strongly commensurate' fields the vortices interact more weakly over the larger separation distances, and thus they may be more susceptible to variations in junction coupling energies and other non-uniformities.

3.6 Analytic Solutions for f = 1/2 and f = 1/3

We have made an exact calculation of the critical current for the f = 1/2 ground state using periodicity and other symmetry arguments to restrict the number of independent gauge-invariant phase differences across the junctions in an infinite array. In our solution, we assume that, as for the zero-current ground state, the current-carrying ground state is made up of vortex superlattice cells of size 2 × 2 junctions, and that the phase differences deform continuously in response to a net imposed current until the intrinsic critical current is reached, above which no static solutions exist. This ground state configuration is shown in Fig. 3.5, where the gauge-invariant phase differences across the four non-equivalent junctions are denoted by α, β, β', and γ. For zero net current, all of these phases are equal to $\pi/4$. A net current applied from left to right will break the symmetry of the ground state, so that α and γ will have different values. If there is no net current in the vertical direction, symmetry requires that $\beta = \beta'$.

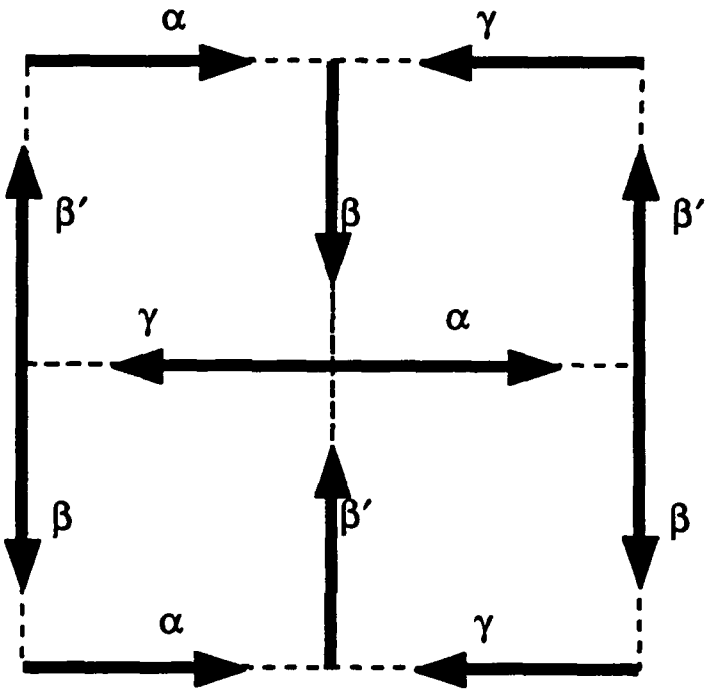

Fig. 3.5 Ground state 2x2 superlattice unit cell for f = 1/2, showing the positions of the gauge-invariant phases, α, β', β, γ, used to accommodate a net dc bias current in the horizontal direction. By symmetry, β' must equal β when there is no net current in the vertical direction. The shaded arrows represent ground state supercurrents across the junctions and have equal magnitude $i_{co}/\sqrt{2}$ for zero dc current bias. The lines between the vertices correspond to the junctions between the superconducting islands.

With these assumptions we can write down the following constraining equations. For f = 1/2, fluxoid quantization requires that

$$\alpha + \gamma + 2\beta = \pi \pmod{2\pi} . \tag{3.6.1}$$

Current conservation at each node in the array is satisfied if

$$\sin\alpha + \sin\gamma = 2\sin\beta . \tag{3.6.2}$$

Finally, the average net current per junction in the horizontal direction, normalized to the single junction critical current, is

$$\frac{i}{i_{co}} = \frac{1}{2}(\sin\alpha - \sin\gamma) . \tag{3.6.3}$$

Solving these equations for the net current as a function of the total gauge-invariant phase difference across the 2x2 cell parallel to the current, $\varphi = \alpha - \gamma$, we find

$$\frac{i}{i_{co}} = \frac{\sin\varphi}{(6+2\cos\varphi)^{1/2}} = \frac{\sin(\varphi/2)}{\left[1+\sec^2(\varphi/2)\right]^{1/2}} . \tag{3.6.4}$$

The maximum current per junction that can be carried in this state is $i_{co}(f=1/2) = (\sqrt{2}-1)i_{co}(f=0)$, as can be found by differentiating this expression; this occurs for $\varphi = 2\arcsin(2-\sqrt{2})^{1/2} \approx 99.88^{o}$. It is interesting to note that (3.5.4) describes a current-phase relation $I(\varphi)$ that is similar to the single-junction current-phase relation $i = i_{co}\sin\varphi$ except that now φ denotes the total gauge invariant phase across the 2x2 vortex superlattice unit cell, and the maximum supercurrent is only $(\sqrt{2}-1)i_{co}$ per junction, or twice that

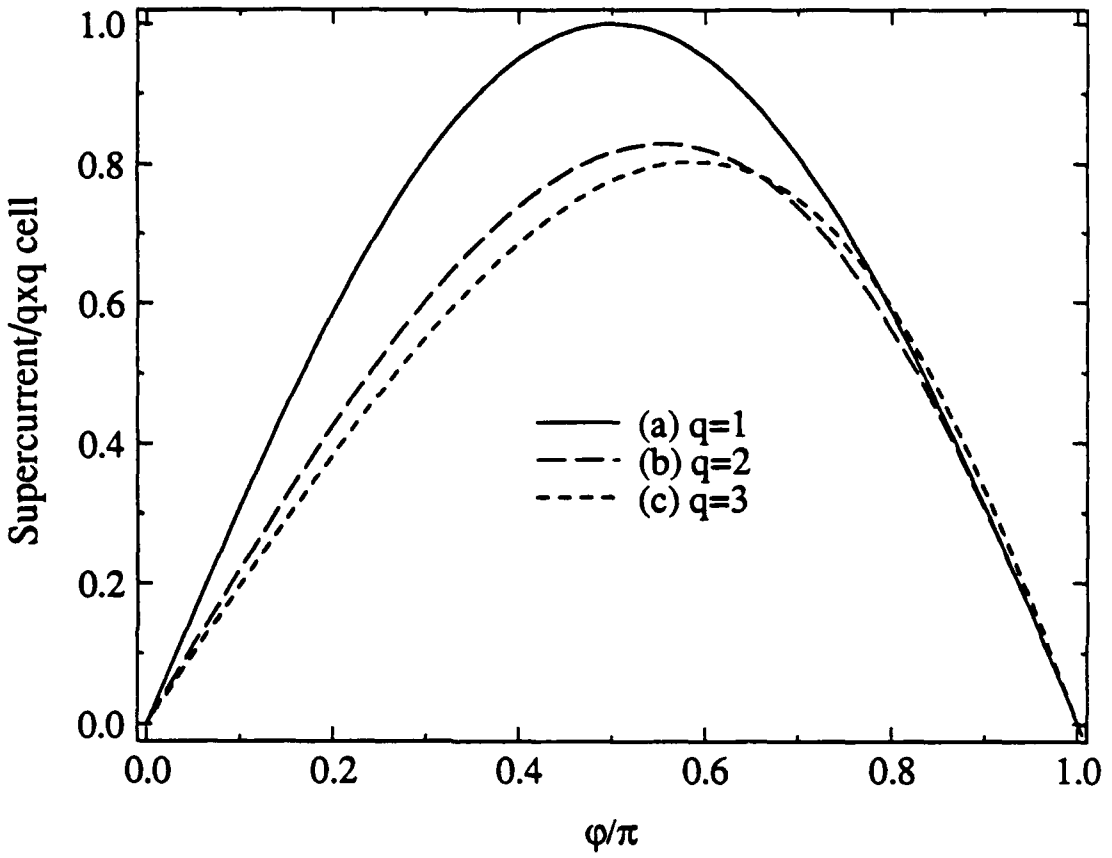

Fig. 3.6 Comparison of current-phase relation for a single junction, for a 2x2 superlattice cell for f = 1/2, and for a 3x3 cell for f = 1/3. The maximum values (0.828 and 0.804) of the curves for f = 1/2 and 1/3 correspond to 0.414 and 0.268 per junction as explained in the text. The gauge-invariant phase difference φ occurs across a single junction for f = 0, but is distributed over two or three junctions in series in the 2x2 or 3x3 cells, respectively. Only half of a complete cycle is shown, to allow detailed features to be more clearly seen.

(*i.e.*, $I_{co}(f=1/2) = 2i_{co}(f=1/2) = 0.82843\ i_{co}$) per 2x2 cell. This current-phase relation for the 2x2 cell is compared with that for a single junction in Fig. 3.6.

The gauge-invariant phases and hence the currents for each of the junctions can be worked out from this solution, with the following results:[11]

$$\sin\alpha = [1 + \sec^2(\varphi/2)]^{-1/2}\,[1 + \sin(\varphi/2)] \qquad (3.6.5a)$$

$$\sin\beta = [1 + \sec^2(\varphi/2)]^{-1/2} \qquad (3.6.5b)$$

$$\sin\gamma = [1 + \sec^2(\varphi/2)]^{-1/2}\,[1 - \sin(\varphi/2)] \qquad (3.6.5c)$$

The sign ambiguity of the square root is resolved by imposing a requirement of continuity. the supercurrents for each of these junctions are plotted in Fig. 3.7 as a function of the total gauge invariant phase, φ.

We have carried out similar (but more intricate) calculations for the f = 1/3 ground state. Here one must determine five independent gauge-invariant phase differences within the 3x3 cell, compared to three in the 2x2 cell for f = 1/2. Although we were not able to find an analytic expression for the maximum supercurrent per junction, it was found numerically to be $i_{co}(f=1/3) = (0.26789)i_{co}(f=0)$. Referred to the 3x3 superlattice cell, the maximum supercurrent is three times this (*i.e.*, $I_{co}(f=1/3) = 3i_{co}(f=1/3) = 0.80367i_{co}$), and occurs at a gauge-invariant phase difference of about 105.23°. The current-phase relation for the f = 1/3 (3x3) superlattice unit cell was calculated numerically and is also plotted in Fig. 3.6.

Comparing the three exact current-phase solutions plotted in Fig. 3.6, for f = 0, 1/2, and 1/3, we note that the maximum supercurrent *per superlattice cell* drops only from 1 to 0.828 to 0.804, and that this maximum occurs at a gauge-invariant phase difference *per*

---

[11]The fact that α, β, and γ depend only on $\varphi/2$, implies that their periodicity in φ is over 4π, while (3.5.4) shows that the *average* net current per junction is periodic over 2π. This difference reflects an internal period doubling in the case of ac drive as found in the "fractional giant Shapiro steps" at f = 1/2 discussed in Chapters 4 and 5.

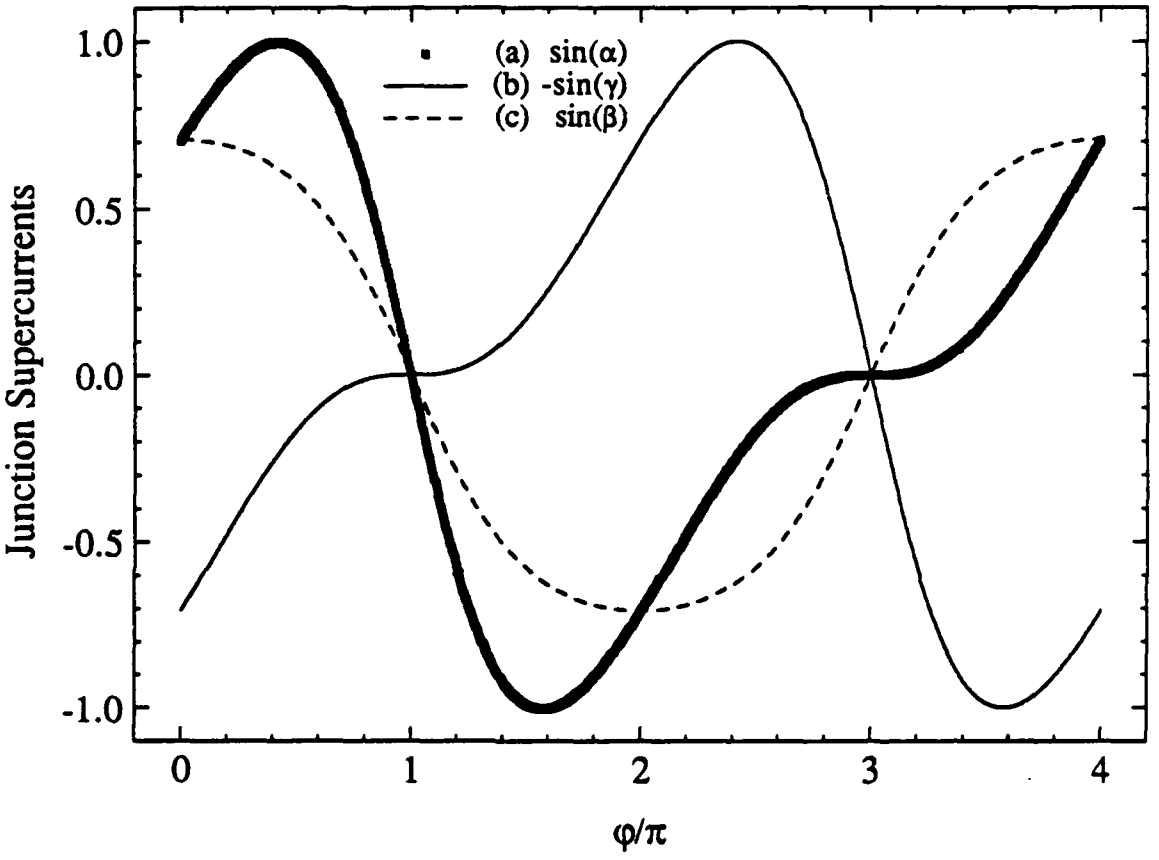

Fig. 3.7. Supercurrents for single junctions *vs.* total gauge-invariant phase across 2x2 superlattice unit cell from (3.5.5a-c): (a) sin(α), (b) -sin(γ), and (c) sin(β). Note that the currents are periodic in 4π as opposed to the average net current plotted in Fig. 3.6 which is periodic in 2π, and that sin(α) and -sin(γ), the currents in adjacent junctions parallel, to the dc bias current are identical but out of phase by 2π.

superlattice cell that increases only from 90° to 100° to 105°. Thus, the effect of the superlattice on the macroscopic response of the array is a sort of renormalization, in which each qxq superlattice cell can be approximately replaced by a 1x1 cell in an array with q-fold larger lattice interval, but rather similar $I_{co}(f) = qi_{co}(f)$ and an approximately sinusoidal current-phase relationship.

These exact current-phase relations can also be used to calculate the zero-temperature helicity modulus, Y, discussed in Section 1.3. The helicity modulus is the change in the free energy of the array in response to a phase twist, γ, applied across the array, in the limit that the twist goes to zero, *i.e.* $Y = \lim_{\gamma \to 0} \partial^2 F / \partial \gamma^2$. The current phase relation is related to the energy by $I(\gamma) = \partial F / \partial \gamma$ (Tinkham, 1975, p. 211), so that $Y = \lim_{\gamma \to 0} \partial I(\gamma) / \partial \gamma$. The total gauge invariant phase, φ, across the superlattice unit cell is essentially a phase twist, to that the slope of the I-φ relations in Fig. 3.6 where $\varphi = 0$ should give the T = 0 helicity modulus for the commensurate fields f = 1/2 and 1/3. From the exact calculations, we find $Y(f=1/2) = 0.7071\ E_J(0)$ and $Y(f=1/3) = 0.6315\ E_J(0)$. These results are in excellent agreement with the values found using Monte Carlo simulations and shown in Fig. 1.2, where $Y(f=1/2) = (0.707 \pm 0.001)\ E_J(0)$ and $Y(f=1/3) = (0.633 \pm 0.003)\ E_J(0)$.

3.6 Conclusion

Systematic measurements of the dynamic resistance of a 2D square array of Josephson junctions have shown it to be a complicated function of both bias current and perpendicular magnetic field. We have consistently explained the major features of this dynamic resistance within a model of the motion of 'strongly commensurate' vortex superlattices in the 2D 'egg-carton' pinning potential of the junction array. This model enabled us to make experimental estimates of the *intrinsic* critical current of the array in commensurate magnetic fields, which we find to be in quite good agreement with exact

theoretical values. The results of the exact calculations for f = 1/2 and 1/3 superlattice states suggest the conceptual usefulness of a renormalized array picture. This work complements previous investigations of the resistive dissipation in Josephson junction arrays in zero field near the Kosterlitz-Thouless transition temperature and near the phase transition temperatures for the commensurate magnetic fields. Taken as a whole, these investigations present a fairly complete and unified picture of the dc properties of 2D Josephson junction arrays over a wide range of temperature, current, and magnetic field. The next two chapters (4 and 5) will discuss the ac properties of the arrays in commensurate magnetic fields when driven with rf as well as dc bias currents.

CHAPTER 4

AC PROPERTIES: EXPERIMENT

4.1 Introduction

We have performed experimental measurements[1] of the response of large two-dimensional (2D) arrays of superconducting-normal-superconducting (SNS) junctions to radio-frequency (rf) currents, $i_{rf}\sin(2\pi\nu t)$, and have found interesting and novel phenomena. When an rf current is applied to a single Josephson junction, Shapiro steps occur in the dc i-v characteristics at voltages $v_n = nh\nu/2e$, where n is an integer (Shapiro, 1963). We have observed *giant* Shapiro steps[2] in large square arrays in zero field occurring at voltages

$$V_n = nN\left(\frac{h\nu}{2e}\right), \qquad n = 0,\ 1,\ 2,..., \tag{4.1.1}$$

where N = 1000 is the number of junctions in the direction of applied current. This indicates that substantially all of the junctions are on the n'th step at the same time and that the junction phases are locking to the rf current.

In the presence of a uniform perpendicular magnetic field, these giant Shapiro steps are drastically altered when the vortex superlattice created by the field is *commensurate* with the underlying junction lattice (see Section 1.4). The most prominent commensurate states

---

[1]Most of the results presented in this chapter have been published in Benz *et al.*, 1990a.

[2]This zero-field effect has been observed previously in hexagonal arrays above the resistive transition by Leeman *et al.* (1984), and earlier in small 5x5 arrays of Nb spheres by Clark (1973).

in a square array occur when the applied magnetic field is such that the number of flux quanta per unit cell, f = p/q (where p and q are integers), is f = 0, 1/4, 1/3, 1/2, 2/3, 3/4 and 1 (as shown in Chapter 1). When the vortex superlattice is in one of these 'strongly commensurate' states and an rf current is applied, we observe *fractional* giant Shapiro steps at voltages

$$V_n = n\left(\frac{N}{q}\right)\frac{h\nu}{2e}, \qquad n = 0,\ 1,\ 2,.... \tag{4.1.2}$$

These fractional giant Shapiro steps depend on the superlattice unit cell size, q, and can be understood by considering the motion of the vortex superlattices in response to the applied rf currents. In this chapter we will describe the behavior of the giant Shapiro steps described by (4.1.1) and show that the novel *fractional* giant steps of (4.1.2) are the result of collective vortex motion across the 2D array locking to the rf drive current.[3]

The fabrication of our Nb-Cu-Nb junction arrays and measurement apparatus is described in detail in Chapter 2, but will be briefly summarized here. The arrays are made with 0.2μm thick niobium islands on 0.3μm thick copper films deposited on a sapphire substrate. The cross-shaped niobium islands are formed by reactive ion etching and have a 2μm separation defining the junction length and a lattice constant of 10μm. Two single junctions with the same geometry as the junctions in the array are made concurrently on the same substrate. Both the single junctions and the square arrays have the same normal state resistance (~2mΩ), determined primarily by the copper. Using a four-point measurement circuit with a lock-in amplifier, the dynamic resistance, dV/dI, of the array was measured versus dc voltage for different external magnetic fields, rf frequencies, rf amplitudes, and

[3]Interesting related quantum interference effects due to vortex motion have been observed in type-II films by Fiory (1971), and in periodic 1-dimensional thickness-modulated films by Martinoli *et al.*, (1975). In the latter, the Abrikosov vortex lattice at certain magnetic fields couples to the spacing of the grooves, leading to an expression for the dc electric field that is proportional to the spacing and the magnetic field.

temperatures. The data on arrays presented in this chapter were taken at temperatures well below the Kosterlitz-Thouless transition to minimize the effects of thermally excited vortices near this phase transition, as discussed in Chapter 1. The dynamic resistance, dV/dI, was measured as a function of either current or voltage to more clearly expose the thermally rounded step structure of the I-V curves. The measurement circuit used is that shown in Fig. 2.4b of Chapter 2. The rf power coupled into the sample is limited by its low impedance (~2mΩ) and by high frequency noise filtering from the twisted-pair measurement leads. The critical current of the array at a given temperature, $I_c(T)$, is taken as the current where the dynamic resistance is a maximum from the measured dV/dI *vs.* I curve as discussed in Chapter 3.

In this chapter we will describe the experimentally observed dynamical properties of 2D arrays when driven with rf currents. We will begin (in Section 4.2) by discussing the rf properties of the individual SNS Josephson junctions that form the building blocks of the array, followed in Section 4.3 by a description of the results of our measurements on arrays. In Section 4.4 we will describe the vortex motion model that we believe explains these novel results, and in Section 4.5 we will discuss some of the more interesting details of the measurements as well as the implications of our vortex motion model.

4.2 Single Junction Properties

The rf properties of arrays are greatly influenced by the behavior of the single junctions in the array. When rf currents are applied to single junctions, steps appear in the dc i-v curves when the Josephson frequency, determined by $\nu_J = 2ev/h$, locks to the applied rf frequency, ν. This will occur when ν_J is equal to ν and also when it is a harmonic of the drive frequency, $\nu_J = n\nu$, giving rise to steps when the average (dc) voltage across the junction equals $nh\nu/2e$. Three experimental i-v curves for one of our single

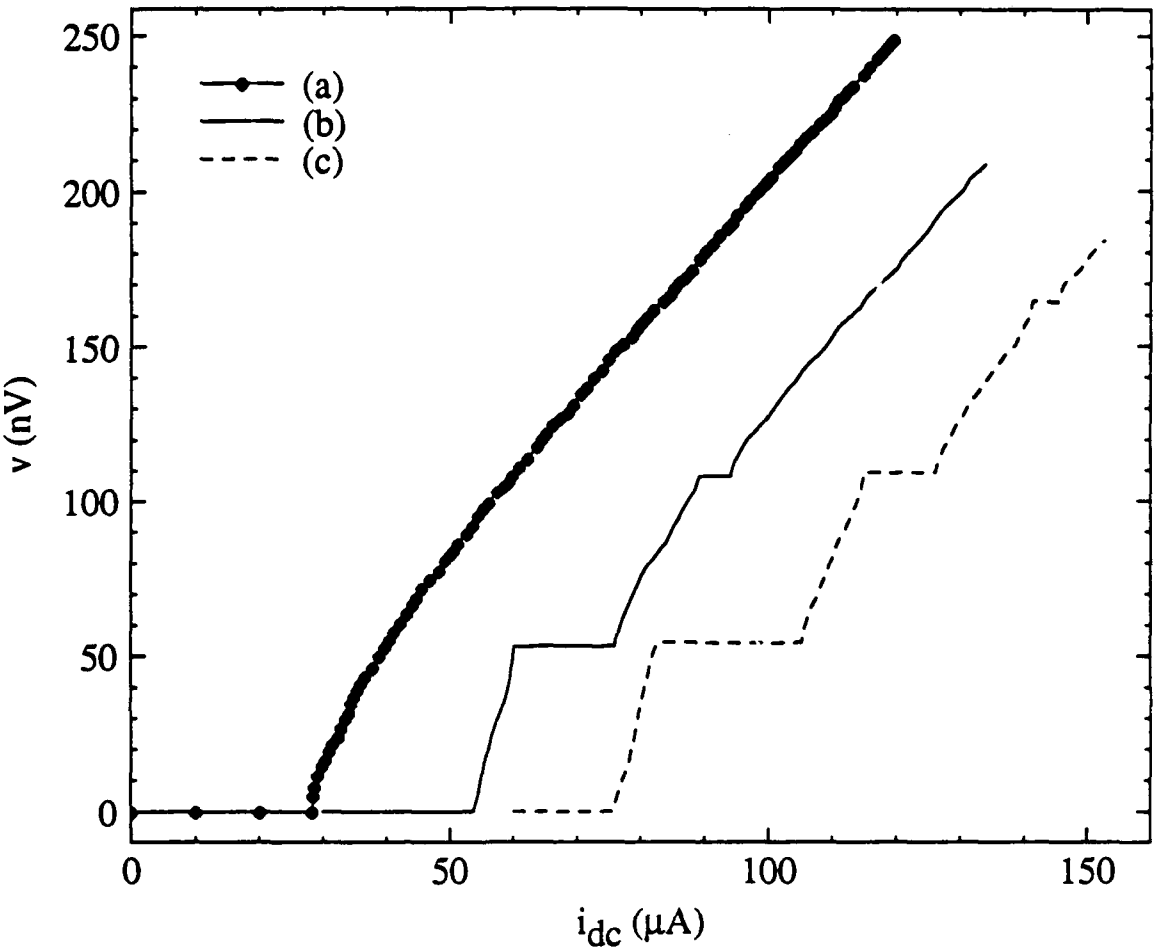

Fig. 4.1. Experimental single junction voltage *vs.* current with $\nu = 27\text{MHz} = \nu_c$ ($\Omega = 1$) at T = 1.35K for three different rf voltage (source) amplitudes: (a) $V_{rf} = 0$, (b) $V_{rf} = 0.6\text{mV}$, and (c) $V_{rf} = 1.0\text{mV}$. Curves (b) and (c) are displaced along the current axis by 30μA and 60μA respectively. Shapiro steps are seen at voltage intervals of 55.9nV.

junctions when driven with rf currents are shown in Fig. 4.1. Constant voltage steps are clearly seen at the appropriate intervals of 55.9nV for this 27MHz frequency.

The details of the junction's response are highly dependent on the characteristics of the junctions, and also on the rf power level and rf frequency that are applied. The characteristic frequency of the *single* overdamped junctions in our arrays, as discussed in Chapter 1, is $\nu_c = r_n/2\pi L_J = 2ei_c(T)r_n/h$, where r_n is its normal state resistance, L_J is the Josephson inductance, and $i_c(T)$ is its temperature-dependent, intrinsic critical current (without fluctuations), as discussed in Chapter 3. By considering the RSJ model circuit with zero capacitance discussed in Section 1.2 (Fig. 1.1a), we can see that when $\nu > \nu_c$, the non-linear Josephson element has a much higher impedance than the linear resistive element, *i.e.* $2\pi\nu\ L_J > r_n$, so that most of the rf current flows through the resistor, effectively ac voltage biasing the Josephson element. Thus, ν_c marks the crossover between the effectively ac voltage-biased ($\nu > \nu_c$) and ac current-biased ($\nu < \nu_c$) regimes, and will be used to define the reduced drive frequency, $\Omega = \nu/\nu_c$.

The response of the overdamped junction is very different in these two frequency regimes. The RSJ model can be used to calculate the i-v curves of the junction in the presence of rf current for these two cases. When rf currents are included in the RSJ model, the current equation (1.2.1) becomes

$$\frac{v}{r_n} + i_c\sin(\phi) = i_{dc} + i_{rf}\sin(2\pi\nu t)\,. \qquad (4.2.1)$$

The voltage across the junctions, including both the time-averaged dc voltage and the time-dependent voltage, can be determined numerically from this equation and the Josephson voltage relation (1.2.2), $v = (\hbar/2e)d\phi/dt$, as will be shown in Chapter 5 for arrays. The dynamics of the junctions, described by these equations, have also been investigated using an analog simulator by Russer (1972). For $\nu >> \nu_c$, the effectively ac voltage-biased

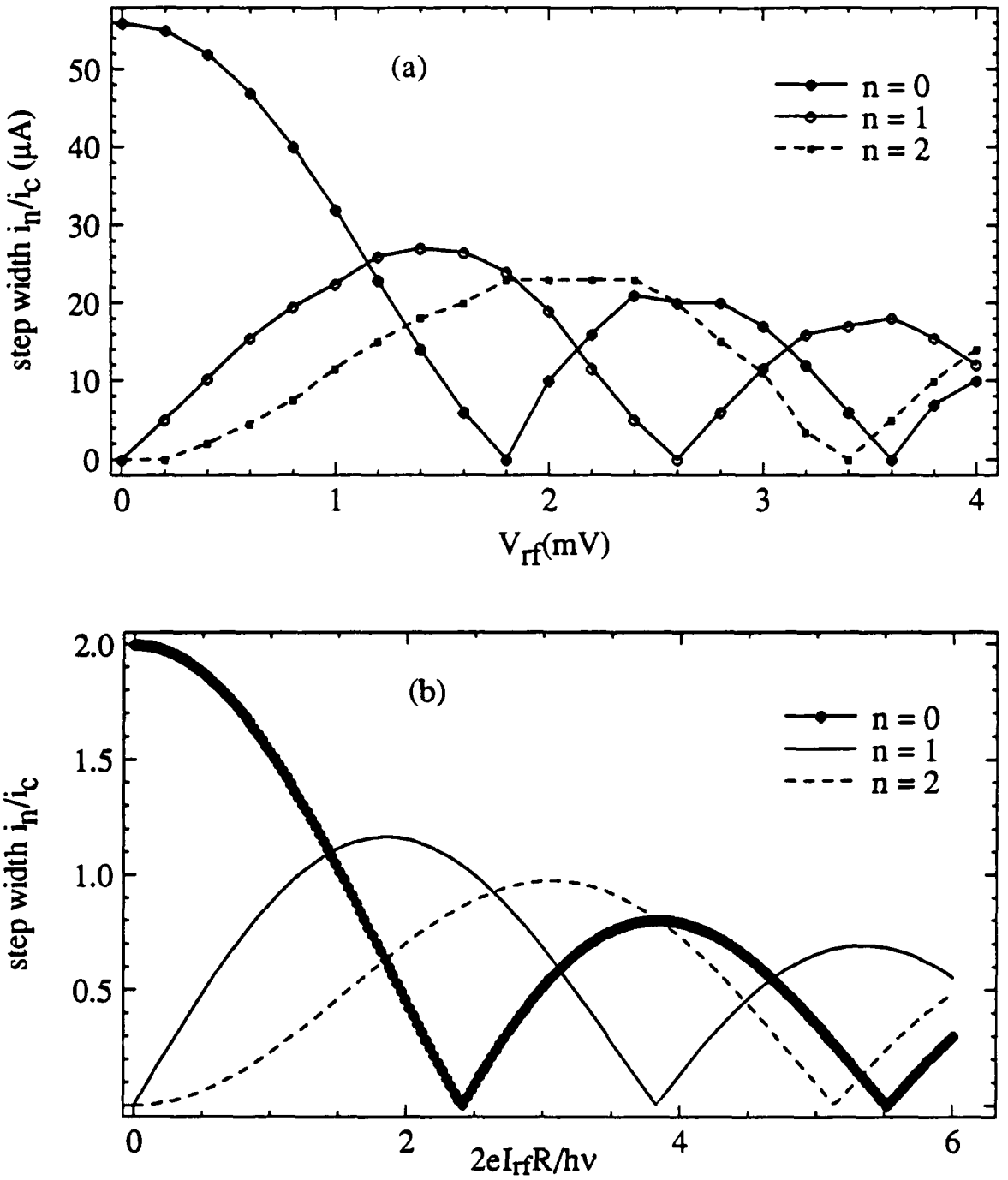

Fig. 4.2. (a) Experimental single junction step widths *vs.* rf voltage (source) amplitude, for $\nu = 27\text{MHz} = \nu_c$ ($\Omega = 1$) at T = 1.35K. V_{rf} is the voltage amplitude from the rf source. (b) Theoretical Bessel function solutions *vs.* normalized rf amplitude for the n = 0, 1 and 2 steps, assuming $\nu >> \nu_c$ ($\Omega >> 1$), where I_{rf} is the rf current amplitude through the resistor, R, effectively ac voltage-biasing the junction.

regime, (4.2.1) can be solved analytically to find an expression for the widths of the constant-voltage Shapiro steps. In this regime the step widths are found to be identical to the ac voltage-biased step widths. It can be shown (see Van Duzer and Turner, 1981, p. 181) that the width of the steps, I_n, as a function of rf amplitude are found to behave like Bessel functions:

$$I_n = 2i_c J_n\left(\frac{2eV_{rf}}{h\nu}\right), \qquad (4.2.2)$$

where J_n is the Bessel function and V_{rf} is the amplitude of the voltage source. For the effectively ac voltage biased solution, V_{rf} can be replaced by $I_{rf}r_n$. When $\nu \leq \nu_c$, the step widths as a function of rf amplitude behave like distorted Bessel functions, as was shown through analog simulations by Russer (1972) and calculations by Taur *et al.* (1974).

We have found the rf frequency and amplitude dependence of our experimental step widths to be in excellent agreement with the distorted Bessel function behavior determined from the current-biased RSJ model. As an example, in Fig. 4.2(a) we have plotted the widths of the n = 0, 1, and 2 steps as a function of rf source amplitude for $\Omega = 1$ as determined from the measured i-v curves of our single junctions (including those shown in Fig. 4.1). These data are in excellent agreement with Russer's simulations for the same frequency. For this frequency, $\nu = \nu_c$, the behavior of the steps is very close to the exact Bessel function solution for the voltage-biased case, so for rough comparison, we have plotted (4.2.2) for the same steps in Fig. 4.2b. This comparison was experimentally useful because it gave us an estimate of the amount of rf current, I_{rf}, that was actually delivered to our samples through the measurement leads.

Since our single junctions follow the predicted theoretical behavior so well, we have great confidence that the junctions in the array are also behaving as ideal Josephson junctions. For instance, the junctions displayed *no* subharmonic steps, *i.e.* $V_n = (n/m)\, h\nu/2e$ having $m \geq 2$, which can be observed in underdamped junctions for various

frequencies and in overdamped point contacts or microbridges, where the current-phase (I-ϕ) relation may not be purely sinusoidal. This agrees with theory, since it has been proven (Renne and Polder, 1974) that the driven RSJ equation (4.2.1) without capacitance and with a purely sinusoidal I-ϕ relation, can not produce subharmonic steps.

4.3 Experimental Array Results

4.3.1 Giant Shapiro Steps

In this section we continue with a description of some of the experimental results on arrays when driven with rf currents. We consider first the effect of rf currents on the 2D array in *zero* magnetic field (f = 0). Fig. 4.3a shows a typical dV/dI *vs.* V curve for f = 0 at T = 3.0K, a temperature below the KT transition (T_{KT}~3.5K for this sample). The voltage axis has been normalized to Nhν/2e, so that 2eV/Nhν = n when the array is on the n'th giant step. The measured I-V is included as an inset (Fig. 4.3b). These data are representative, and clearly show minima in the dynamic resistance corresponding to *giant* steps at voltages in agreement with (4.1.1). This behavior indicates that the N = 1000 junctions in each row across the array are all on the same step and attempting to lock to the rf current.

In zero field, the 2D array can be thought of as behaving like a collection of single junctions, all simultaneously phase-locking to the drive frequency, and all having the same average (dc) voltage. These voltages simply add across the array, so that for an M by N array (see Section 3.3.1), the total array voltage is: V = Nv. The array bias currents, likewise, must scale with the width, M, of the array, so that the total array current is M times larger than the single junction currents, *i.e.* I = Mi. However, the characteristic frequency that determines the dynamics of the array is simply the characteristic frequency of the junctions, namely $\nu_c = 2ei_c(T)r_n/h$. Thus an array of junctions in zero field will have

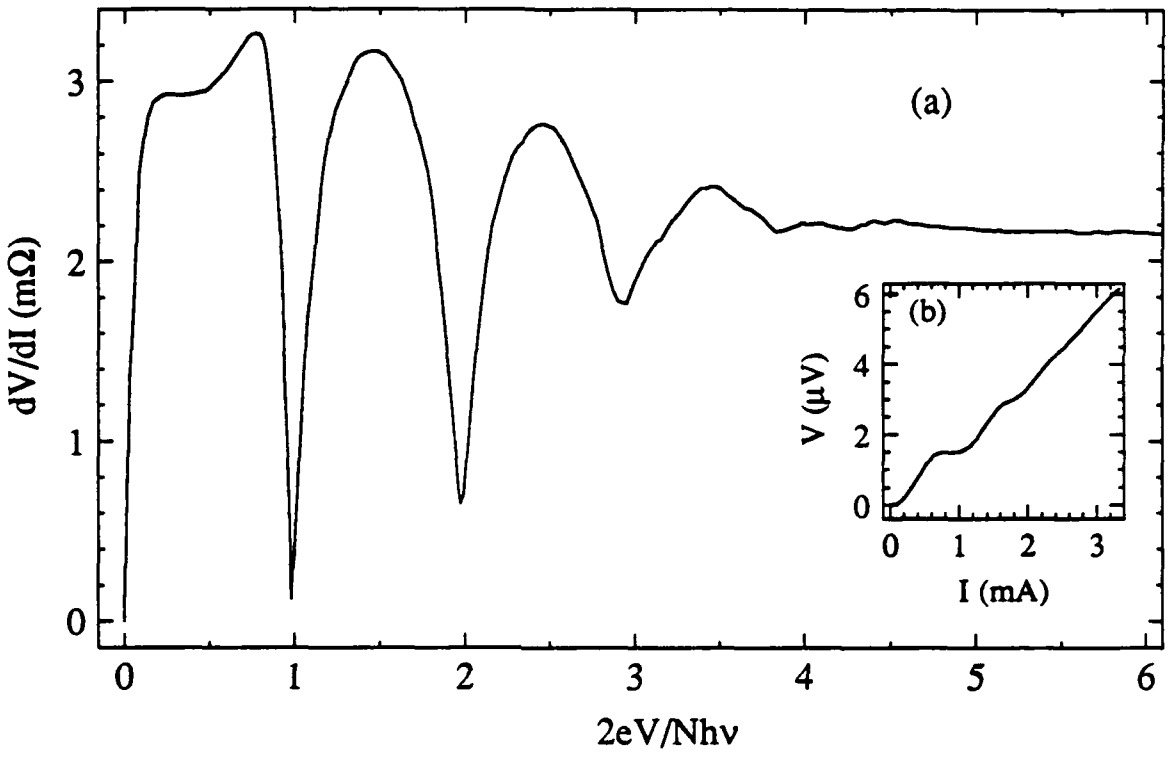

Fig. 4.3. (a) A typical dynamic resistance *vs.* normalized voltage curve in zero field for a 1000 by 1000 array. The data were taken at T = 3.0K, where I_c = 0.79mA, with ν = 0.73MHz ($\Omega = Nh\nu/2eI_cR = 1.0$), and $I_{rf} \sim I_c$. (b) The inset shows the I-V curve measured with the same parameters.

the same I-V curve as a single junction, for the same frequency, but the voltage and current axis will by scaled by N and M respectively. This is why we can measure steps in the arrays at much lower frequencies (kHz or MHz) than can typically be measured in single junctions (MHz or GHz).

When a magnetic field is applied to the array, however, the dynamics becomes dominated by the collective effects of the array. When f is an integer, we find that the array behaves as it did in zero field, showing giant Shapiro steps. This periodicity derives from the commensurability of the magnetic field with the periodic array structure, because for all integer f there are no field-induced vortices in the array. This periodicity is identical to the periodicity found for the magnetoresistance, critical current, and transition temperature, discussed in Section 1.4. This symmetry of the 2D array in a magnetic field is one of the primary characteristics that distinguishes the ac dynamics of arrays from that of single junctions or series arrays (as was also found for the dynamic resistance curves with dc currents in Chapter 3) and also leads to the novel appearance of fractional giant steps for commensurate fields discussed in the next section.

4.3.2 Fractional Giant Shapiro Steps

Fig. 4.4 shows the dynamic resistance *vs.* normalized voltage for *strongly commensurate* fields when f = 0, 1/2, and 1/3 at T = 2.1K, all for the same rf frequency and amplitude. The voltage axis has been normalized to Nhν/2e, so that 2eV/Nhν = n/q when the array is on the n'th fractional giant step. The minima in the dynamic resistance correspond to *fractional* giant Shapiro steps at voltages in agreement with (4.1.2). For example, when f = 1/3, steps are observed when 2eV/Nhν = 1/3, 2/3, 1, 4/3, etc. The step widths become narrower for larger q. We have also observed fractional giant steps for f = 1/6, 1/5, 1/4, 2/5, 2/3, and 3/4, confirming the q-dependence of the fractional steps. The

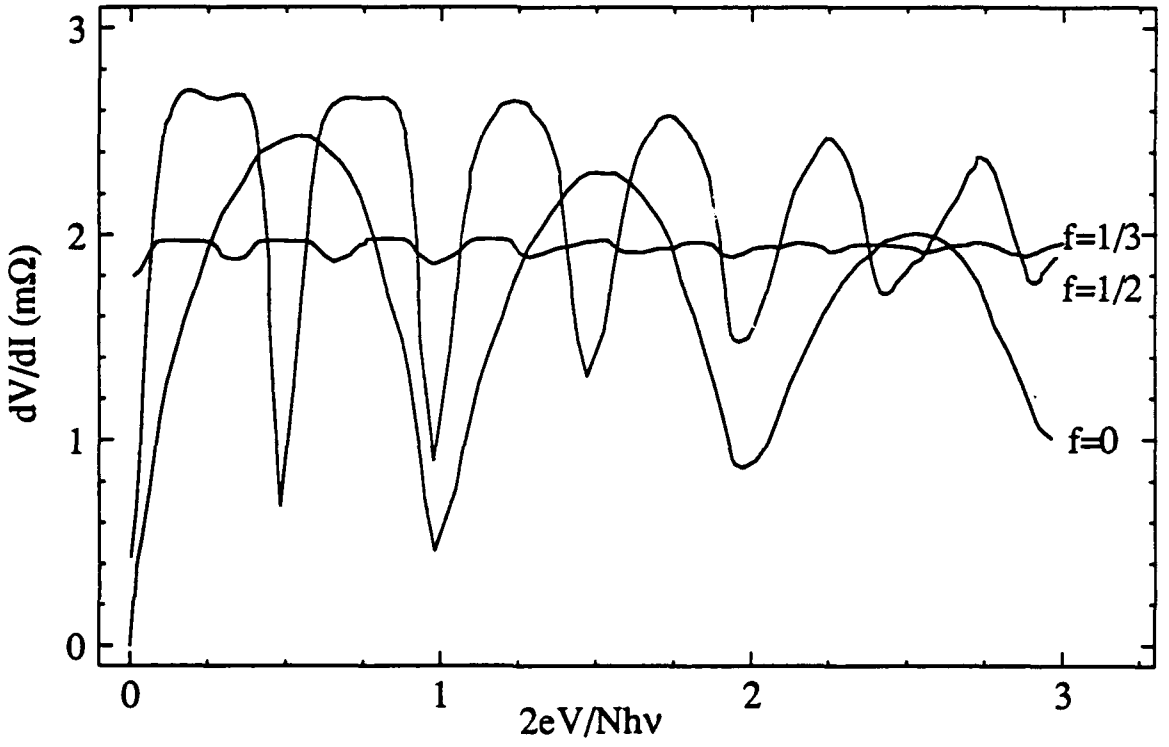

Fig. 4.4. Dynamic resistance *vs.* normalized voltage for different commensurate magnetic fields, corresponding to f = 0, 1/2, and 1/3. The data were taken at T = 2.1K, where I_c = 7.9mA, and with the same rf frequency, ν = 0.73MHz ($\Omega = Nh\nu/2eI_cR = 0.1$), and amplitude, $I_{rf} \sim 0.75I_c$, for each curve.

fractional steps found for f = 2/3 are at voltages identical to those for f = 1/3, thereby establishing the symmetry about f = 1/2 of the fractional giant steps.

4.4 Vortex Motion Model

The voltages of these novel field-induced fractional giant steps can be explained by a simple picture incorporating the motion of vortices arranged in superlattices with qxq unit cells on a periodic 2D "egg-carton" pinning potential due to the junction array. Vortex superlattices and the "egg-carton" potential are described in detail in Chapter 1, but will be briefly summarized below. The motion of a single vortex in a periodic junction array is analogous to the motion of a particle on a periodic 2D "egg-carton" pinning potential (Lobb *et al.*, 1983, and Rzchowski *et al.*, 1990). The minima of the egg-carton potential are located at the centers of the array unit cells. The potential has energy barriers at the junctions so that the vortices prefer to be centered on a unit cell and not over a junction (see Fig. 1.5). When a commensurate magnetic field is applied, the repulsive forces between the vortices combined with the influence of this 2D potential, cause them to be arranged in the ordered superlattices discussed above.

When a dc current is applied to the array, a Lorentz force is exerted on the vortices as discussed in Chapter 3. This force, in effect, tilts the 2D potential[4] so that for large enough currents the vortices will slide down the potential. Note that the Lorentz force will move vortices of opposite sign in the opposite direction, giving rise to the symmetry about f = 1/2 mentioned above, and that the dc current required to depin the vortex superlattice is different for the various commensurate fields, giving rise to the different depinning currents, $I_c(f)$, discussed in Chapter 3. Thus, for strongly commensurate fields, the vortex

[4]This is analogous to the 'washboard' model for single junctions, where the current term is included in the 'effective' potential (see Van Duzer and Turner, 1981, pp. 179-180).

superlattice can be considered to move down a tilted 2D potential in response to applied dc currents.

When an rf current is applied, the potential is effectively rocked at the rf frequency so that, at sufficiently high values of rf and dc current, the entire superlattice can slide down the potential, locking to the rf frequency. The array I-V curves will have fractional giant steps when this synchronized motion occurs because the junctions will collectively phase slip as the vortices in the superlattice move across them at periods of the drive frequency. We will first describe the model for the specific case of f = 1/3, and then include a detailed description for arbitrary magnetic fields.

In the zero temperature *ground state* for f = 1/3 (q = 3), the vortices are distributed in a 'staircase' superlattice (see Fig. 1.4b). At finite temperatures and in the presence of dc and rf bias currents, we assume, for simplicity, that the vortices are still arranged in 3x3 superlattice unit cells.[5] The currents exert a Lorentz force on the vortices, causing the ground state configuration to deform so that the vortices move across the array perpendicular to the direction of applied current. This superlattice motion is shown schematically in Fig. 4.5. When the entire f = 1/3 vortex superlattice has moved one array unit cell, indicated in Fig. 4.5 by the solid arrows, then a total phase slip of $2\pi N/3$ will have occurred across the array. When this happens exactly once every rf period, then the voltage is given by (4.1.2), with n = 1 and q = 3, giving the first fractional giant Shapiro step. If the dc current is increased so that the vortex superlattice moves across two array unit cells, a distance of $2a$ (indicated by the dashed arrows in Fig. 4.5), in an rf period, then a total phase slip of $4\pi N/3$ occurs giving the n = 2 fractional giant step for q = 3. Similarly, for n = 3, the f = 1/3 superlattice will move three array unit cells per rf period so

[5]The actual positions of the vortices within the superlattice unit cell is unimportant. The essential element for the model is that there exist a repeat distance, q, in the direction of vortex motion. In the presence of large enough bias currents, when the vortices are moving, the actual positions of the vortices in the unit cell may be different from the ground state, but the model still gives the correct step voltages.

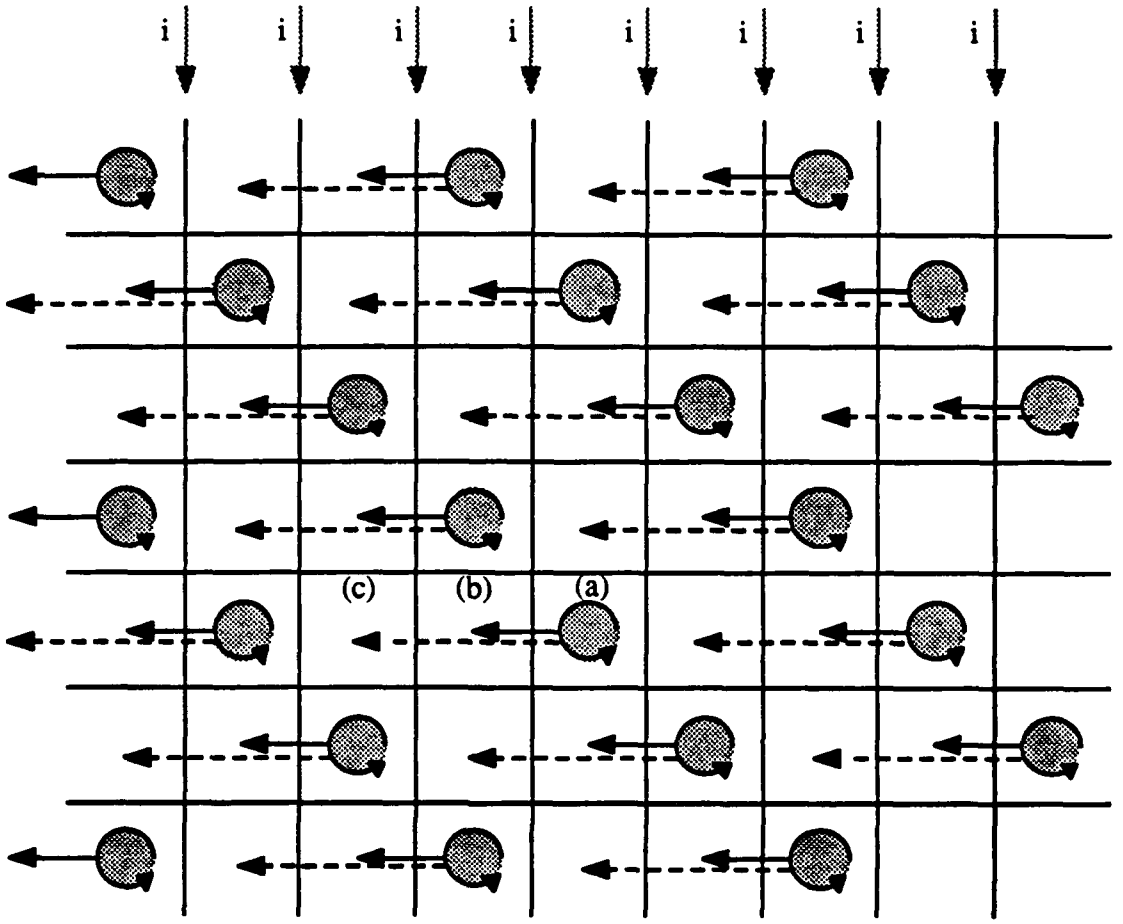

Fig. 4.5. Array schematic showing vortex motion model for f = 1/3. The position of the vortices is indicated by the filled circles. The applied magnetic field direction is out of the page so that the circulating vortex currents are counter-clockwise (as indicated). The dc and rf bias currents are distributed uniformly from top to bottom as in indicated by the shaded arrows labelled 'i'. The Lorentz force on the vortices due to these currents will move them to the left. When the superlattice moves one array unit cell (as shown for a vortex in the middle moving from (a) to (b) along the solid arrow) in each rf cycle, the array will be on the n = 1, q = 3 fractional giant step. When the superlattice moves two array unit cells (dashed arrows), as indicated for one vortex moving from (a) to (c), in each rf period, then the array will be on the n = 2, q = 3 fractional giant step.

that the vortices are at the same position in the array after every rf period. This will give the same voltage as the n = 1 giant step in zero field because all the junctions in the array are phase slipping by 2π per rf period.

In general for f = p/q, the vortices lie in qxq superlattice cells, so that the ratio of the number of array unit cells moved per rf period, n, relative to the vortex superlattice unit cell size, q, determines the voltage at each step. When the entire superlattice moves one array unit cell during one rf period, the total phase slip across the array will be $2\pi N/q$, giving a total voltage across the array of (N/q) hν/2e, corresponding to the first fractional step for that particular commensurate field (given by (4.1.2) with n = 1). The n'th fractional step occurs when the superlattice moves n array unit cells in a given rf period, giving a total phase slip of $2\pi nN/q$ across the array. Thus, when the number of array unit cells moved is not a multiple of the vortex superlattice cell size, then n/q is a fraction and the voltage across the array will be a *fractional* giant step. It is the commensurability of the vortex superlattice with the periodic pinning potential of the array of junctions that is essential for producing the fractional giant steps. When n/q is an integer, the vortex superlattice returns to a configuration which is identical to its starting configuration after each rf period. In this latter case, the Josephson frequency $\nu_J = 2eV/Nh$ of each junction is a harmonic of the drive frequency, that is $\nu_J/\nu = n/q$ is an integer, and all the junctions phase slip by $2\pi n/q$ per rf period. These 'harmonic' giant steps occur at the same voltage as the giant steps in zero field.

Our model for the fractional steps does not attempt to describe the detailed motion of the vortices, but only to present a qualitative picture that would result in a total phase slip across the array of $2\pi nN/q$ per rf drive period and thus give the experimentally discovered voltages. Dynamical simulations on arrays of resistively shunted junctions are required to determine the vortex motion in more detail and will be discussed in Chapter 5.

4.5 Discussion

In this section we will discuss some of the experimental details of the fractional giant steps. We will also attempt to explain certain experimentally observed features, such as the roundedness of the steps, and 'subharmonic' steps in zero field. An experimentally observed 'beating' effect of the dynamic resistance for large drive currents will also be shown. We will begin with a detailed discussion of the frequency dependence of the ac properties of arrays.

As discussed in Section 4.3.1, the frequency dependence of the giant Shapiro steps for integer f is primarily determined by the characteristics of the single junctions in the array. These junctions, with critical currents $i_c(T)$, are highly overdamped, having an essentially infinite plasma resonance frequency, so that the relevant frequency is the crossover frequency, $\nu_c = 2ei_c(T)r_n/h$, above which the normal state resistance of the junction, r_n, dominates the conduction, as discussed in Section 4.2. The rf frequency and amplitude dependence of the experimental giant step widths of the array in zero field qualitatively follow the behavior of the single junctions for the same reduced drive frequency $\Omega = \nu/\nu_c$, if we use the critical current of a single junction in the array, $i_c(T) = I_c(T)/M$, with the experimentally determined array critical current, $I_c(T)$, in the definition of ν_c. Since i_c is strongly temperature dependent (2.3.1), ν_c is also, so that we can explore a wide range of frequencies. (Note the different values of Ω for the different $I_c(T)$ in Figs. 4.3 and 4.4). Despite the rounding effects, we have observed giant steps in our 2D arrays in the frequency range 90kHz-50MHz, and up to 1GHz in a 1000 junction *series* array. The observation of the giant steps in the 2D arrays (for $\nu \sim \nu_c \propto i_c(T)$) at low temperatures when the characteristic frequency is large, appears to be limited only by the larger drive currents necessary to achieve sizeable steps, due to the exponential temperature dependence of $i_c(T)$ and $I_{rf} = Mi_{rf}$ (see Section 2.3). The sample size (1cm x 1cm) is much smaller than the shortest wavelength, λ, of applied rf radiation (for 1GHz), so that the

finite sample size does not limit the frequency range over which the junctions can be coherently driven, and the array can be treated as a lumped element (Na, and $Ma << \lambda$).

The dependence of the width of the commensurate field-induced *fractional* steps on rf frequency and amplitude is still under investigation, but some interesting qualitative features have been observed. The frequency dependence of the step widths, in general, qualitatively follows the behavior for single overdamped junctions, in that they get smaller as Ω gets smaller. The field-dependent critical currents, $I_c(f)$, for the commensurate vortex superlattices, also appear to influence the absolute step width for these states; experimentally (see Chapter 3) we find that $I_c(f=1/2) > I_c(f=1/3)$ and that the giant step widths for $f = 1/2$ are greater than those for $f = 1/3$. We propose that the fractional step widths may scale with $I_c(f)$, and that the characteristic frequency describing the response of the array in the presence of a commensurate field is scaled by $I_c(f)$ instead of $I_c(f=0)$. A detailed study of the experimental step widths as a function of rf frequency and amplitude is complicated by the roundedness of the steps and the fact that they are not absolutely flat.

The roundedness and lack of flatness of the fractional giant Shapiro steps indicates that voltage locking of the single junctions is incomplete throughout the entire array. The Shapiro steps in our single junctions do appear flat at the lowest attainable temperatures (1.35K), indicating that the junctions are then truly phase-locked to the rf current. The giant steps of the array could not be quantitatively compared with those of the single junctions, because the giant steps are more rounded and dV/dI does not always go completely to zero at each step. The giant steps in the arrays become flatter at lower temperatures, but the steps are not completely flat even at the lowest measurable temperature (2.1K). (The single junctions cannot be measured at the same temperature and characteristic frequency as the arrays because the single junction steps are completely washed out by thermal fluctuations at 2.1K (see Section 1.3). The arrays cannot be measured effectively below 2.1K, as discussed in Section 2.3, because the available I_{rf} is insufficient to induce observable steps as a result of the larger critical currents at lower

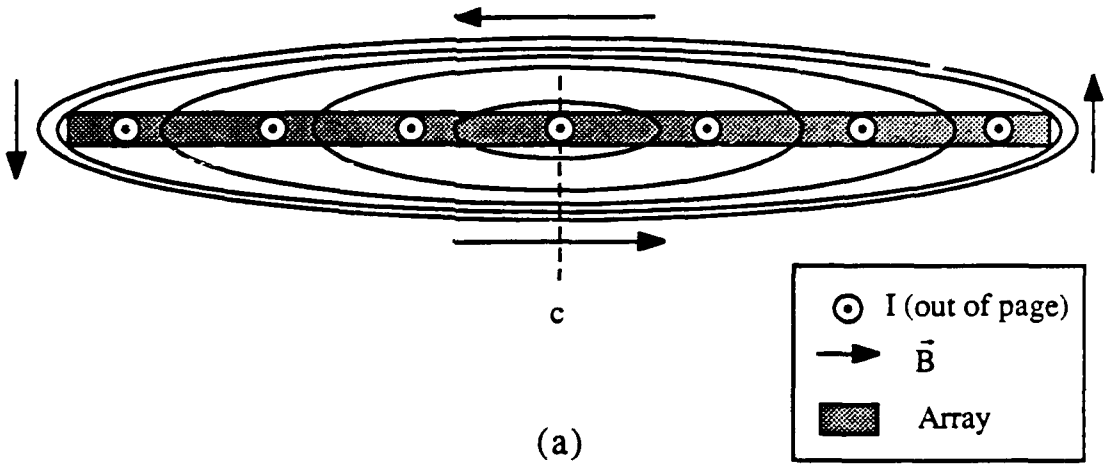

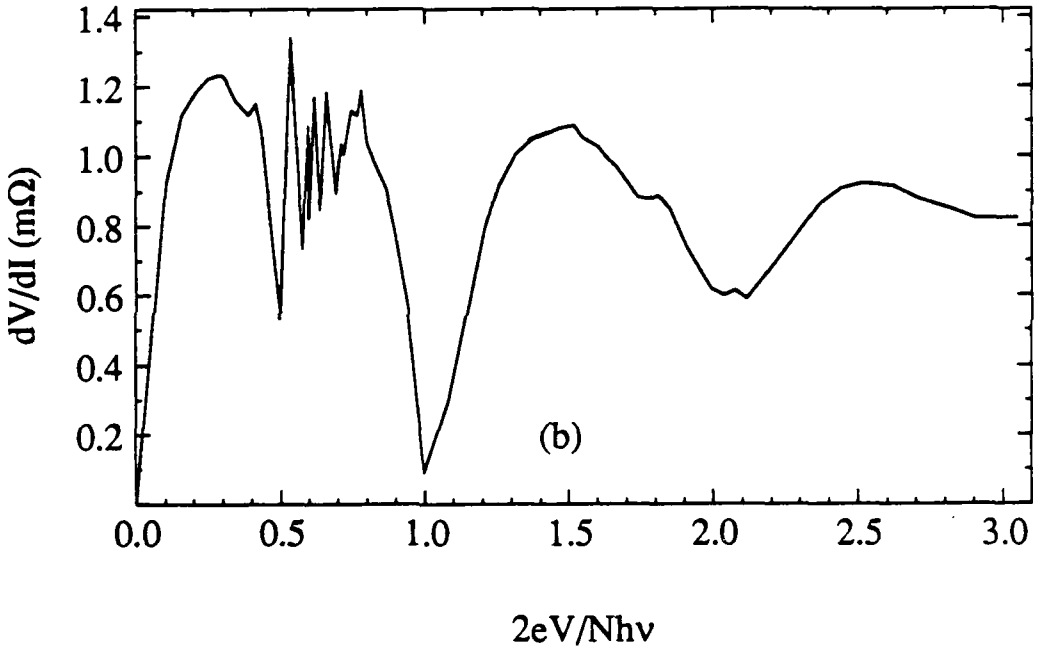

Fig. 4.6. (a) Cross section of an array perpendicular to the applied current direction. A current-induced magnetic field, indicated by the ellipsoidal lines (and direction indicated by the arrows: counterclockwise for applied current out of the page) penetrate the array, being strongest near the edges. This field will induce vortices in the array, with opposite sign on the left side from those on the right. These 'current-induced' vortices will be forced towards the center of the array (point 'c') by the current, where they will annihilate with vortices of the opposite sign. The dissipation from these extra vortices may cause rounding in the I-V curves or of the fractional steps. They also may be responsible for the 'subharmonic' steps in zero field. (b) Dynamic resistance *vs.* normalized voltage in zero field (f = 0), for T = 2.09K, ν = 7MHz ($\Omega \approx 1.0$), V_{rf} = 500mV ($I_{rf} \sim I_c$). Subharmonic structure is apparent between the n = 0 and n = 1 giant steps.

temperatures.) This experimental evidence suggests that the rounded giant steps in the 2D array are primarily a result of thermally-induced vortices and thermally-activated phase slip. This view is consistent with theory, since the ratio of the energy barrier to the temperature, central to the Ambegaokar-Halperin (1969) theory for noise rounding due to thermally activated phase slip, is ~85 times larger for one of our junctions at 1.35K than at 2.1K. Non-uniform current flow due to the sample size being larger than the perpendicular penetration depth (see Section 2.3), or due to differences in single junction critical currents throughout the array, may also contribute to rounding.

Even with the symmetric current injection leads (Fig. 2.6b) that were used for these measurements, the large bias currents can still generate magnetic fields in the array. These fields will, however, be antisymmetric about an imaginary center line drawn parallel to the applied current through the array. The finite size of the array will cause these fields to be strongest near the edges of the array, as shown in Fig. 4.6a, generating vortices of opposite sign on opposite edges. These vortices, which are present in zero field, will be driven by the current toward the center of the array, where they can annihilate with the oppositely-signed vortices that are moving toward the center from the opposite side. These 'current-induced' vortices may also contribute to the rounding of the steps discussed above, but we believe they are responsible for a more interesting effect: 'subharmonic' steps observed in zero field. An example of these steps that shows a considerable amount of structure is shown in Fig. 4.6b. The 'subharmonic' steps that we have observed are the most prominent when $\Omega \geq 1$ and $I_{rf} \geq I_c$, and generally have a only single feature occuring at $2eV/Nh\nu = 1/2$, where $n = 1$, and $m = 2$ (see Section 4.2). Motion of current-induced vortices can lead to a subharmonic giant step at $n/m = 1/2$ if the current generates a field strong enough to nucleate a vortex in every other cell on the edges of the array during each rf period. These vortices will move towards the center (moving one array unit cell in each rf period) in an $f = 1/2$-like superlattice where they will annihilate with the oppositely signed vortices arriving from the opposite edge. This current-induced vortex model, which

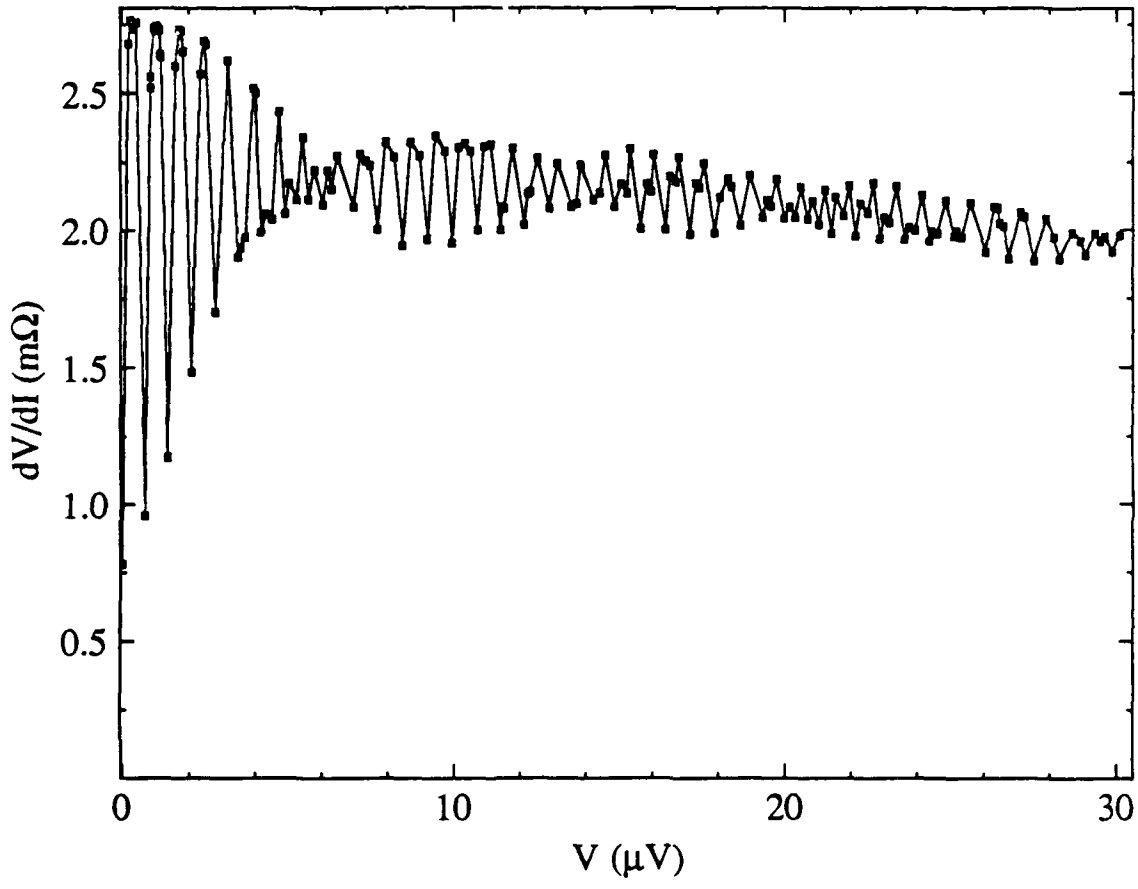

Fig. 4.7. Dynamic resistance *vs.* voltage for a 1000x1000 array, with f = 1/2, showing a 'beating effect'. The data were taken at T = 2.09K, where I_c = 7.9mA, with ν = 0.73MHz ($\Omega \approx 0.1$), and amplitude, $I_{rf} \sim I_c$.

originated through discussions between S. P. Benz, J. C. Garland, C. J. Lobb, D. B. Mast, R. S. Newrock, and M. Octavio (1990 APS March meeting), although speculative, has some experimental support. In a recent experiment by Mast and Newrock (Lobb, 1990), the 'subharmonic' steps disappeared when currents were injected in the opposite direction through a parallel normal-metal film placed directly above the array (thus eliminating the perpendicular component of the field and the 'current-induced' vortices in the array).

Another interesting feature that we found experimentally was a 'beating effect' in the dynamic resistance, shown in Fig. 4.7, where the minima and maxima in the dynamic resistance at the steps have a complicated (almost Bessel function-like) dependence on the dc voltage. This phenomena has been observed for a number of commensurate fields, including f = 1/2 and f = 1/3, but only occurs for large rf drive amplitudes, $I_{rf} \geq I_c$. The minima and maxima in the dynamic resistance appear to oscillate over finite voltage intervals. Possible causes for this phenomena may include a combination of the following: non-uniformity in the junctions, finite array size and current-induced vortices, or a more complicated superlattice motion for these large rf bias currents. This phenomena requires further examination to determine its dependence on rf frequency and amplitude.

4.6 Conclusion

In this chapter we presented some interesting phase-locking properties that were experimentally discovered in 2D arrays. In the presence of rf currents and commensurate magnetic fields, novel steps appeared in the dc I-V characteristics which were named 'fractional giant Shapiro steps' because they occurred at fractions of the voltage found for the array in zero field. We have explained these steps with a model of vortex motion, where vortices move collectively across the array locking to the rf drive frequency. In the next chapter we present the results of computer simulations that were used to further explore the ac dynamical properties of junction arrays.

CHAPTER 5

AC PROPERTIES: DYNAMICAL SIMULATIONS

5.1 Introduction

The experimental measurements presented in Chapter 4 have shown that when a radio-frequency (rf) current, $i_{rf}\sin(2\pi\nu t)$, is applied to a square array of Josephson junctions in the presence of a perpendicular magnetic field commensurate with the lattice structure of the array, *fractional* giant Shapiro steps occur in the dc I-V characteristics at voltages

$$\langle V_n \rangle = n\left(\frac{N}{q}\right)\frac{h\nu}{2e}, \qquad n = 0,\ 1,\ 2,..., \tag{5.1.1}$$

where $\langle V_n \rangle$ is the average voltage across the array, n is an integer, N is the number of junctions in the array in the direction of the applied current, and q is determined by the vortex superlattice unit cell size q x q. The vortex superlattice, in turn, is determined by the number of flux quanta per array unit cell, f = p/q, where p and q are integers. Such a rational value of f is essential for observing fractional giant Shapiro steps because only for such fields are field-induced vortices arranged in ordered superlattices commensurate with the array of junctions.

We proposed in Section 4.4 that these fractional steps arise from the motion of a field-induced vortex superlattice as it moves across the array in response to the rf and dc currents. In this model, locking of the rf frequency and the frequency of the superlattice motion results in Shapiro-like steps in the I-V curves. Since the detailed motion of the

vortices in response to the rf current is difficult to determine experimentally, we have performed simulations[1] on 2D arrays of overdamped resistively shunted junctions (RSJ) to gain insight into the physical origin of the fractional giant steps. The simulations show fractional giant steps in agreement with (5.1.1), and confirm the phenomenological model proposed in Section 4.4 to explain the steps. We will describe these results and then present further results of simulations, at frequencies lower than the characteristic frequency of the junctions, $\nu_c = 2ei_cr_n/h$, that show unexpected dynamical behavior.

5.2 Simulation Algorithm

Our numerical simulations were performed, as were previous simulations (Xia and Leath, 1989 and Chung *et al.*, 1989), by solving the coupled, nonlinear, first-order differential equations found from current conservation at each node of the array. In the RSJ model, discussed in Chapter 1, it was shown that the current, i_{ij}, through an individual junction is given by

$$i_{ij} = i_c \sin\gamma_{ij} + \frac{v_{ij}}{r_n}, \tag{5.2.1}$$

where r_n is the junction resistance, the voltage drop across the junction is given by the Josephson relation,

$$v_{ij} = \frac{\hbar}{2e}\frac{d\gamma_{ij}}{dt}, \tag{5.2.2}$$

and the total gauge invariant phase difference across the junction is given by

[1]Most of the results presented in this chapter have been published in Free *et al.*, 1990 and in Benz *et al.*, 1990c.

$$\gamma_{ij} = \phi_j - \phi_i - \frac{2\pi}{\Phi_0}\int_i^j \vec{A}\cdot d\vec{l}\,, \qquad (5.2.3)$$

where Φ_0 is the flux quantum, ϕ_i is the phase on node i, and $\vec{A}$ is the vector potential. The magnetic field, $\vec{H} = H\hat{z}$, enters through the vector potential. We use the Landau gauge $\vec{A} = Hx\hat{y}$ so that the integral term vanishes for junctions along the $\hat{x}$-direction and equals $(2\pi H/\Phi_0)x(y_j-y_i) = \pm 2\pi f\,(x/a)$ along the $\hat{y}$-direction, where y_i and y_j are coordinates of the i'th and j'th nodes. Current conservation at each node requires,

$$\sum_j i_{ij} = i_i^{ext}\,. \qquad (5.2.4)$$

In general $i_i^{ext} = 0$, except at the boundaries, where $i_i^{ext} = \pm[i_{dc} + i_{rf}\sin(2\pi\nu t)]$ is the current injected (+) or extracted (-), as in the experimental configuration. Periodic boundary conditions were chosen in the direction perpendicular to the current. The applied dc and rf currents were uniformly injected into each column of the array. This is shown in the schematic circuit diagram for a simulated 4x5 junction array in Fig. 5.1.

The coupled first-order differential equations resulting from (5.2.1)-(5.2.4) were solved using a fourth-order Runge-Kutta method with uniform time steps. Starting with initial phases at each node, the equations were integrated forward one time step to generate new phases, which were then used to integrate forward another time step, etc. The times steps were generally chosen to be one-fiftieth of the characteristic period, $1/\nu_c$. I-V curves were calculated by ramping the current from zero, where the phases were placed initially in the zero-temperature ground state configuration (see Figs. 1.3a and 1.3b), in order to avoid boundary-related metastable states due to finite array size. The phases were allowed to relax over 200 rf periods before time-averaging the voltage to obtain the average voltage <V>. The longest periods in the simulations occur near the edges of the steps, but generally 200 rf periods were sufficient for achieving a good average. The time steps were

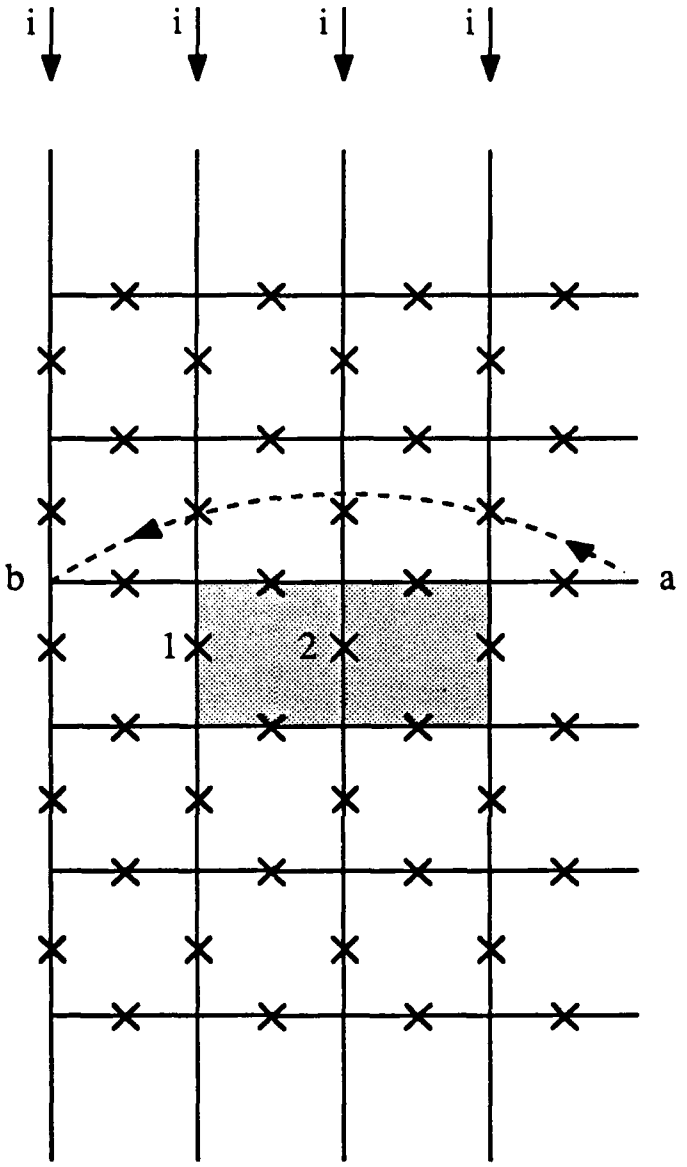

Fig. 5.1. Schematic circuit diagram for a simulated 4x5 junction array with periodic boundaries in the direction perpendicular to the applied current. The bias current, $i = i_{dc} + i_{rf}\sin(2\pi\nu t)$, is injected at the top and removed at the bottom, and distributed uniformly to each of the junctions along the edges, as shown by the solid arrows. The dangling junctions on the right side are connected to the vertices on the left in order to complete the periodic boundaries, as indicated for one of the junctions by the dashed curve with arrows from 'a' to 'b'. The voltage waveforms on the first $f = 1/2$ fractional giant step for the two junctions labelled 1 and 2 are displayed in Fig. 5.3, and the junction currents on this step at three specific times are shown in Fig. 5.4 for the two shaded unit cells in the center.

chosen to be small fractions of the characteristic period ($1/50\nu_c$) and the relaxation and averaging times were taken as a large multiple of the rf period ($200/\nu$), because $1/\nu_c$ is the smallest fixed period in the problem and$1/\nu$ was generally the largest for the frequency range studied, $\nu \leq \nu_c$.

The choice of boundary conditions for the simulations was not arbitrary. Simulations had to be done on small arrays, since it was not computationally feasible (on our Apollo computer) to simulate the 1000 by 1000 arrays used in our experiments. Periodic boundary conditions (see Fig. 5.1) were chosen in the direction perpendicular to the current, rather than free boundaries, because free boundaries cause non-uniform vortex motion in small samples. The number of junctions in the periodic direction must be a multiple of q in order to accommodate a qxq vortex superlattice, and to match the symmetry with the lattice.

A more critical boundary problem that influenced the dynamics of the simulated arrays was the method of current injection. We originally used bus bars in our simulations by tying the junctions on both ends to single nodes (each with a single phase), and injecting and extracting the current from these nodes. However, bus bars were found to strongly affect the simulated I-V curves because of the nonphysical phase constraints they introduce, leading, for example, to unreasonably small critical currents. Fractional giant steps were also observed in the simulations with bus bars and either periodic boundary conditions or free boundary conditions, but we found that uniform current injection and periodic boundary conditions in small arrays more closely simulated the behavior of our large experimental arrays. We note that the *dynamical* behavior on the steps was not significantly affected by boundary conditions, even though the *values* of the dc currents at which steps occur, *i.e.* the step widths, were affected.

With periodic boundary conditions perpendicular to the current and uniform current injection imposed at the ends of the array, the critical current per junction for the f = 1/2 state was found to be $i_c(f=1/2) = 0.35 i_c(f=0)$. This is in agreement with the critical current

found by Mon and Teitel (1989) for the same boundary conditions. It should be noted that this critical current is substantially lower than that calculated (for infinite arrays) by other methods, as discussed in Chapter 3 where it was found that $i_c(f=1/2) = 0.414 i_c(f=0)$. This difference is due to the boundary conditions: uniform current injection gives a pattern of currents that strongly deviates from the periodic ground state near the current injection (or extraction) nodes. As an alternative to uniform current injection, we used currents at the boundaries which were determined from the exact calculations for the periodic f = 1/2 state, *i.e.* the supercurrent equations (3.6.5a)-(3.6.5c) for the α and γ junctions from the exact calculation in Section 3.6. With periodic boundaries perpendicular to the current and this current injection method, the array behaved as though it were part of an infinite array; the supercurrents in the array were not distorted near the current injection nodes, and the correct ground state critical current ($\sqrt{2}$-1) was reproduced.

The experimental arrays discussed in Chapter 3 were very large, 1000 by 1000 junctions, had free boundaries on the edges parallel to the current and used superconducting bus bars to inject the current (Fig. 2.4a). The arrays discussed in Chapter 4 used normal metal electrodes configured to inject the current approximately uniformly (Fig. 2.4b) were found to display essentially the same dynamic resistance behavior as the arrays with bus bars. We conclude that the experimental arrays are so large that their measured properties are essentially independent of their boundary conditions including the method of current injection, since the few affected rows of junctions at the edge of the array contribute a voltage that is less than one percent of that given by a feature involving the bulk of the array. Accordingly, their measured properties resemble those of an infinite array. On the other hand, since simulations are limited to much smaller arrays, the boundary conditions are more important, as discussed above. We were unable to use the exact solutions for currents greater than the critical current, so the uniform current injection technique was used as the best approximation for the large experimental arrays, even

though the critical current that is found experimentally for the f = 1/2 state agrees more closely with $0.414i_c(f=0)$, than the uniform current injection result of $0.35i_c(f=0)$.[2]

5.3 Voltage vs. Current Curves and Results

Figure 5.2 shows representative dc current-voltage (I-V) curves computed for various commensurate magnetic fields f with an applied rf current. The first curve shows results for f = 0 and $i_{rf} = i_c(f=0)$, at a normalized frequency $\Omega = \nu/\nu_c = 1$, where $\nu_c = 2ei_cr_n/h$ is the characteristic frequency. i_{dc} is the applied dc current per junction parallel to the current flow, and <V> is the time-averaged voltage across the array. The constant-voltage giant Shapiro steps occur at the voltages given by (5.1.1) with q = 1. This curve is the same as the response of a single junction to combined dc and rf currents because each junction responds in the same way to the external dc and rf currents, as was suggested in Chapter 4 for the zero magnetic field case.

The second curve in Fig. 5.2 shows an I-V curve for f = 1/2, with the same rf current amplitude and frequency as the f = 0 curve. Fractional giant Shapiro steps now appear at voltages given by (5.1.1), with q = 2. The third curve shows an I-V curve for f = 1/3. The voltages of the fractional giant Shapiro steps are also given by (5.1.1), with q = 3 in this case. All of these simulations produce results which are in qualitative agreement with the experiments discussed in Chapter 4.

---

[2]We have recently become aware of a new simulation technique (Eikmans and van Himbergen, 1990) that may allow periodic boundaries in both directions in the presence of arbitrary dc and rf bias currents This would provide the best method for eliminating finite-size and boundary effects in the small simulated arrays.

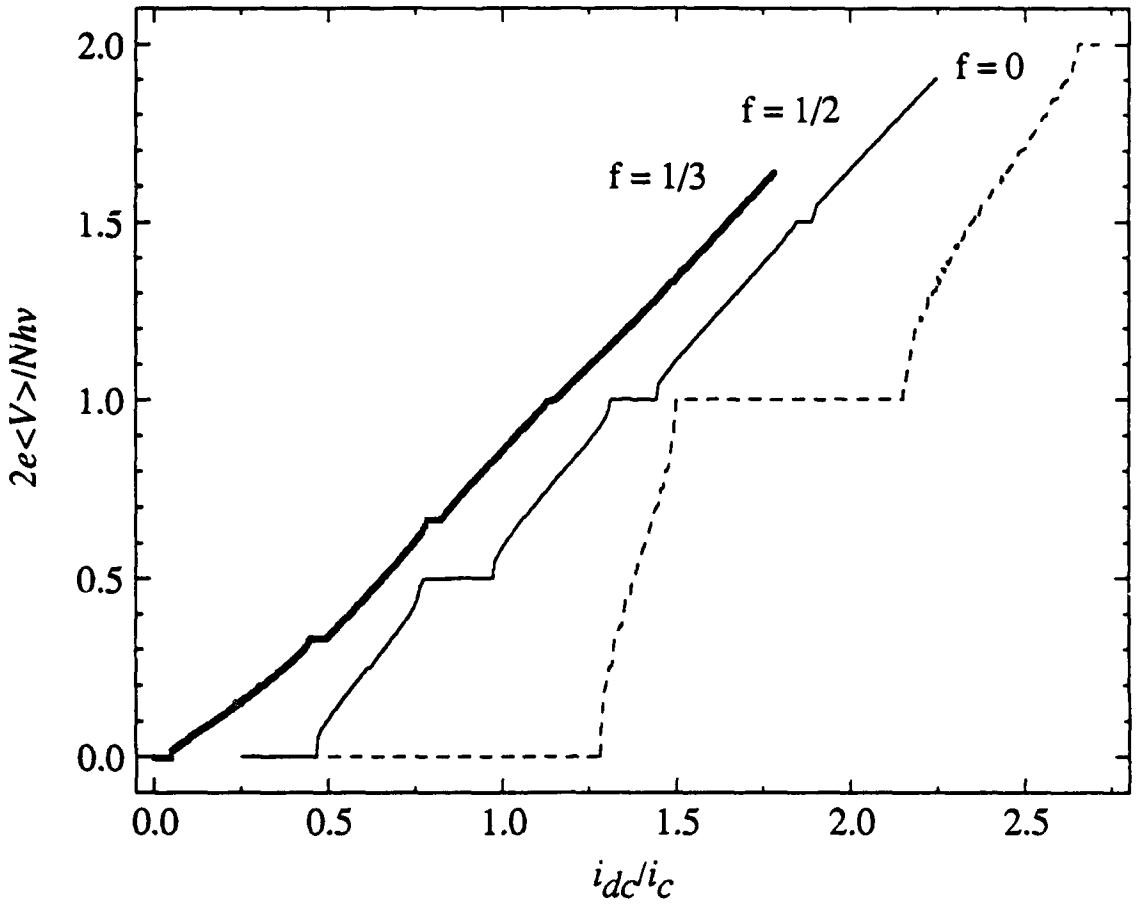

Fig. 5.2. Normalized time-averaged voltage vs. normalized dc current per junction for simulated MxN arrays with $\Omega = 1$, $i_{rf} = i_c$, and different magnetic fields: f = 0, 4x5 junctions; f = 1/2, 4x5 junctions; f = 1/3, 3x6 junctions. Curves f = 1/2 and f = 0 are shifted from the origin along the current axis by successive 0.25 increments. Fractional giant steps are apparent in these I-V curves and are at voltages in agreement with experimental results.

5.4 Comparison with the Vortex Motion Model

To gain further insight into the rf response of arrays, and to make a detailed comparison with the theoretical model discussed in Section 4.4, we have looked at the instantaneous voltage and phase difference across individual junctions in the array as a function of time. A 4x5 junction array (shown in Fig. 5.1) was chosen for f = 1/2 so that one row of junctions would be symmetrically located between the current injection and removal edges of the array. Fig. 5.3 shows the voltages across two adjacent junctions (labelled 1 and 2 in Fig. 5.1) in this row oriented along the current direction on the lowest (n = 1) fractional step of the f = 1/2 curve shown in Fig. 5.2. Two main features are worth noting. First, the two junctions have the same voltage waveform, but are out of phase by exactly one rf period. Second, the period of the voltage on *each* junction on this lowest step is twice the period of the external rf current, although the *spatial average* voltage retains the period of the drive.

Figure 5.4 shows the phases and supercurrents in two adjacent unit cells in the center of the 4x5 junction array (shaded unit cells in Fig. 5.1) at the times (a), (b), (c) indicated in Fig. 5.3, *i.e.*, before, during, and after the phase slips which dominate the behavior of the array on the lowest-voltage step. [The dc current flows from top to bottom in this figure. The instantaneous voltage of the center junction (labeled 2 in Fig. 5.4) is plotted by the solid line and the junction to the left (labeled 1) is plotted by a dashed line in Fig. 5.3] Fig. 5.4a shows the junctions at a point in the drive period when the rf and dc currents nearly cancel, and the phase and current configuration resembles the zero-current ground state. In Fig. 5.4b, the current in the center junction (labeled 2 in Fig. 5.3) has increased toward the zero-field critical current, while the currents of opposite sense in the adjacent junctions (labeled 1 and 3) have decreased nearly to zero. The phases continue to evolve until the currents in the outer junctions (1 and 3) go to zero and begin to increase in magnitude in the opposite direction, after which the current in the center junction (2) goes

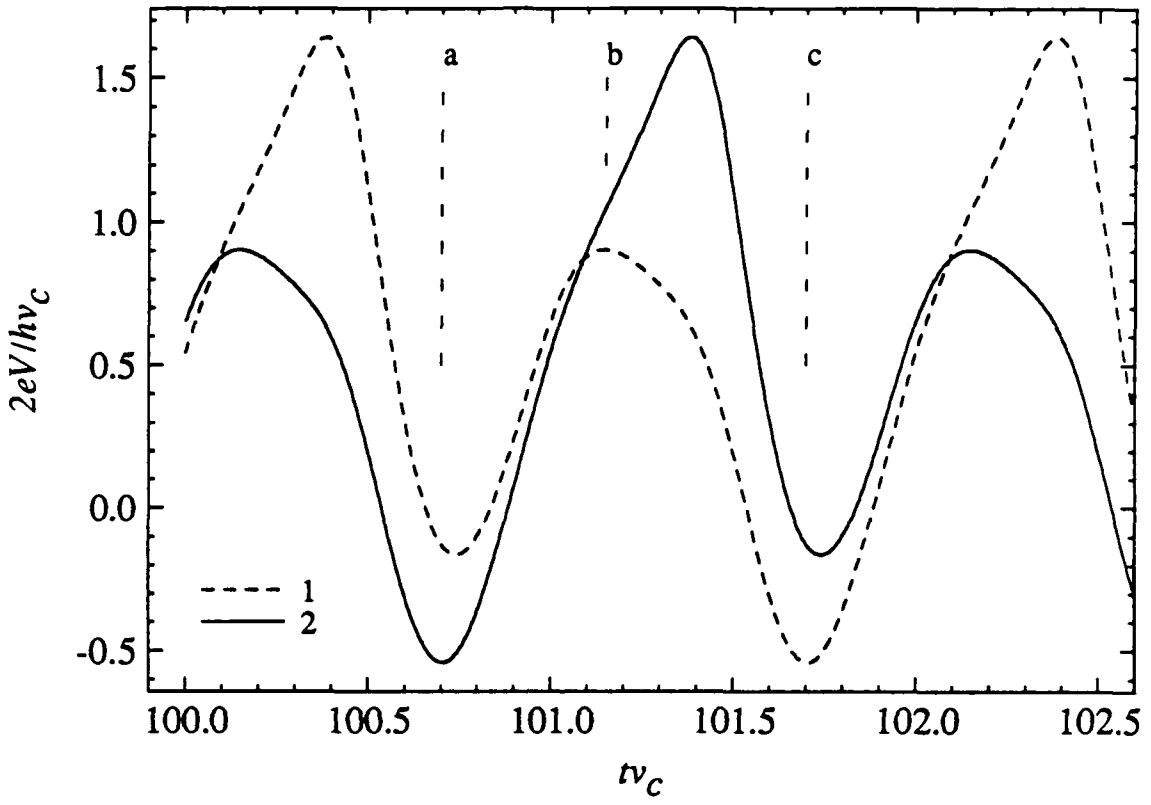

Fig. 5.3. Normalized instantaneous voltage *vs.* normalized time across two adjacent junctions parallel to the current (labeled 1 and 2 in Fig. 5.1) for a 4x5 array on the n = 1, q = 2 fractional giant step, with f = 1/2, Ω = 1, $i_{rf} = i_c$, and $i_{dc}/i_c = 0.65$. Lines a, b, and c mark the times associated with the supercurrent snapshots shown in Fig. 5.4. Time is normalized to the single junction characteristic frequency, ν_c. Note that the waveforms are identical, have a period double that of the rf period, and are out of phase by exactly one rf period.

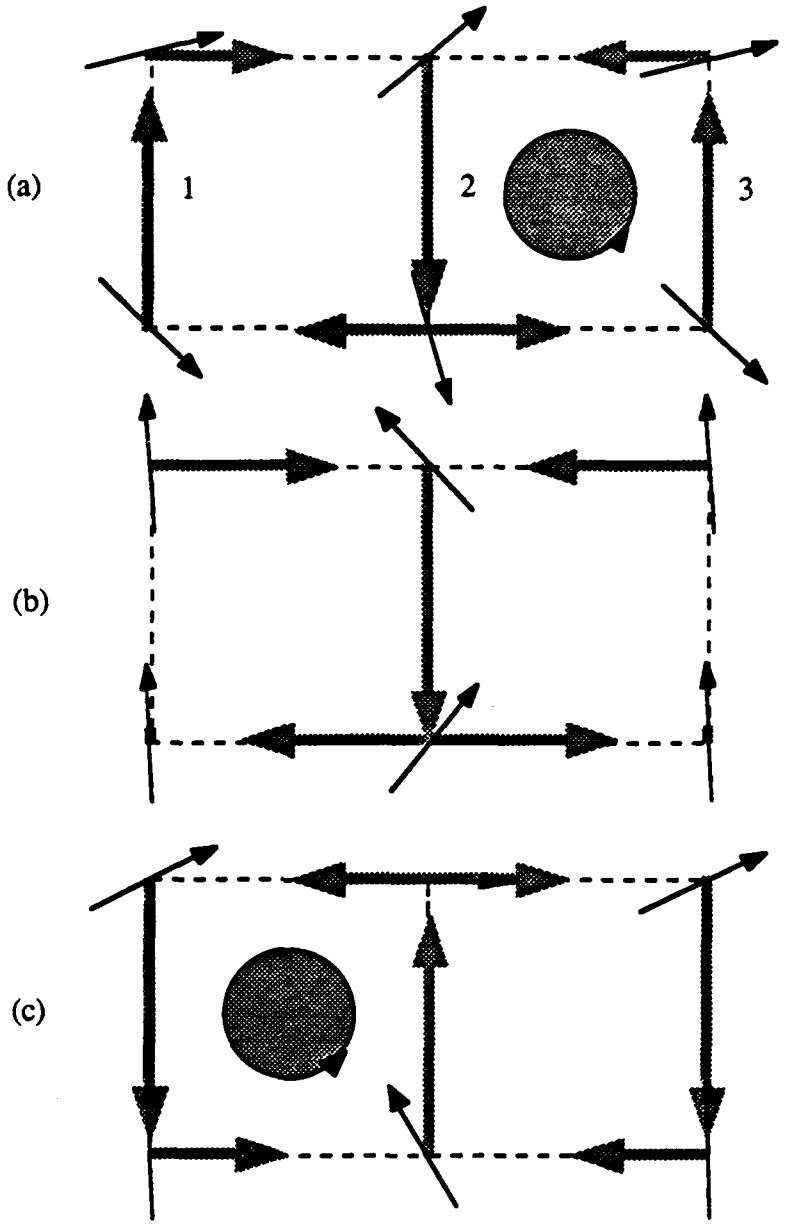

Fig. 5.4. Supercurrents (shaded arrows) and phases (narrow dark arrows) for two unit cells in the center of a 4x5 junction array (the shaded cells in Fig. 5.1) under the same conditions as in Fig. 5.3. a) $tv_c = 100.7$, b) $tv_c = 101.15$, and c) $tv_c = 101.7$. Times a) and c) are exactly one rf period apart (since $v = v_c$) and show the currents in the left unit cell at time (c) to be identical to the currents in the right unit cell exactly one rf period earlier at time (a). The filled circle with an arrow represents a vortex, centered on the right unit cell at time (a), moving across the energy barrier at junction 2 at time (b), and then sitting at the identical position in the left unit cell exactly one rf period later at time (c).

through zero and changes direction. Finally, the currents in the transverse junctions also reverse, so that unit cells which started with clockwise (counterclockwise) currents in Fig. 5.4a end up with counterclockwise (clockwise) currents in Fig. 5.4c. In effect, the f = 1/2 vortex superlattice has moved one unit cell, as indicated by the placement of the filled circle having moved from the right cell in Fig. 5.4a into the left cell in Fig. 5.4c. The phase difference across each junction in the direction of the current has advanced by an average amount of π, which leads, via the Josephson voltage-frequency relation, to (5.1.1) for the voltage drop across the whole array, with n = 1 and q = 2. More generally, when each junction has an average phase slip of $n\pi$ per rf period, the n'th step occurs. These results give detailed confirmation to the model proposed in Section 4.4.

Analogous behavior occurs for f = 1/3, as shown in Fig. 5.5a for two adjacent junctions when $\nu \geq \nu_c$. The period of the instantaneous voltage across a single junction as a function of time on the lowest step for f = 1/3 is tripled with respect to the rf drive, instead of doubled as for f = 1/2. The voltage waveforms across adjacent junctions are the same, but again are out of phase by one rf drive period. This shows that the vortex superlattice for f = 1/3 effectively moves one junction lattice unit cell per rf period when current biased on the n = 1, q = 3 fractional giant step, in support of our model.

5.5 Low Frequency Results

We have also investigated the response of the arrays to lower rf drive frequencies, specifically $\nu = 0.1\nu_c$. Since the characteristic response frequency of the junctions, ν_c, is 10 times faster than the drive frequency in this regime, the vortices can respond more quickly to the rf current, slipping into adjacent cells in a time $\sim 1/\nu_c = 0.1/\nu$. This is shown in Fig. 5.5b, where we have plotted the instantaneous voltage across two adjacent junctions parallel to the external current (the same junctions 1 and 2 shown in Fig. 5.1) for a current at the center of the lowest (n = 1) fractional giant step for f = 1/2. The junctions in the

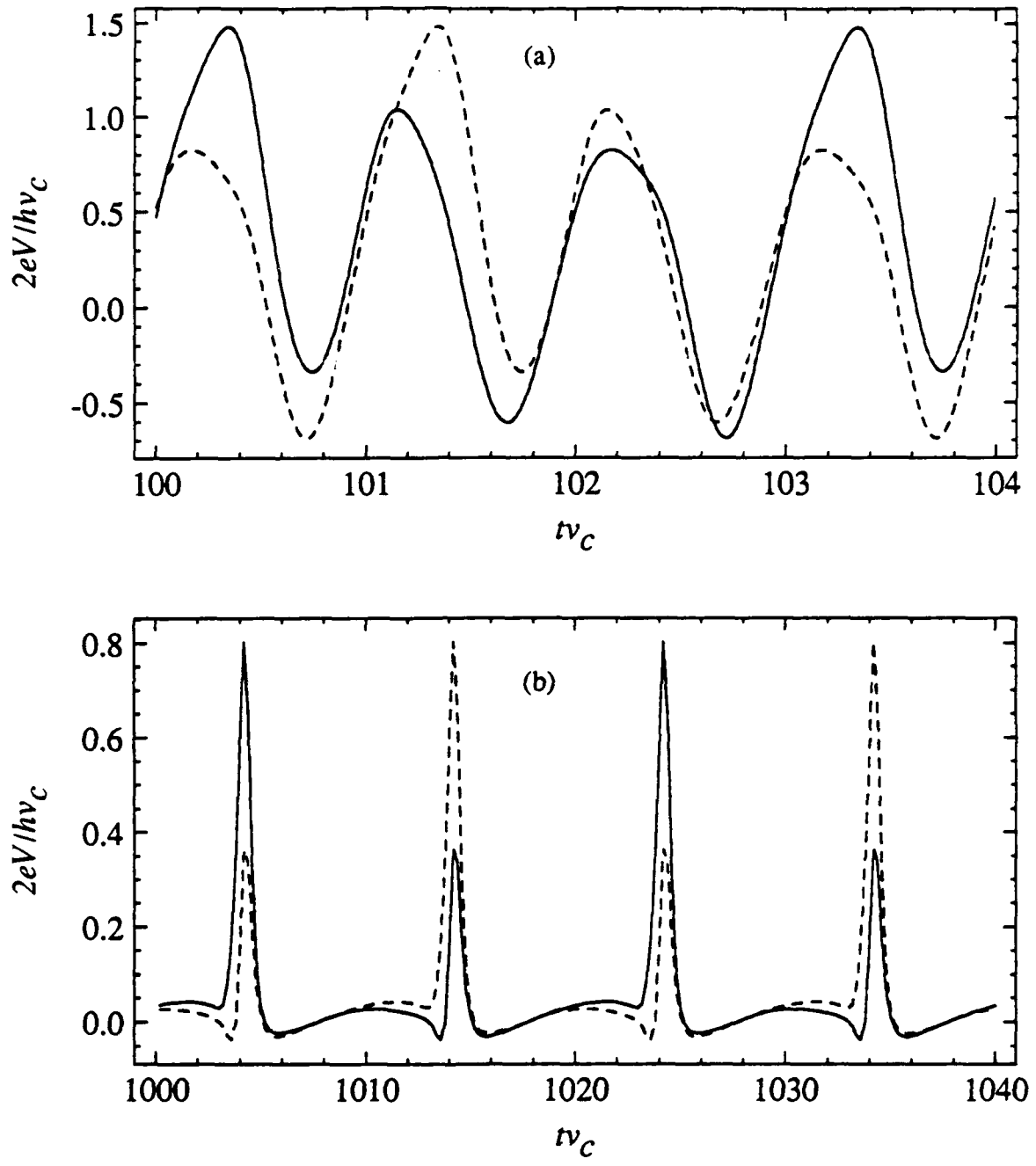

Fig. 5.5. Normalized instantaneous voltage *vs.* normalized time across two adjacent junctions parallel to the transport current: (a) for a 3x6 junction array on the n = 1, q = 3 fractional giant step, with f = 1/3, $\nu = \nu_c$, $i_{rf} = i_c$, and $i_{dc} = 0.47i_c$, and (b) for a 4x5 junction array on the n = 1, q = 2 fractional giant step, with f = 1/2, $\nu = 0.1\nu_c$, $i_{rf} = 0.2i_c$, and $i_{dc} = 0.25i_c$. Time is normalized to the characteristic period, $1/\nu_c$.

array still collectively lock to the same voltage so that the steps are given by (5.1.1). For a large portion of the rf period, ~0.9/ν, the vortex superlattice is essentially at rest and then each vortex slips quickly into its adjacent cell in a time ~$1/\nu_c$. This is shown by the relatively long flat voltage followed by the narrow spike when the vortex superlattice slips. The two junctions have the same voltage waveform, which is period doubled with respect to the rf drive, but are out of phase by exactly one rf period. Thus we see the same behavior, *i.e.* period doubling and adjacent junctions being out of phase by one rf period, as we did in Fig. 5.3 for the same junctions at a higher frequency ($\nu \sim \nu_c$), except that the voltage waveforms are much different at this lower frequency because the response of the junctions is much faster than the drive frequency.

For these low frequencies $\nu < \nu_c$, the response of the vortices will be faster than the rf drive so that the vortex superlattice may deform for short intervals within rf periods. It is not unlikely that vortex lattice shear or some other more complicated deformation of the vortex superlattices could occur. If a row of vortices can shear past its adjacent rows at these low frequencies, the voltage across the array will be determined by the number of moving vortices and distance they move in a given rf period. If this motion locks to the rf drive frequency, 'subharmonic' fractional giant steps would occur at voltages

$$\langle V_n \rangle = \frac{n}{m}\left(\frac{N}{q}\right)\frac{h\nu}{2e}, \qquad n = 0,\ 1,\ 2,\ldots,\ \text{and}\ \ m = 1,2,\ldots, \tag{5.5.1}$$

for any value of q. We have observed some experimental indications of a possible 'subharmonic' step for f = 1/3 but the step widths are small at these frequencies and much too rounded by thermal noise for explicit confirmation.

Our simulations for f = 1/3 at these low frequencies, namely $\nu = 0.1\nu_c$, do show new steps. In Fig. 5.6 we see not only the fractional giant Shapiro steps, but *subharmonic* fractional giant steps at one-half the fractional step voltage, so that m = 2 in (5.5.1). No

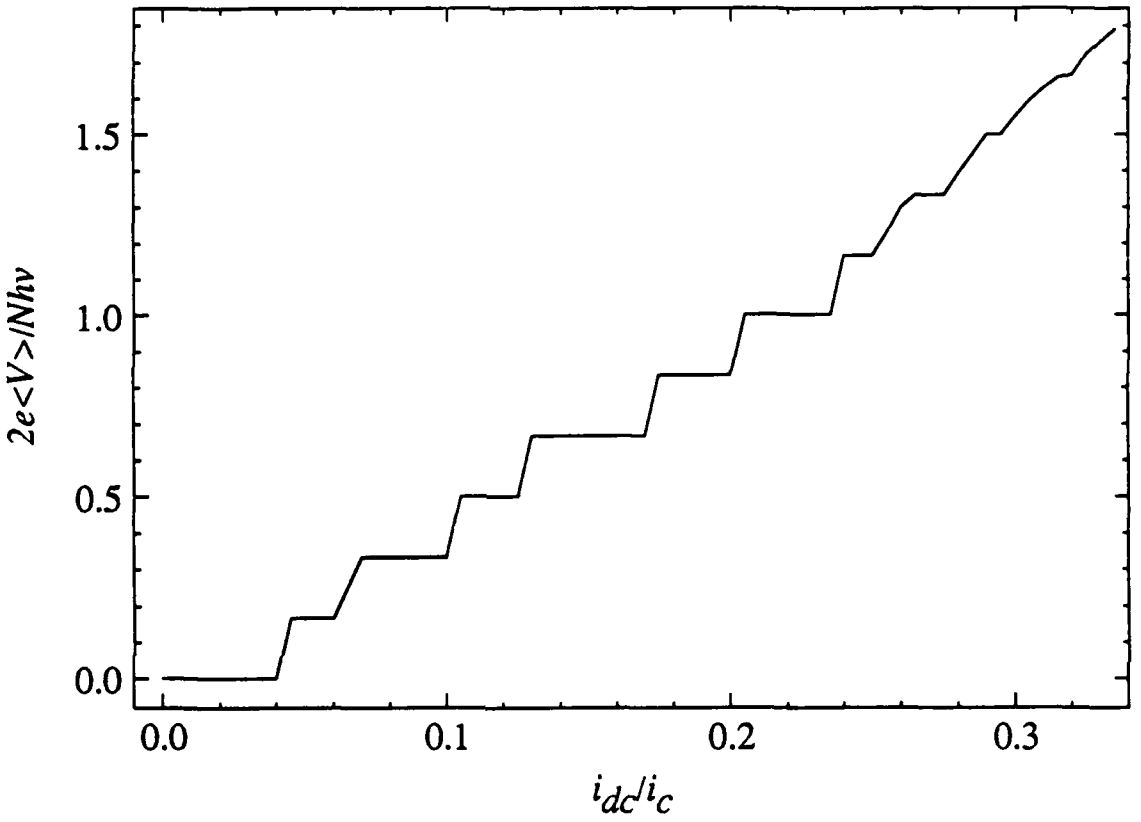

Fig. 5.6. Normalized time-averaged voltage *vs.* normalized dc current per junction for a simulated 3x6 array with $\nu = 0.1\nu_c$, $i_{rf} = 0.2i_c$, and magnetic field f = 1/3. *Subharmonic* fractional giant steps appear halfway between the fractional giant steps of the f = 1/3 I-V curve in Fig. 5.2.

subharmonic steps were observed, though, for f = 1/2 at low frequencies. These steps are similar to those reported by Lee *et al.* (1990), specifically for *odd* values of q, where they suggested that sublattices of the original superlattice are moving and locking to the rf period.[3] We emphasize that these subharmonic fractional steps, if they can be shown to exist experimentally and are not an anomalous result of the simulations' boundary conditions, are a result of vortex motion and thus are entirely different from the subharmonics found in single underdamped junctions for frequencies near the plasma resonant frequency. Further work is required to clarify whether this phenomenon is a result of boundary conditions or an intrinsic property of the superlattice response.

The exact current-phase relations for the f = 1/2 and f = 1/3 superlattices discussed in Section 3.6 also suggest the possibility of subharmonic steps for commensurate fields. The renormalization picture mentioned in that section, replaces superlattice unit cells with single junctions, which have only approximately sinusoidal current-phase relations. Using this renormalization, the fractional giant step voltage relation (4.1.2) reduces to the giant step relation (4.1.1), $V_n = nN'(h\nu/2e)$, because there are effectively N' = N/q renormalized junctions across the array. Since the current-phase relations for these renormalized junctions are not perfectly sinusoidal, subharmonic steps become possible as suggested for single overdamped junctions by Renne and Polder (1974).

[3]Recently (at the 1990 APS March meeting), Lee *et al.* have retracted their 'subharmonic' step results, claiming that they were a result of their free boundary conditions. However, our 'subharmonic' fractional giant steps *were* observed using periodic boundary conditions, but for much smaller-sized arrays than those simulated by Lee *et al.* At these low frequencies for f = 1/3 the vortex superlattice is very distorted and there is not a symmetric period-tripled voltage waveform analogous to the waveform for f = 1/2 at low frequency in Fig. 5.5b.

5.6 Conclusion

In conclusion, we have performed RSJ model simulations on arrays of overdamped Josephson junctions and studied their dynamical response to applied rf currents in the presence of a magnetic field. The results show fractional giant Shapiro steps at voltages in agreement with the experimental observations discussed in Chapter 4. By following the response of adjacent junctions in the array, we have shown that on fractional giant steps, the vortex superlattice does indeed slip perpendicular to the applied current in synchrony with the rf drive current as proposed in the vortex motion model. We have found interesting and complex dynamical behavior in the simulations that have shown subharmonic fractional giant steps for $f = 1/3$ at low frequencies.

CHAPTER 6

THE SUPERCONDUCTOR-NORMAL PHASE BOUNDARY IN POSITIONALLY DISORDERED ARRAYS

6.1 Introduction

Many superconductors are not homogeneous, but contain voids, normal regions, or regions with weaker superconducting properties. Disorder plays an important role in these materials because the positions or sizes of the normal or superconducting regions may vary randomly. Granular superconductors, which consist of weakly Josephson-coupled grains, are one example of disordered superconductors, and have been studied both in bulk and as thin films. Disorder in these materials is evident in many forms, including randomness in grain sizes, coupling strength between grains, and grain positions (Shih *et al.*, 1984; and Tinkham and Lobb, 1989). High-T_c superconducting oxides are the most recent and exciting examples of this class of disordered materials.

Superconducting arrays of weakly-coupled Josephson junctions have recently been investigated both theoretically and experimentally as a system where positional disorder can be introduced deliberately. Invoking a renormalization group analysis by Rubinstein, Shraiman and Nelson (1983), Granato and Kosterlitz predicted (in 1986) both a disorder-dependent critical field for the destruction of quasi-long-range order and a reentrant phase transition when positional disorder was introduced. The results of experiments on positionally disordered Josephson junction arrays have been previously reported by Forrester *et al.* (1987 and 1988). By analysis of structure in the magnetoresistance measured in such samples, it was possible to extract a critical field beyond which quasi-long-range phase coherence was destroyed (Forrester *et al.*, 1988). This field was in good

agreement with the prediction of Granato and Kosterlitz. However, the most prominent experimental result, the decay of the principal resistance oscillations, has not been explicitly dealt with in any existing theory. This chapter[1] will briefly review this unresolved result and then describe mean-field simulations we have performed to interpret it.

6.2 Experimental Results

Experiments were performed on two-dimensional thin film arrays of proximity-effect junctions, consisting of cross-shaped superconducting Pb islands, weakly coupled through a normal metal underlayer (Forrester *et al.*, 1987 and 1988). Positional disorder was quantitatively introduced by displacing the centers of the islands by a small random amount, $\delta \mathbf{r} = (\delta x, \delta y)$, given by a truncated uniform probability distribution, $P(\delta \mathbf{r}) = P_x(\delta x) \cdot P_y(\delta y)$:

$$P_x(\delta x) = \begin{cases} \dfrac{1}{2\Delta^*} & -\Delta^* < \dfrac{\delta x}{a} < \Delta^* \\ 0 & \text{otherwise} \end{cases}, \qquad (6.2.1)$$

where a is the regular array lattice constant. When the islands were displaced, the edges forming the junctions, *i.e.* the tips of the crosses, were constrained to remain on their periodic lattice positions, as shown in Fig. 6.1a, in order to preserve uniformity in the junction critical currents.

The array resistance, R, was measured as a function of the average number of flux quanta per unit cell, f_o. In samples without deliberate disorder, $R(f_o)$ showed principal oscillations periodic in integer f_o, as well as fine structure at higher order rational values of f_o, *i.e.* strongly commensurate fields where $f_o = p/q$ (see Section 1.4), as seen previously

[1]Much of this chapter has been published in Benz *et al.*, (1988).

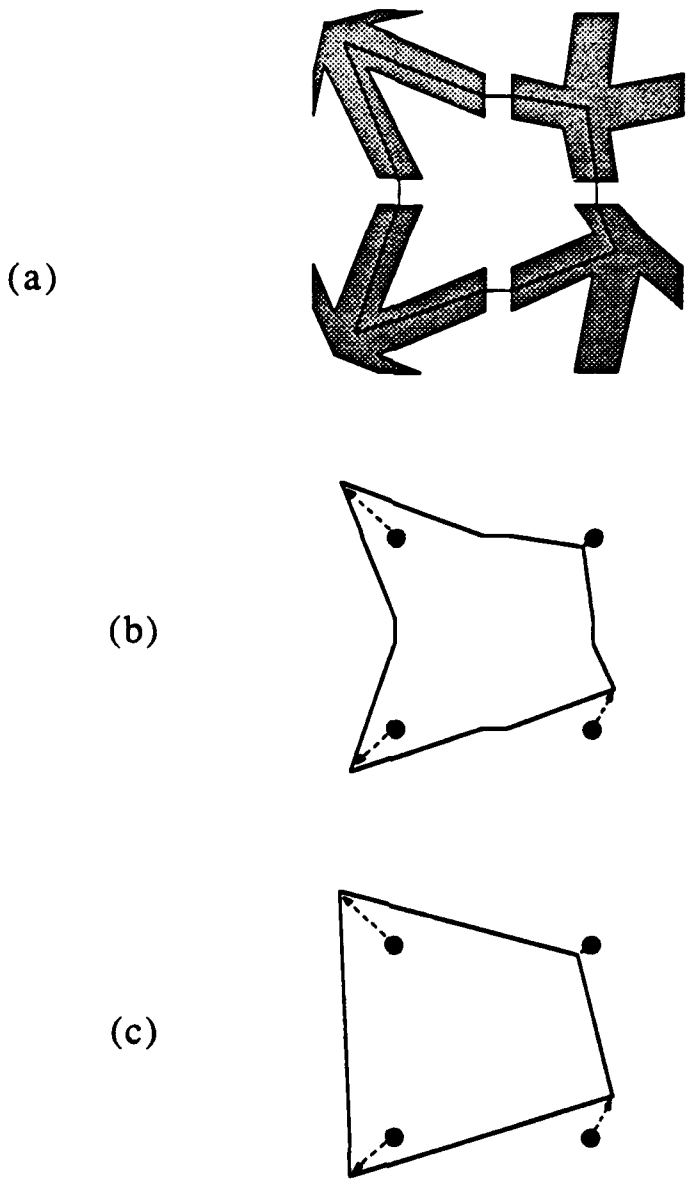

Fig. 6.1. (a) Typical unit cell in a proximity-coupled array. Distorted crosses are superconducting islands. Solid line was added to emphasize junction constraints. (b) Typical wire network unit cell emphasizing wire constraints, analogous to (a). (c) Wire network unit cell without constraints. The nodes in (a), (b) and (c) are displaced by the same amount.

in both junction arrays (Tinkham *et al.*, 1983; Webb *et al.*, 1983; Kimhi *et al.*, 1984; and Brown and Garland, 1986) and wire networks (Pannetier *et al.*, 1984). The principal oscillations in samples with disorder were found to decay with increasing field at a rate depending on the amount of disorder, as illustrated in Fig. 6.2. By measuring samples with various values of Δ^*, and correcting for single junction effects,[2] it was found that the peak-to-peak amplitude of the principal oscillations decayed within an approximately linear envelope, disappearing at a critical field, f_c, given by (Forrester *et al.*, 1987 and 1988)

$$f_c \cdot \Delta^* \approx 0.95 \ . \qquad (6.2.2)$$

Granato and Kosterlitz (1986) predict the same proportionality between the disorder and their critical field for integer f_o, but their proportionality constant is an order of magnitude lower. This is because the experimental critical field, as defined here, measures destruction of correlations over a single unit cell, while the prediction by Granato and Kosterlitz is for quasi-long-range order (see Forrester *et al.*, 1988). Fluctuations greatly influence quasi-long-range-order, but have less effect on short-range correlations. The Ginzburg-Landau mean-field theory, without corrections for thermal fluctuations (Teitel and Jayaprakash, 1985), might explain the decay of the principal oscillations.

6.3 The Ginzburg-Landau Equations and Simulation Algorithm

The Ginzburg-Landau equations have been used to calculate the phase boundaries of many different wire networks, including ordered (Alexander, 1983; Pannetier *et al.*, 1984; Fink *et al.*, 1982; Rammal *et al.*, 1983; and Simonin *et al.*, 1983), quasiperiodic (Nori *et*

[2]Single junction effects cause the gradually rising background in the data of Fig. 6.2, as well as an additional modulation of the resistance oscillations (see Section 3.3.3, and Forrester *et al.*, 1987 and 1988).

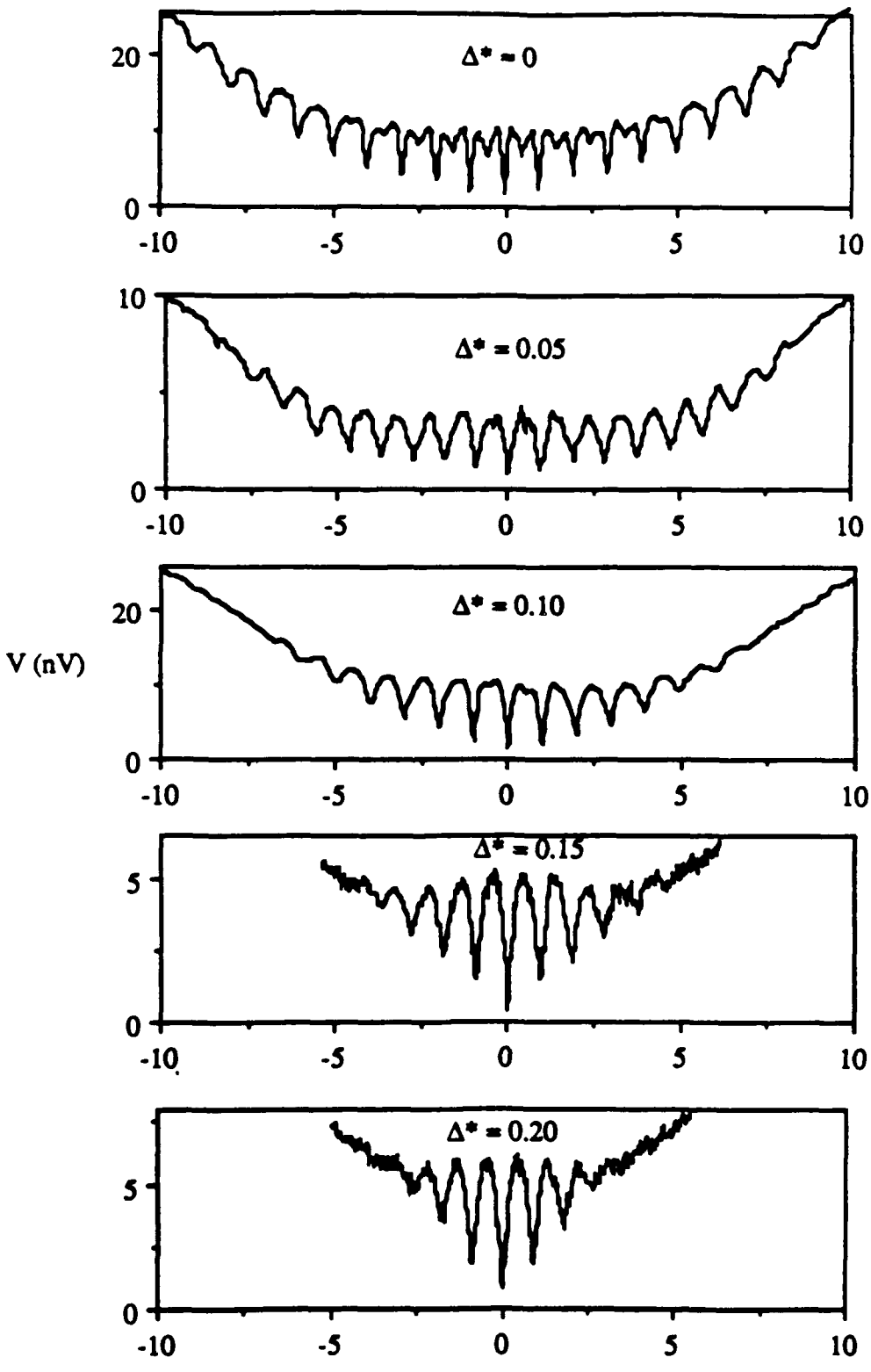

Fig. 6.2. Voltage (at I = 10μA) *vs.* magnetic field (in average number of flux quanta per unit cell, f_o) for experimental arrays with various amounts of disorder, Δ* (from Forrester, *et al.*, 1988, and Forrester, 1988).

al., 1987 and Nori and Niu, 1988) and fractal networks (Rammal and Toulouse, 1982). The measured change in resistance, $\delta R(f_o)$, of wire networks and Josephson arrays is roughly proportional to the change in the critical temperature, $\delta T_c(f_o)$.[3] Mean-field calculated phase boundaries are in excellent agreement with experiments on wire networks (Pannetier *et al.*, 1984; Gordon *et al.*, 1986; Behrooz *et al.*, 1986; and Santhanam *et al.*, 1988). They have also compared well with resistance oscillations in quasiperiodic Josephson arrays (Springer and Van Harlingen, 1987).

The Ginzburg-Landau mean-field theory does not determine the exact phase transition temperature for our arrays, because it neglects vortex fluctuations close to T_c. It is, however, a very good approximation (see Teitel and Jayaprakash, 1985), especially for strongly coupled junctions, and will provide a useful comparison for the primary resistance oscillations, which were measured above T_c. Therefore we use this mean-field calculation for $T_c(f_o)$ to predict the qualitative behavior of the magnetoresistance in the experimental Josephson junction arrays with positional disorder.

We assume the linearized Ginzburg-Landau equations,

$$\left(i\vec{\nabla}_l + \frac{2\pi\vec{A}(l)}{\Phi_0}\right)^2 \psi - \xi(T)^{-2}\psi = 0, \tag{6.3.1}$$

$$\vec{J} = -\left(\frac{e\hbar}{2m}\right)\left[\psi^*\left(i\vec{\nabla}_l + \frac{2\pi\vec{A}(l)}{\Phi_0}\right)\psi - \psi\left(i\vec{\nabla}_l - \frac{2\pi\vec{A}(l)}{\Phi_0}\right)\psi^*\right], \tag{6.3.2}$$

are valid on a network of one-dimensional wires. The supercurrent density, $\vec{J}$, the vector potential, $\vec{A}(l)$, and the gradient, $\vec{\nabla}_l = \hat{l}\,\partial/\partial l$ are vectors along the path l of the wire.

[3]Experimentally in junction arrays, the resistance is measured with a small current at a fixed temperature above the zero field critical temperature, $T > T_c(0)$. In this case $\delta R(f_o,T) \approx \delta T_c(f_o) \cdot (dR/dT')|_T$ (Tinkham *et al.*, 1983).

$\xi(T)$ is the temperature dependent coherence length and Φ_0 is the flux quantum. These equations have a solution for the order parameter, $\psi(l)$, at a distance l along a single branch from node m to node n of length L_{mn},

$$\psi(l) = \frac{e^{i\gamma_{ml}}}{\sin\left(\frac{L_{mn}}{\xi(T)}\right)}\left[\psi_m \sin\left(\frac{L_{mn}-l}{\xi(T)}\right) + \psi_n e^{-i\gamma_{mn}} \sin\left(\frac{l}{\xi(T)}\right)\right], \qquad (6.3.3)$$

where γ_{mn} is the integral of the magnetic vector potential along the wire from node m to node n,

$$\gamma_{mn} = \frac{2\pi}{\Phi_0}\int_m^n \vec{A}(l)\cdot d\vec{l} \ . \qquad (6.3.4)$$

$\psi_m = |\psi_m| e^{i\phi_m}$ is the value of the order parameter at node m. In our square network, each node is connected to four nearest neighbors, $1 \le n \le 4$. Current conservation then gives the following equation at each node m in the network,

$$\sum_{n=1}^{4}\left[-\psi_m \cot\left(\frac{L_{mn}}{\xi(T)}\right) + \psi_n \frac{e^{-i\gamma_{mn}}}{\sin\left(\frac{L_{mn}}{\xi(T)}\right)}\right] = 0 \ , \qquad (6.3.5)$$

For an ordered array, this equation is greatly simplified because the length $L_{mn} = a$ is a constant throughout the network. However, in a disordered array, the lengths between nearest neighbors are random, and for an NxN array (6.3.5) becomes a set of N^2 coupled, complex equations.

For a given f_o, we solved this set of equations by adjusting the coherence length, $\xi(T)$, to find the highest-temperature solution, which defines $T_c(f_o)$. The coherence length, in mean-field theory, is related to the critical temperature at f_o by the following relation:

$$\left(\frac{a}{\xi[T_c(f_o)]}\right)^2 = [T_c(0) - T_c(f_o)]\frac{a^2}{\xi(0)^2 T_c(0)} \equiv [\delta T_c(f_o)]\cdot\alpha \ , \qquad (6.3.6)$$

where a is the lattice constant, and $\alpha = a^2/\xi(0)^2 T_c(0)$ is a positive constant. Equation (6.3.6) is the calculated change in the critical temperature that we wish to compare with the measured change in the resistance of the junction arrays, $\delta T_c(f_o) \propto \delta R(f_o)$. (Note that $\delta T_c(f_o)$ is defined as the *downward* shift of the phase transition temperature from the zero field value, since $\alpha > 0$.)

We solved (6.3.5) for NxN arrays, with N = 4, 8, 12, 16 and 24, all having periodic boundary conditions in both directions. Without disorder we found the usual phase boundary that is periodic in integer f_o (note that $f_o = f$ for a regular array), with the expected fine structure at the strongly commensurate fields, f_o = 1/2, 1/3, 1/4, *etc.*, for a square array (see Fig. 6.3). When we introduced disorder, we considered three different cases with various types of site displacements and unit cells. In the first case (G) we displaced the nodes with a *Gaussian* probability distribution, of variance Δ_G, and then connected the nodes with straight wires to form four-sided unit cells, as shown in Fig. 6.1c. This is analogous to the situation considered by Granato and Kosterlitz (1986) for junction arrays. For the second case (U), we used a *uniform* probability distribution (6.2.1), truncated at half-width Δ_U, to avoid the tails associated with the Gaussian distribution, with the same unit cell shape as in (G). And for the third case (P), we modeled the experimental disordered arrays more closely. Twelve-sided *polygon*-shaped unit cells were created by constraining the center segment, of length equal to that of the

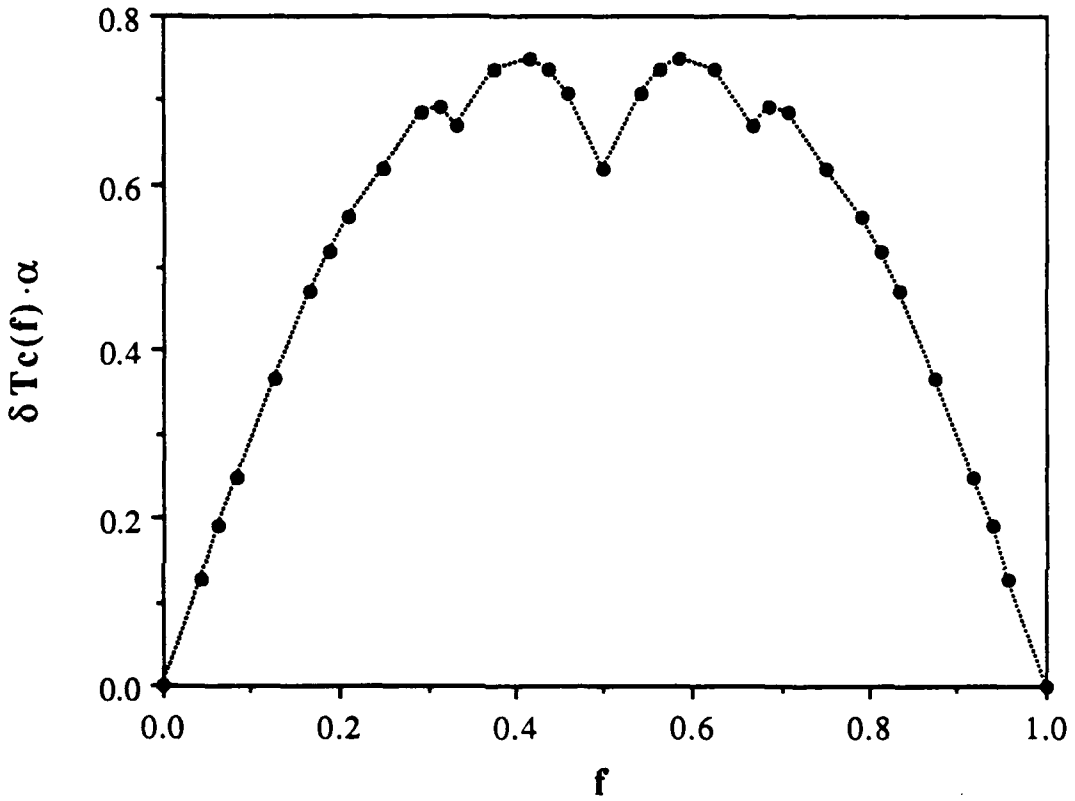

Fig. 6.3. Decrease in critical temperature *vs.* magnetic field (in flux quanta per unit cell, f) for a uniform array. See (6.3.6) for the relation between $\delta T_c(f)\cdot\alpha$ and $T_c(f)$. Data is combined from runs on 16x16 and 24x24 arrays. Notice that we only calculate $T_c(f)$ for values of field commensurate with the particular size lattice, *e.g.* for an 8x8 network we calculate T_c for $f = m/8$, where m is an integer. Thus larger arrays show higher order fine structure.

junction (= $0.15a$), along each wire (Fig. 6.1b) and then displacing the nodes with a uniform distribution (6.2.1), of half-width Δ_P. Cases (G) and (U) simulate different disorder distributions on the same shaped unit cells (four-sided), while cases (U) and (P) simulate the same disorder distribution (uniform) on different unit cell shapes.

6.4 Simulation Results and Discussion

Typical results for an 8x8 network for each of the three cases are shown in Fig. 6.4, where $\Delta_G = \Delta_U = \Delta_P = 0.1$. Each graph represents an average over many disorder realizations to reduce finite-size fluctuations in the individual realizations. Note that $T_c(f_o)$ still oscillates periodically in integer f_o as in the ordered arrays, but there is no fine structure. Unlike the ordered case, these principal oscillations in $T_c(f_o)$ decrease within an approximately linear envelope with increasing field, similar to the experimental resistance oscillations (see Section 6.2). As in the experiments, we define a critical field, f_c, by extrapolating the envelope of the oscillations to the field where its amplitude goes to zero. Above f_c the critical temperature fluctuates weakly about a constant value. Note that f_c is different in each case, although the respective Δ's are the same, showing that both disorder distribution and unit cell shape are important for determining f_c. Calculations for various amounts of disorder show that this critical field is inversely proportional to the amount of disorder. In the case (P) most analogous to our experimental junction arrays we find that

$$f_c \cdot \Delta_P \approx 1.0 \ , \qquad (6.4.1)$$

which agrees very well with the experimental result (6.2.2).

Figure 6.5 shows data for 12x12 networks, where different amounts of disorder were chosen for each case in order to get the same critical field. This occurred when the amount of disorder was chosen so that each case had the same fractional root-mean-square

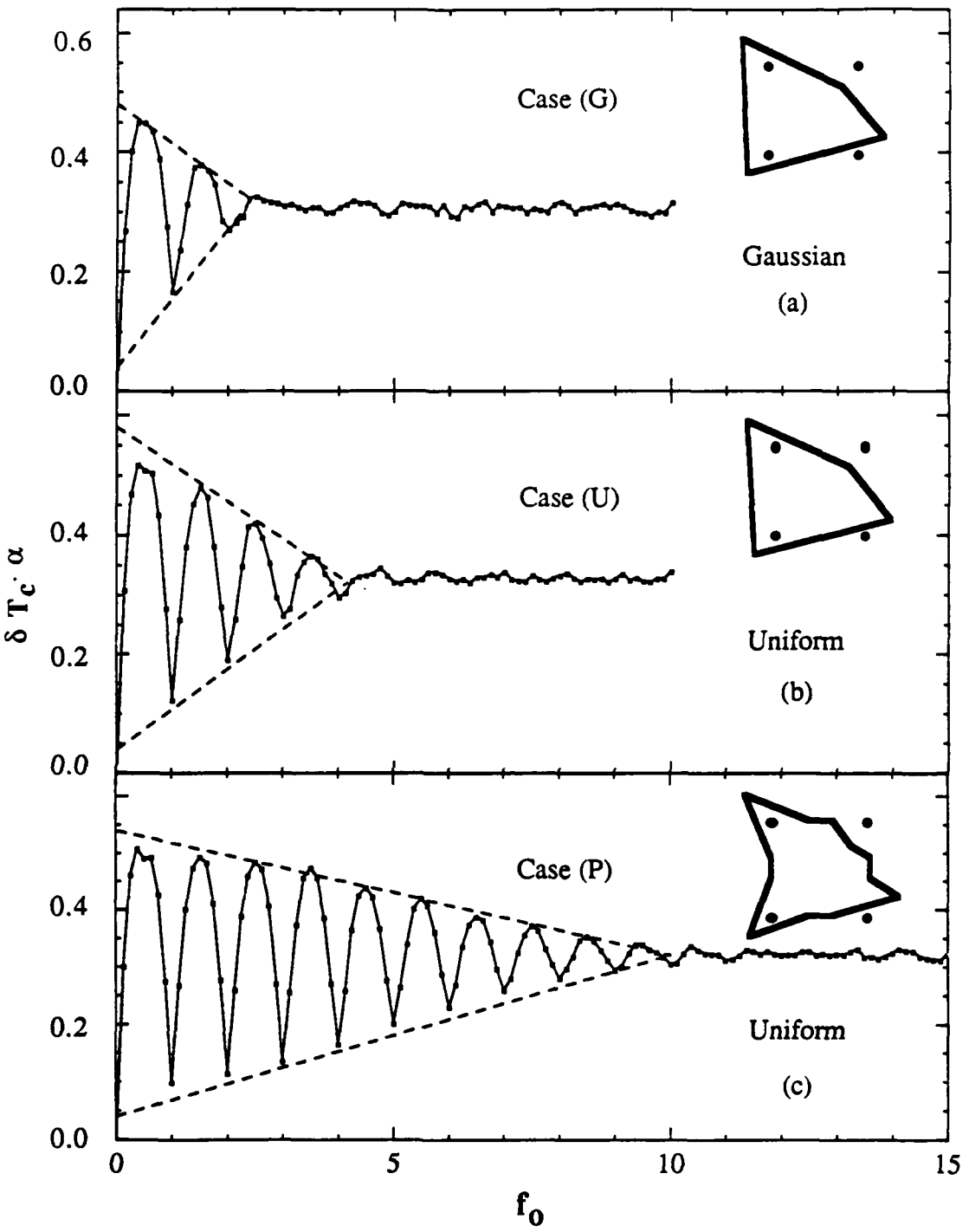

Fig. 6.4. Decrease in critical temperature *vs.* magnetic field for 8x8 arrays with disorder. (a) Case (G), with $\Delta_G = 0.1$, averaged over 25 realizations. (b) Case (U), with $\Delta_U = 0.1$, averaged over 26 realizations. (c) Case (P), with $\Delta_P = 0.1$, averaged over 52 realizations. Dashed lines show approximate envelope used to define f_c.

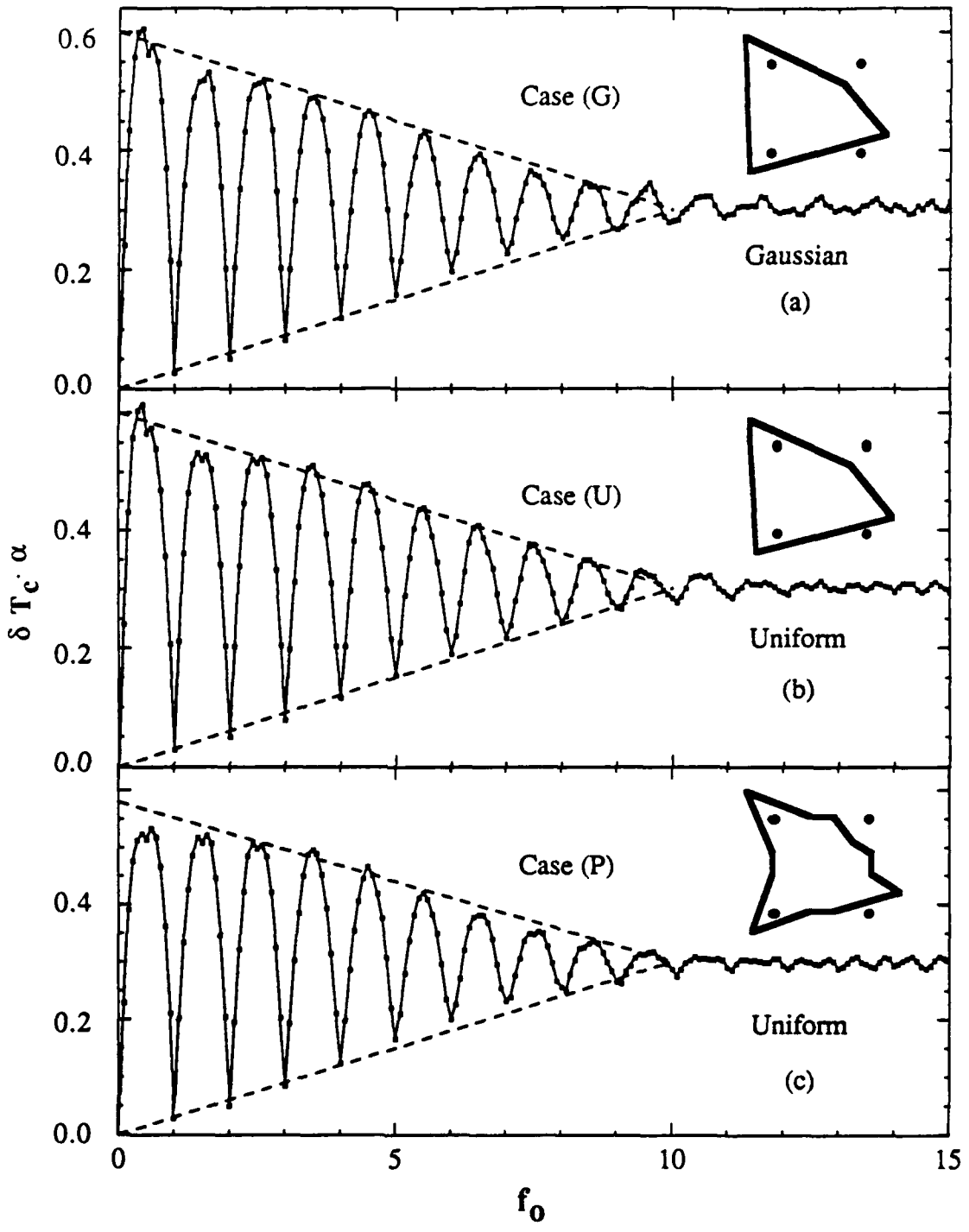

Fig. 6.5. Decrease in critical temperature *vs.* magnetic field for 12x12 arrays with disorder, averaged 15 realizations each. (a) Case (G), with $\Delta_G = 0.02404$. (b) Case (U), with $\Delta_U = 0.0408$. (c) Case (P), with $\Delta_P = 0.1$. Dashed lines show approximate envelope used to define f_c.

unit cell area fluctuations, σ^{A}_{rms}. This quantity depends on both disorder distribution and unit cell shape. The rms area fluctuations for the three cases can be shown to have the following values

$$\sigma^{A}_{rms} = \sqrt{2}\Delta_G = \frac{\sqrt{2}}{\sqrt{3}}\Delta_U = \frac{\sqrt{2}}{4.16}\Delta_P \quad . \tag{6.4.2}$$

The first two expressions were determined analytically and the last numerically. Expressing (6.4.1) in terms of rms area fluctuations, or equivalently rms flux fluctuations, our results for all three cases are consistent with

$$\left(\frac{\delta\Phi_{rms}}{\Phi_0}\right)_c = f_c \cdot \sigma^{A}_{rms} \approx 0.34 \quad . \tag{6.4.3}$$

Thus, the oscillations in $T_c(f_o)$ disappear when the rms flux fluctuations reach approximately a third of a flux quantum, Φ_o, in each unit cell. It is not obvious why this value should be so close to 1/3, but it is reasonable that it is less than 1/2.

By comparing Figs. 6.4(c) and 6.5(c), which represent the same amount of disorder but different size arrays, one can see that the critical field is indeed the same, thus demonstrating the size independence of (6.4.1). However, some small amplitude oscillations which persist even beyond f_c are more obvious in Fig. 6.5. This is a result of insufficient disorder averaging, as can be seen by comparing with the data in Fig. 6.4, where more averaging has substantially reduced the fluctuations.

6.5 Other Notable Features

Other interesting results have been found from these mean-field simulations that require further investigation. For integer f_o, positional disorder causes $T_c(f_o)$ to *decrease* with increasing f_o. However, for some fractional f_o, such as the fully-frustrated half-integer f_o case, the $T_c(f_o)$ *increases* as f_o approaches f_c, leading to the conclusion that positional disorder relieves the frustration of the array at higher fields for more frustrated values of f_o. For $f_o > f_c$, the phases become random for all f_o, resulting in a T_c that is between the critical temperatures of the integer and half-integer f_o cases without disorder. This high-field T_c depends on the size of the array, but remains independent of f_o, even for very large f_o. Extrapolating to large arrays we find $\delta T_c(f_o) \cdot \alpha \approx 0.27$ for $f_o > f_c$. This numerical result has not yet been explained theoretically.

Finally, arrays with very small positional disorder show interesting behavior for $f_o << f_c$. *In this low-field region, as shown in Fig. 6.6, fine structure is present* at strongly commensurate fields as found in ordered wire or junction arrays and in disordered junction arrays (Forrester *et al.*, 1988). Furthermore, the $T_c(f_o)$ principal oscillations in this region decay at a faster rate than those discussed above. This low-field decay rate scales only with the rms site displacements,[4] as opposed to the rms unit cell area fluctuations discussed above, because a uniform distribution with $\Delta_U = 0.004$ gives the same decay rate as the Gaussian distribution with $\Delta_G = 0.00231$ and is independent of the unit cell shape, *i.e.* cases (P) and (U) give the same low-field decay rate since they have the same uniform probability distribution. However, the low-field decay rate is also array-size dependent, since it was found that the rate increases with increasing sample size, so that the 'cross-over' field ($f_o \sim 7$ in Fig. 6.6), defined as the field above which the decay rate is determined by rms area fluctuations as discussed above, goes to zero as the array size is

[4]The scaling factor between the Gaussian and uniform probability distributions for the rms site displacements in 2D is $\Delta_G = \Delta_U/\sqrt{3}$.

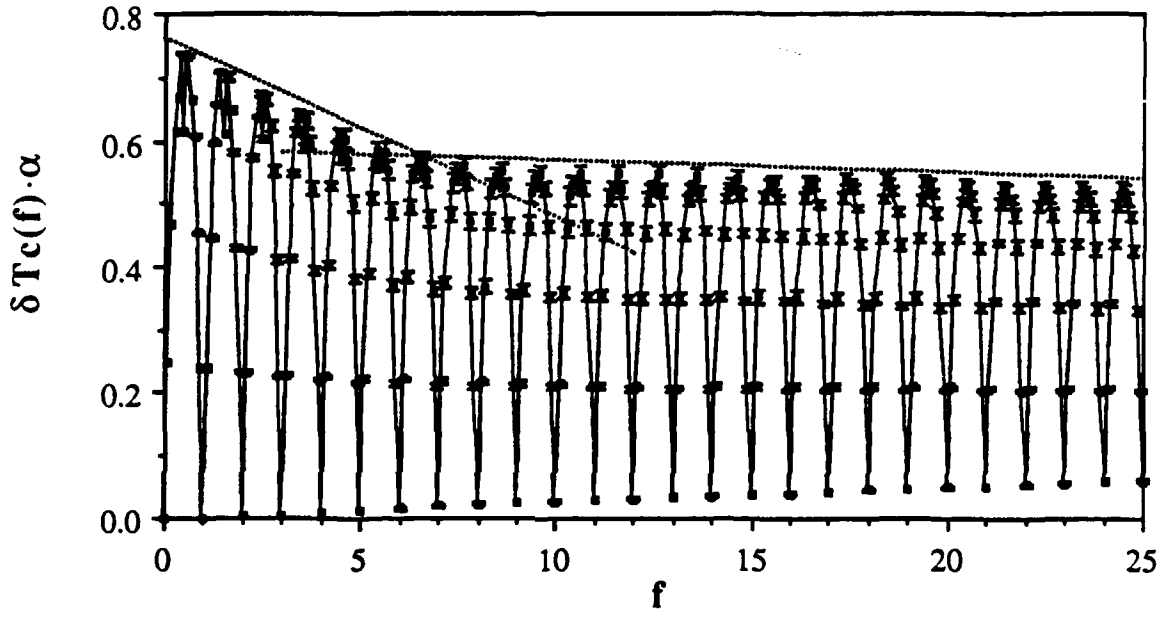

Fig. 6.6. Decrease in critical temperature *vs.* magnetic field averaged over 10 realizations for a 12x12 array with weak positional disorder defined by a Gaussian distribution (case G), with $\Delta_G = 0.00231$. Note the faster decay rate for the principal oscillations at low f, crossing over to more slowly decaying principal oscillations at $f_o = 7$, as indicated by the intersection of the dashed lines. Fine structure is present within the low field envelope. The same decay rate occurs for cases (P) and (U) when $\Delta_P = 0.004$ and $\Delta_U = 0.004$, indicating that this low-field decay rate is independent of unit cell area or shape.

increased. Further simulations are necessary to extrapolate these results to the infinite-sample limit.

6.6 Conclusion

We conclude that the behavior of $T_c(f_o)$ oscillations as determined by mean-field simulations on positionally-disordered wire arrays is similar to measured magnetoresistance oscillations of two-dimensional Josephson junction arrays with positional disorder. Both have a critical field, defined by the disappearance of principal oscillations, that scales inversely with the amount of disorder with approximately the same proportionality constant. Further investigation is necessary, however, to determine whether mean-field theory, using the linearized Ginzburg-Landau equations, is sufficient for describing the decay of fine structure in disordered arrays.

CHAPTER 7

SUMMARY AND SUGGESTIONS FOR FUTURE RESEARCH

We have shown in the previous chapters that interesting phenomena occur in 2D Josephson junction arrays biased with large dc and rf currents. The commensurability of the magnetic field was shown to play an important role in the resulting dynamical response, particularly for the commensurate fields when the field-induced vortex superlattices are strongly coupled to the array of junctions.

Our investigation of the dc properties showed that the peak in the dynamic resistance *vs.* current curves in zero field was an excellent measure of the intrinsic array critical current I_{co}. We observed similar peaks in the dynamic resistance for other commensurate magnetic fields, and, using the analogy with the zero field case, interpreted them as depinning currents for the commensurate vortex superlattices. Our exact calculations of the critical current for the f = 1/2 and 1/3 cases were shown to be in good agreement with our experimental results and with previous theoretical results.

We discussed the effects of rf currents on the phase-locking dynamics of the array. In zero field, we observed *giant* Shapiro steps at voltages 1000 times that expected for a single junction, $V_n = nNh\nu/2e$, where N = 1000 is the number of junctions in the direction of applied current. When a commensurate magnetic field is applied, we showed that *fractional* giant steps appear at voltages, $V_n = n(N/q)h\nu/2e$, directly related to the vortex superlattice unit cell size, q. We presented a model based on the locking of the motion of the vortex superlattice with the applied rf current to explain these novel steps.

Computer simulations were performed on arrays of resistively shunted Josephson junctions in a perpendicular magnetic field and *fractional* giant Shapiro steps were found in the simulated current-voltage characteristics in agreement with our experimental

measurements. The detailed motion of the magnetic field-induced vortices was shown to be in agreement with our phenomenological model, through investigations of the instantaneous voltage across adjacent junctions in the array. We presented further results at low frequencies that indicated the possibility of *subharmonic* fractional giant steps.

Finally, we reported the results of mean-field simulations of superconducting wire networks with positional disorder. These simulations were performed in order to explain the decay of the magnetoresistance oscillations experimentally observed in positionally-disordered Josephson junction arrays. Using the linearized Ginzburg-Landau equations we numerically determined the transition temperature, T_c, as a function of the average number of magnetic flux quanta per unit cell, f_o, for different amounts of disorder. We found that $T_c(f_o)$ exhibited decaying oscillations, periodic in f_o, whose amplitude went to zero at a disorder-dependent critical field, f_c. Our calculated value of this critical magnetic field was shown to be in excellent agreement with that found from our experimental magnetoresistance measurements on Josephson junction arrays.

We have presented experimental results on 2D Josephson arrays, and explained them with various theoretical models and calculations, but many interesting experiments, theoretical calculations, and simulations remain to be completed in order to fully understand the dynamical properties of arrays. The physical properties of the real (experimental) arrays, such as the geometrical inductance, self-induced fields and vortices, *etc.*, were shown to be very important for understanding the true dynamical behavior of the arrays in certain temperature regimes, as well as causing interesting dynamical effects, such as the zero-field 'subharmonic' steps. Simulations can be performed that include these 'real' properties, such as the geometrical inductance, to ascertain in a controlled fashion their effects on the array critical currents and fractional giant steps, and to make comparisons with the experimentally determined results. The widths of the fractional giant steps as a function of rf frequency, rf amplitude and damping, have yet to be systematically

investigated, although preliminary simulations (Lee and Stroud, 1990) and calculations (Halsey, 1990) are underway. *Subharmonic* fractional giant steps (besides the 'current-induced' zero-field steps), suggested in Section 5.5, are a very interesting possibility in the overdamped arrays, and will require careful theoretical and experimental scrutiny. Two-dimensional arrays of underdamped junctions are expected to have even more complicated dynamical properties because of the hysteretic response of the junctions.

The addition of disorder to arrays may also lead to more complicated vortex superlattice motion, pinning, and subharmonic steps that can be investigated both experimentally and theoretically. We have made preliminary dynamical measurements on overdamped arrays with positional disorder, like those discussed in Chapter 6. Interesting subharmonic fractional giant steps, independent of q, have been observed for *all* magnetic fields, which appear to die out more quickly at higher voltages for larger amounts of disorder, just as the fine structure in the magnetoresistance decays with increasing f_o in Chapter 6. These results can be understood qualitatively in our model because the disorder breaks the symmetry of the array and, hence, the vortex superlattices become distorted, destroying the coherent motion of the vortices.

The possibility of coherent phase-locking of the junctions in the 2D arrays to their own radiation, without externally applied rf currents, is another interesting phenomena that remains to be explored. This *mutual* phase-locking in arrays of junctions was originally proposed by Tilley (1970) and has been sought by many authors using series arrays. (For reviews of this subject see Jain *et al.*, 1984, and Hansen and Lindelof, 1984.) Arrays of junctions that can emit reasonable power levels ($\geq$1mW) to typical $\geq 50\Omega$ loads, will have potentially useful applications as voltage-controlled oscillators at high-frequencies ($\nu > 100$GHz) up to the superconducting gap frequency. Hadley (1989) has shown that critically damped ($\beta_c \approx 1$) series and 2D arrays have a stable in-phase solution and, thus, could possibly emit coherent radiation (also see Hadley *et al.*, 1988). Even though the impedance and characteristic frequency of our arrays are much to low for use in practical

devices, our results have shown that phase-locking to *externally* applied rf currents is possible in very large 2D arrays. Two-dimensional arrays could have a number of advantages over series arrays for this application: (1) the quasi-long-range coupling throughout the 2D array could improve the coherence and mutual phase-locking; (2) voltage-locking may also be improved in 2D arrays, since they are not as detrimentally affected by non-uniform junction critical currents (as are series arrays) because the currents can redistribute through the network in compensation; (3) 2D arrays may also be 'magnetically-tunable' oscillators through the application of commensurate magnetic fields; (4) the application of commensurate magnetic fields might even improve the coherent mutual phase-locking of the junctions in the array through the presence of the vortex superlattices; and, finally, (5) the available output power from an array to a matched load (at any given frequency) goes as the square of the width of the array ($P \propto M^2$), thus making the available power and impedance matching ($R_L = (N/M)r_n$) easily adjustable by changing the length and width of the array (see Lukens *et al.*, 1989).

Finally, 2D arrays may be useful experimental systems for investigating such recent theoretical ideas in 2D condensed matter physics as 'fractional statistics'. We have casually used the term 'vortex' to describe the current patterns in our arrays in commensurate magnetic fields, but single vortices are not localized entities defined by the currents through only four junctions in a unit cell. It is possible that vortices in commensurate states have an effective fractional "charge", and thus there may be a connection between our commensurate vortex states and the 'anyon' states proposed by Wilczek in 1982 (see also Laughlin, 1983, and Halperin 1984).

REFERENCES

Abraham, David W., unpublished doctoral thesis, Harvard University (1983).

Abraham, David W., C. J. Lobb, M. Tinkham, and T. M. Klapwijk, Phys. Rev. B **26**, 5268 (1982).

Alexander, S., Phys. Rev. B **27**, 1541 (1983).

Ambegaokar, V. and B. I. Halperin, Phys. Rev. Lett. **22**, 1364 (1969).

Behrooz, A., M. J. Burns, H. Deckman, D. Levine, B. Whitehead, and P. M. Chaikin, Phys. Rev. Lett. **57**, 368 (1986).

Benz, S. P., M. G. Forrester, M.Tinkham, and C. J. Lobb, Phys. Rev. B **38**, 2869 (1988).

Benz, S. P., J. U. Free, M.S. Rzchowski, M.Tinkham, C. J. Lobb and M. Octavio, to appear in *Proceedings of the Nineteenth International Conference on Low Temperature Physics, Brighton* (1990).

Benz, S. P., M. S. Rzchowski, M. Tinkham, and C. J. Lobb, Phys. Rev. Lett. **64**, 693 (1990)a.

Benz, S. P., M. S. Rzchowski, M. Tinkham, and C. J. Lobb, submitted to Phys. Rev. B (1990)b.

Benz, S. P., M. S. Rzchowski, M. Tinkham, and C. J. Lobb, to appear in *Proceedings of the Nineteenth International Conference on Low Temperature Physics, Brighton* (1990)c.

Benz, S. P., M. S. Rzchowski, M.Tinkham, C. J. Lobb, and G. O. Zimmerman, Bull. Am. Phys. Soc. **34**, 845 (1989).

Brown, R. K., and J. C. Garland, Phys. Rev. B **33**, 7827 (1986).

Chang, W. H., IEEE Trans. Mag., **MAG-17**, 764 (1981).

Chung, J. S., K. H. Lee, and D. Stroud, Phys. Rev. B **40**, 6570 (1989).

Clark, T. D., Phys. Rev. B **8**, 137 (1973).

Clarke, J., and J. L. Paterson, Appl. Phys. Lett. **19**, 469 (1971).

Davidson, A., R. S. Newbower, and M. R. Beasley, Rev. Sci. Inst. **45**, 838 (1974).

De Gennes, P. G., Rev. Mod. Phys. **36**, 225 (1964).

Deutscher, G., and P. G. De Gennes, in *Superconductivity*, Vol. II, edited by R. D. Parks (Marcel-Dekker, New York, 1969).

Eikmans, H., and J. E. van Himbergen, "Dynamic Simulations of arrays of Josephson junctions," preprint (1990).

Falco, C. M., W. H. Parker, S. E. Trullinger, and P. K. Hansma, Phys. Rev. B **10**, 1865 (1974).

Fink, H. J., A. Lopez, and R. Maynard, Phys. Rev. B **26**, 5237 (1982).

Fiory, A. T., Phys. Rev. Lett. **27**, 501 (1971).

Forrester, M. G., unpublished doctoral thesis, Harvard University (1988).

Forrester, M. G., Hu Jong Lee, M. Tinkham, and C. J. Lobb, Jap. J. Appl. Phys. **26**, Suppl. 26-3, 1423 (1987).

Forrester, M. G., Hu Jong Lee, M. Tinkham, and C. J. Lobb, Phys. Rev. B **37**, 5966 (1988).

Free, J. U., S. P. Benz, M. S. Rzchowski, M.Tinkham, C. J. Lobb and M. Octavio, Phys. Rev. B **41**, 7267 (1990).

Giffard, R. P., R. A. Webb, and J. C. Wheatley, J. Low Temp. Phys. **6**, 533 (1972).

Gordon, James M., A. M. Goldman, J. Maps, D. Costello, R. Tiberio, and B. Whitehead, Phys. Rev. Lett. **56**, 2280 (1986).

Gordon, James M., A. M. Goldman, M. Bushan, and R. H. Cantor, Jap. J. Appl. Phys. **26**, 1425 (1987).

Granato, E., and J. M. Kosterlitz, Phys. Rev. B **33**, 6533 (1986).

Hadley, P., M. R. Beasley and K. Wiesenfeld, Phys. Rev. B **38**, 8712 (1988).

Hadley, P., unpublished doctoral thesis, Stanford Univiversity (1989).

Halperin, B. I., Phys. Rev. Lett. **52**, 1583 (1984).

Halsey, T. C., Phys. Rev. B **31**, 5728 (1985).

Halsey, T., "Giant Shapiro steps in Josephson junction arrays," preprint (1990).

Hansen, J. Bindslev, and P. E. Lindelof, Rev. Mod. Phys. **56**, 431 (1984).

Huggins, H. A., and M. Gurvitch, J. Appl. Phys. **57**, 2103 (1985).

Jain, A. K., K. K. Likharev, J. E. Lukens, and J. E. Sauvageau, Phys. Rep. **109**, 309 (1984).

Jaycox, J. M., and M. B. Ketchen, IEEE Trans. Mag., **MAG-17**, 400 (1981).

Josephson, B. D., Phys. Lett. **1**, 251 (1962).

Ketchen, M. B., IEEE Trans. Mag., **MAG-17**, 387 (1981).

Kimhi, D., F. Leyvraz, and D. Ariosa, Phys. Rev. B **29**, 1487 (1984).

Kosterlitz, J. M., and D. J. Thouless, J. Phys. C **6**, 1181 (1973).

Langer, J. S., and V. Ambegaokar, Phys. Rev. **164**, 498 (1967).

Laughlin, R. B., Phys. Rev. Lett. **50**, 1395 (1983).

Lee, K. H., D. Stroud, and J. S. Chung, Phys. Rev. Lett. **64** (1990) 962.

Lee, K. H., and D. Stroud, Bull. Am. Phys. Soc. **35**, 627 (1990).

Lee, K. H., J. S.Chung, and D. Stroud, workshop on Relaxation and Related Phenomena in Complex Systems, Torino, Italy, 1989, edited by A. Campbell and C. Giovannella (Plenum, New York).

Leeman, Ch., Ph. Lerch, and P. Martinoli, Physica **126B**, 475 (1984).

Leeman, Ch., Ph. Lerch, G.-A. Racine, and P. Martinoli, Phys. Rev. Lett. **56**, 1291 (1986).

Lobb, C. J., Physica **126B**, 319 (1984).

Lobb, C. J., private communication (1990).

Lobb, C. J., David W. Abraham, and M. Tinkham, Phys. Rev. B **27**, 150 (1983).

Lukens, J. E., A. K. Jain, and K. L. Wan, "Application of Josephson Effect Arrays for Submillimeter Sources," in *Superconducting Electronics*, edited by H. Weinstock and M. Nisenoff (Springer-Verlag, New York, 1989), p. 235.

Martinoli, P., O. Daldini, C. Leeman, and E. Stocker, Solid State Commun. **17**, 205 (1975).

McCumber, D. E., and B. I. Halperin, Phys. Rev. B **1**, 1054 (1970).

McCumber, D. E., J. Appl. Phys. **39**, 3113 (1968).

McWane, J. W., J. E. Neighbor, and R. S. Newbower, Rev. Sci. Inst. **37**, 1602 (1966).

Mon, K. K., and S. Teitel, Phys. Rev. Lett. **62**, 673 (1989).

Mooij, J. E., in *Percolation, Localization, and Superconductivity*, edited by A. M. Goldman and S. A. Wolf (Plenum, New York, 1983), p. 325.

Mück, H. M., H. Rogalla, and C. Heiden, private communication (University of Giessen, W. Germany, 1987).

Nori, Franco and Qian Niu, Phys. Rev. B **37**, 2364 (1988).

Nori, Franco, Qian Niu, Eduardo Fradkin, and Shau-Jin Chang, Phys. Rev. B **36**, 8338 (1987).

Nelson, D. R., and J. M. Kosterlitz, Phys. Rev. Lett. **39**, 1201 (1977).

Pannetier, B., J. Chaussy, R. Rammal, and J. C. Villegier, Phys. Rev. Lett. **53**, 1845 (1984).

Rammal, R., and G. Toulouse, Phys. Rev. Lett. **49**, 1194 (1982).

Rammal, R., T. C. Lubensky, and G. Toulouse, Phys. Rev. B **27**, 2820 (1983).

Renne, M. J., and D. Polder, Rev. Phys. Appl. **9**, 25 (1974).

Resnick, D. J., J. C. Garland, J. T. Boyd, S. Shoemaker, and R. S. Newrock, Phys. Rev. Lett. **47**, 1542 (1981).

Resnick, D. J., R. K. Brown, D. A. Rudman, J. C. Garland, and R. S. Newrock, in *Proceedings of the Seventeenth International Conference on Low Temperature Physics*, (1984) p. 739 .

Rubinstein, M., B. Shraiman, and D. R. Nelson, Phys. Rev. B **27**, 1800 (1983).

Russer, P., J. Appl. Phys. **43**, 2008 (1972).

Rzchowski, M. S., S. P. Benz, M.Tinkham, and C. J. Lobb, Phys. Rev. B, to appear (1990).

Santhanam, P., C. C. Chi, and W. W. Molzen, Phys. Rev. B **37**, 2360 (1988).

Shapiro, S., Phys. Rev. Lett. **11**, 80 (1963).

Shih, W. Y. and D. Stroud, Phys. Rev. B **32**, 158 (1985).

Shih, W. Y., and D. Stroud, Phys. Rev. B **28**, 6575 (1983).

Shih, W. Y., C. Ebner, and D. Stroud, Phys. Rev. B **30**, 134 (1984).

Simonin, J. M., C. Wiecko, and A. Lopez, Phys. Rev. B **28**, 2497 (1983).

Springer, K. N., and D. J. Van Harlingen, Phys. Rev. B **36**, 7273 (1987).

Stewart, W. C., Appl. Phys. Lett. **10**, 277 (1968).

Straley, J. P., Phys. Rev. B **38**, 11225 (1988).

Taur, Y., P. L. Richards, and F. Auracher, in *Low Temperature Physics-LT13*, Vol. 3, edited by K. D. Timmerhaus, W.J. O'Sullivan, and E. F. Hammel (Plenum Press, New York, 1974), pp. 276-280.

Teitel, S., and C. Jayaprakash, J. Physique Lett. **46**, L-33 (1985).

Teitel, S., and C. Jayaprakash, Phys. Rev. B **27**, 598 (1983)a.

Teitel, S., and C. Jayaprakash, Phys. Rev. Lett. **51**, 1999 (1983)b.

Tilley, D. R., Phys. Lett. **33A**, 205 (1970).

Tinkham, M., *Introduction to Superconductivity* (McGraw-Hill, New York, 1975; reprinted by Krieger, Florida, 1985).

Tinkham, M., David W. Abraham, and C. J. Lobb, Phys. Rev. B **28**, 6578 (1983).

Tinkham, M., and C. J. Lobb, "Physical Properties of the New Superconductors," in *Solid State Physics*, Vol. 42, edited by H. Ehrenreich and D. Turnbull (Academic, San Diego, 1989), pp. 91-134.

Van Duzer, T., and C. W. Turner, *Principles of Superconductive Devices and Circuits* (Elsevier North Holland, New York, 1981).

van der Zant, H.S.J., C.J. Muller, H.A. Rijken, B.J. van Wees, and J.E. Mooij, Physica B **152**, 56 (1988).

Vanneste, C., et al., J. Appl. Phys. **64**, 242 (1988).

Voss, Richard F., and Richard A. Webb, Phys. Rev. B **25**, 3446 (1982).

Webb, Richard A., Richard F. Voss, G. Grinstein, and P. M. Horn, Phys. Rev. Lett. **51**, 690 (1983).

Wilczek, F., Phys. Rev. Lett. **48**, 1144 (1982), and Phys. Rev. Lett. **49**, 957 (1982).

Xia, W., and P. L. Leath, Phys. Rev. Lett. **63**, 1428 (1989).

Zimmerman, J. E., and A. H. Silver, Phys. Rev. **141**, 367 (1966).

APPENDIX I

Niobium-Copper-Niobium SNS Array Fabrication Procedure

1) **Clean 1" sapphire substrates** with TCE, ACE, and METH in ultrasonic for 10 mins each.

2) Prepare Photoresist-Aluminum-Photoresist **trilayer** on substrates (see Forrester thesis, Technical Report No. 26).
   -spin Shipley 1400-27 @ 4000 rpm for 30 sec.
   -bake for 30 mins @ 100°C.
   -blanket expose entire substrate for 15 secs in Karl Suss mask aligner, using soft contact mode.
   -evaporate 500 Å of Al in an alumina boat (base pressure $P_B < 1x10^{-6}$Torr).
   -spin Shipley 1400-27 (or thinner) @ ≥4000 rpm for 30 sec.
   -bake for 30 mins @ 80-90°C.
   -expose bilayer (array) mask for 3.7 secs in Karl Suss (soft contact mode).
   -expose triangular current injection pads or other contact leads that are required.
   -develop fully (~1 min) in 5:1 H_2O:Microposit 351 Developer.
   -rinse thoroughly with H_2O bottle, and blow dry with dry compressed air or N_2.
   -etch Al until completely gone, and wait about 10-20 secs longer.
   -rinse in H_2O and blow dry thoroughly.
   -using *fresh* developer form undercut in bottom PR (~30 secs).
   -rinse in H_2O and blow dry.
   -back-etch Al in undercut, rinse H_2O and blow dry.
   -check under microscope for 1-3 μm undercut, and develop further if necessary.

3) **Copper evaporation**
   -mount sample on evaporator sample block and install in evaporator using insulating teflon sheet, and teflon screws. Connect wire from sample block to high-voltage feedthrough for application of rf. Check continuity and grounding before closing chamber.
   -place high-purity (99.999%) copper in large tungsten or molybdenum boat and mount in evaporator using the electrodes for copper.
   -make a small window in Al foil and pump chamber to $P_B < 2x10^{-7}$Torr (degas on).
   -**rf clean substrate.**
      -adjust Argon pressure in chamber to 15 mTorr (100mTorr foreline pressure).
      -attach rf matchbox and make sure 25 pF tuning capacitor is installed.
      -open shutter.
      -set forward power on rf supply to 12W.
      -tune loading inductor to minimize reflected power until it reads zero.
      -the dc self bias voltage on rf matchbox meter should read ~100 V.
      -turn off rf power after 5 mins and close shutter.
   -shut off Ar flow and pump out chamber again to $P_B < 2x10^{-7}$ Torr (degas on).
   -turn on thckness monitor and set density $\rho = 8.96$ gm/cm^3.
   -copper should melt ~8.5-9.5 A.

-boil off impurities for > 2 mins (≥300 Å total).
-turn current up to 15.5 A, wait 10 secs (≥1700 Å total).
-open shutter and zero thickness monitor simultaneously.
-evaporate 3500 Å, and then imediately turn off power supply.
-cool down with shutter open.
-remove sample and mount directly in magnetron sputtering system.

4) **Niobium sputtering** (see Fig. 2.4)
-cover Al magnetron target with foil and shutter.
-make sure divider shield is installed on cold shroud.
-mount substrate using stainless steel substrate clamp with 1" square hole, making certain that substrate is in good thermal contact with copper block (no sliding).
-mount 1-5/8" diam. (small hole) dark space shield ~1/4" from substrate and make certain that shield and substrate holder are not electrically shorted.
-pump chamber to $P_B < 1.5 \times 10^{-7}$ Torr (degas on and liquid N_2 trap filled).
-make sure that **cooling water** is flowing to sample holder and appropriate magnetrons.
-start liquid N_2 flowing through cold shroud, P_B should drop to $\leq 6 \times 10^{-8}$ Torr (with degas off).
-rotate substrate above Aluminum target position.
-start Ar flow (35 sccm), adjust gate valve until chamber pressure reads 6 mTorr.
-connect magnetron cathode to high voltage supply and connect chamber ground.
-increase rheostat until voltage reads 500 V.
-drop diffusion pump 'flap' to increase chamber pressure until plasma ignites.
-optimum **sputtering** parameters are: 6 mTorr Ar, and 150 mA @ 500 V .
-dc clean target and getter chamber for a total of 15 mins.
-after 8 mins, begin **rf Ar ion etching** of substrate over the Al target with rf power on and off for 1min intervals, for a total of 4 mins etching time (see Fig. 2.5).
-optimum rf etching parameters are 600 V dc self bias voltage, 23 W forward power (0-1 W reflected power), using 75 pF tuning capacitor in matchbox.
-at the 15 min mark, imediately turn off rf power, rotate substrate over niobium target, remove matchbox and ground substrate, all as *quickly* as possible.
-sputter niobium onto substrate for 10 mins (rate is ~ 200 Å/min).

5) **Lift off** in acetone, 10-30 mins.
-ultrasonic 1 min in fresh acetone.
-ultrasonic 2 min in methanol.
-blow dry.

6) **Clean masks.**
-rinse masks with PGMEA and methanol, and blow dry.
-if necessary, clean masks in outer room hood using *Piranha* bath {3:7 solution of 30% H_2O_2 (Hydrogen Peroxide): Sulfuric Acid (conc.)}.

7) **Inverting photoresist.**
***important note**: Shipley 1400 series PR is incompatible with Hoechst AZ PR. The solvent for the AZ resist is propylene glycol monomethyl ether acetate (PGMEA) not acetone. (=> use only specially marked 'AZ' beakers and clean up with PGMEA). The AZ resists are also excellent non-inverting resists; just skip the inverting steps below.
-spin Hoechst AZ-5214E photoresist 4000 rpm for 30 secs (~1.4μm thick).
-bake for 30 mins @ 90°C.
-expose array mask for 3.7 sec in Karl Suss.

-for superconducting bus bars and contact leads, expose the pad mask next.
-for normal metal contact leads and triangular current injection pads, expose these regions individually by blanking-off the array with the 'half chrome' mask. (We want these regions to be protected by inverted photoresist while the Nb islands are formed to ensure array uniformity).
-inverting steps:
  -bake 1" sapphire substrate in oven for 4 min @ 120°C (70 secs for 2" Si wafers).
  -blanket expose for 90 secs in Karl Suss (soft contact mode).
-develop 75 secs with Hoechst AZ-422MIF for inverting process (developing time for noninverting PR is longer, ~3 min).
-rinse very thoroughly with H_2O and blow dry.

8) **Reactive ion etch** (RIE).
-mount in old RIE chamber using Si spacers between clips and substrate.
-make sure that **cooling water** is flowing to sample holder/cathode.
-pump chamber to < 100 mTorr and vent to near atmosphere with dry N_2.
-Repeat pump and vent three times.
-flow SF_6 15 min (full scale) and set gas correction factor to read 14 sccm full scale.
-connect rf matchbox and make sure 25 pF tuning capacitor is installed (see Fig. 2.5).
-set flow rate to 13 sccm (~180 mTorr in chamber).
-set rf power level to 44 W.
-turn on rf power and tune matchbox to minimize reflected power (typically only 1 W).
-matchbox self-bias voltage should read ~30 V.
-RIE for 4-5 mins (Nb etch rate ~750 Å/min, SiO etch rate ~250 Å/min).
-turn off rf and SF_6 gas flow.
-vent and pump with dry N_2 three times and then vent to atmosphere.
-remove sample and pump down chamber.

9) **Strip photoresist**
-put substrate in beaker with Hoechst AZ-300T stripper.
-place beaker on hot plate and heat to 70-80°C (low setting).
-strip for 25-30 mins and then ultrasonic briefly, 1-2 mins.
-rinse with H_2O and blow dry.

10) Complete **Normal metal contact pads and leads.**
-repeat processing steps 7-9 above, with the following exceptions:
  -expose only the Nb on the pads and leads with the 'half-chrome' mask.
  -skip inverting steps (post-expose bake and blanket expose) for noninverting process.
  -RIE until Nb on pads and leads are visibly removed (~90 secs).
  -remove PR with PGMEA if possible and skip ultrasonic steps.

APPENDIX II

DC SQUID Fabrication and Application as a Sensitive Voltmeter

The motivation for developing dc SQUID (superconducting quantum interference device) fabrication technology in our lab was to make a highly-sensitive pico-voltmeter for measuring 2D arrays very close to their phase transition temperature. The voltmeter must be sensitive because the arrays have low resistance and because very small bias currents must be used to minimize the current unbinding of the vortex pairs. With the advent of thin-film fabrication technology, dc SQUIDs can now be fabricated with two nearly identical junctions and noise sensitivities approaching the quantum noise limit, thus making them ideal devices for constructing such a voltmeter. We will briefly describe some of the important considerations for making dc SQUIDs into useful and sensitive devices, followed by a brief description of our fabrication process and the SQUID voltmeter.

A. DC SQUID Design

A dc SQUID is a device made of two Josephson junctions in parallel so that it can be dc current biased, as opposed to an rf SQUID that must be coupled to inductively. The dc SQUID is essentially a flux to voltage transducer, where a changing magnetic field through the area between the junctions will result in a change in the voltage across the SQUID. The SQUID is sensitive to extremely small changes in magnetic field as a result of fluxoid quantization around the superconducting loop formed by the two junctions, thus making them excellent magnetometers. The first high-performance thin-film planar dc SQUIDs were made by Jaycox and Ketchen (1981) using IBM's Nb-Pb edge-junction technology. The advantages of these dc SQUIDs over previous point contact SQUIDs are better

junction uniformity and the ability to fabricate an input coil that is very 'closely-coupled' to the SQUID 'washer' that forms the superconducting loop between the junctions. Most dc SQUIDs, including our own, are now modelled after this design.

There are three interdependent quantities that must be adjusted in order to tune a dc SQUID to its optimum sensitivity (see Ketchen, 1981): (1) the McCumber parameter, $\beta_c = 2ei_cr_n^2C/\hbar$ (see Section 1.2), (2) the ratio of the geometrical inductance of the washer, L, to the Josephson inductance, $\beta_L = L/\pi L_J = 2i_cL/\Phi_0$ (see Section 2.3), and (3) the intrinsic (coupled) energy sensitivity of the SQUID due to white noise, $\varepsilon_w = hkT/ei_cr_n l^2$, where $l^2 = M^2/L_iL$. M is the mutual inductance between the input coil and the SQUID washer, and L_i is the self inductance of the input coil. With the closely-coupled input coil arrangement discussed above, the coupling to the dc SQUID is excellent, giving values of $l^2 \geq 0.9$ (see Jaycox and Ketchen, 1981). The two junctions in the dc SQUID should be overdamped ($\beta_c \leq 1$) so that they are not hysteretic and the i-v curves are single valued. The parameter β_L determines the maximum current modulation depth of the dc SQUID with magnetic field (see Van Duzer and Turner, 1981, pp. 206-213). It has been shown (Zimmerman and Silver, 1966, and Clarke and Paterson, 1971) that the SQUID is most sensitive when its modulation current is $\approx$ 50% of its maximum current ($2i_c$) and that this occurs when $\beta_L \approx 1$.

Thus, with l^2 determined by the coupling configuration, the sensitivity of the dc SQUID can approach the quantum limit, $\varepsilon_w \approx h$, at a given operating temperature, by choosing ei_cr_n larger than kT. The trick to all of this is to fabricate junctions with large i_cr_n, while keeping them non-hysteretic and, at the same time, fixing $\beta_L \approx 1$. The critical current and capacitance of the junctions are generally determined by the fabrication technology (the minimum area of the junctions and the oxidation time of the tunnel barriers), so that β_c is finely tuned by placing external shunt resistors across each of the junctions. We can adjust $\beta_L \approx 1$ by fabricating a SQUID washer with a certain hole diameter, *d*, since Chang (1981) has shown that $L \approx 1.25\mu_0 d$ (see also Jaycox and Ketchen, 1981).

B. DC SQUID Fabrication

These planar dc SQUIDs are the most complicated devices made in our lab, requiring five separate mask patterning steps and all of the latest fabrication technologies (RIE, Nb sputtering, *etc.*) that we have available. We originally made our own dc SQUID masks using our electron-beam patterning facility, but with the limited field of view we could only make masks for a single device. The masks that we now use are copies of those used by Mück *et al.* (1987) for making Nb-Nb_2O_5-Pb dc SQUIDs, and can make ~16 usable devices on a 2"-diameter Si wafer. The washers for these SQUIDs have L ~ 300-600pH, thus requiring a critical current for each junction i_c ~ 1-3μA. A schematic diagram of the thin-film layers required to make a dc SQUID are shown in Fig. AII.1. The junctions are defined by the 2.5μm-diameter holes in the SiO insulating layer. We chose to develop an all-refractory Nb junction technology with artificial aluminum-oxide barriers (Nb-Al_2O_3-Nb), because Nb junctions are more robust than Pb junctions and Al_2O_3 is now known to be a much better junction barrier than Nb_2O_5 (Huggins and Gurvitch, 1985). We will briefly describe the fabrication steps below. Please refer to the array fabrication procedure in Appendix I for various details on Nb sputtering, RIE, rf Ar-ion etching, and inverting photoresist techniques.

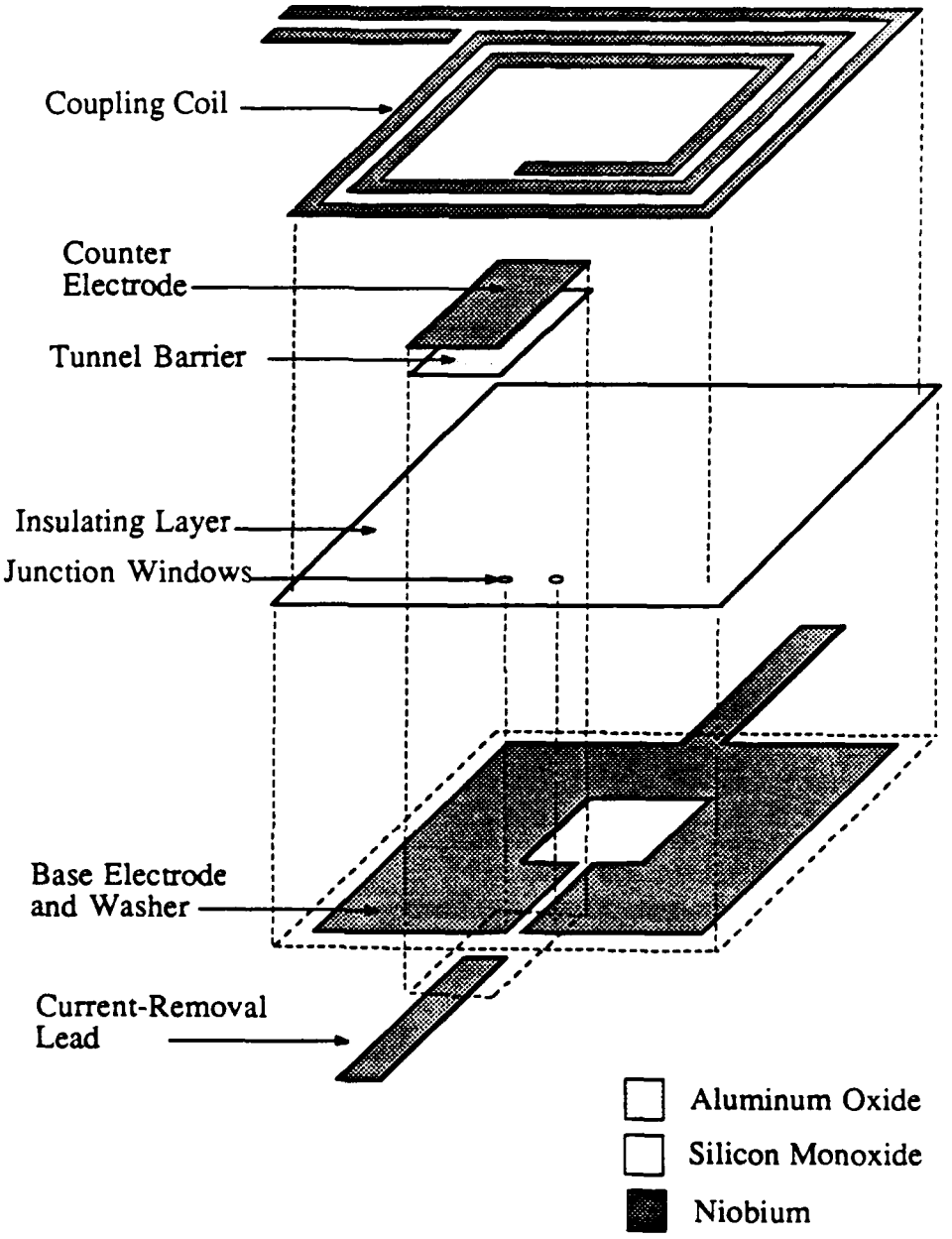

Fig. AII.1. Planar thin-film dc SQUID schematic, showing four of the five mask steps for making a complete SQUID with a close-coupled input coil. (The missing step is the first step which defines the $Cu_{.6}Au_{.4}$ shunt resistors.) The Nb-Al_2O_3-Nb junctions are vertical 'sandwich' junctions defined by the 2.5μm-diameter windows in the SiO, where the first Nb layer that forms the SQUID washer also serves as a base electrode. The Al_2O_3 tunnel barrier and Nb counter electrode that complete the junction are formed sequentially in the magnetron sputtering machine during the same (final) pump-down step in order to ensure junction reproducibility.

C. DC SQUID Fabrication Procedure

1) **Clean** a 2" Si substrate with TCE, ACE, METH in ultrasonic for 10 mins each.

2) **$Cu_{.6}Au_{.4}$ Shunt resistors.**
   -**Chlorobenzene photoresist undercut technique** (Mück *et al.*, 1987).
      -spin Shipley 1450J for 30 sec @ 6000 rpm.
      -bake for 20 mins @ 65°C.
      -cool wafer ≥ 1 min.
      -soak in chlorobenzene for 10 mins (be careful not to breathe it!).
      -bake for 10 mins @ 65°C.
      -expose U-shaped resistor mask in Karl Suss for 15 secs
      (blank off the other patterns on the mask with the black negative).
      -develop 30-60 secs (as short as possible for the best resolution).
      -rinse thoroughly in H_2O.
      -check under microscope for 0.5-1.0μm undercut.
   -evaporate 60% Cu and 40% Au (by weight) in evaporator (ρ = 13.10 gm/cm^3), using the W or Mo wire coils. Each shunt resistor should be ~1-10Ω (note that 500Å gives a resistivity ~ 10μΩ-cm).
   -lift off in acetone.

3) **Nb Base electrode, washer and pads.**
   -This Nb level can either be formed by RIE or with a lift-off process, since we have masks of either sign. We will describe the lift-off process using the RIE mask and a negative photoresist, because the RIE mask is a better copy of the original (the regular mask is not as good because the gap in the washer slit is larger (> 10μm) than the junction window spacing) and because lift off is simpler than RIE.
   -prepare inverting photoresist AZ-5214E (see Appendix I) and align the RIE mask so that the L-shaped CuAu alignment marks are at the corners of the washer. The U-shaped resistor should contact both the washer and the current-removal lead on all the SQUID devices on the wafer. Expose and process using the inverting steps described in Appendix I.
   -sputter 1000-2000Å of Nb (see Appendix I)
   -lift off in PGMEA.

4) **SiO Insulating layer and junction window.**
   -prepare Shipley photoresist 1400-28 (or -30) and spin at 4000-8000 rpm for a thin layer. Do not use an undercut.
   -expose the SiO insulating layer mask, aligning the windows to the corners of the washer (on the inside edges of the washer slit) and develop.
   -rf clean the substrate 5 mins in the evaporator (see Appendix I) before evaporating 1000Å of SiO (ρ = 2.13 gm/cm^3) from a 'chimney' chamber. Make sure that all of the SiO powder is in one compartment and that its chimney is capped.
   -remove from chamber and inspect for pin-holes in the SiO (We have had problems with the SQUID input coil shorting through the SiO to the washer. Breaking vacuum and evaporating another layer fills the pin-holes).
   -evaporate another 1000Å of SiO (Note that the complete SiO layer should be thicker than the Nb base electrode/washer layer).
   -lift off in acetone.

5) **Nb Close-Coupled coil.**

-prepare a thin layer of photoresist as described in (4) above and expose the 50-turn 'close-coupled' input coil, blanking off the other patterns on the mask with the black negative. The coil leads on this mask must contact the outgoing leads (that go to the pads) as well as the windows in the SiO layer that allow contact to the Nb strip in the washer slit. This strip completes the coil circuit by bringing the inner winding of the coil back to the outside where it can connect to the pad leads.
-sputter 1600Å of Nb (~ 8 mins).
-lift off in acetone.

6) **Al_2O_3 Barrier formation and Nb counter electrode deposition.**

-prepare photoresist with an undercut using the chlorobenzene technique described above in (2).
-expose counter electrode mask (again blanking off the unwanted patterns with the negative) and develop. The counter electrode should be aligned to cover the windows in the SiO layer and make contact to the current-removal lead.
-mount sample on water cooled sample holder in sputtering chamber (make sure that both Nb and Al magnetrons are uncovered and have H_2O cooling).
-rf Ar-ion etch at a self-bias voltage of $600V_{dc}$ (on match box), for 4 mins total at 1 min intervals (see Appendix I) to remove the Nb-oxide that formed in the windows.
-immediately sputter 50-100Å of Al from the Al magnetron (80 mA @ 500V gives a rate ~ 120Å/min).
-oxidize the Al to create the tunnel barrier by closing the gate valve and filling the chamber with pure O_2. By varying the oxidation time and pressure the critical current of the junctions can be tuned. We typically used 1 hour @ 1 Torr. It is also possible to create a controlled oxide barrier with an rf plasma using the 5% O_2-95% Ar *(mixture) cylinder.*
-pump out the oxygen with the roughing pump and then pump the chamber back down to its original base pressure with the diffusion pump.
-dc clean the the Nb target thoroughly and then sputter 2000Å Nb.
-lift off.

6) Spin a protective layer of photoresist on the wafer and then dice or saw it into the 7 x 10mm dc SQUID chips. Remove the photoresist with acetone. The dc SQUID chips are now complete.

Photographs of a completed dc SQUID made in our lab using the above process are shown in Figs. AII.2 and AII.3. We have just finished developing this fabrication process. The SQUIDs have yet to be finely tuned for optimum sensitivity by adjusting the thickness of the resistors and the oxidation parameters for the junction barriers.

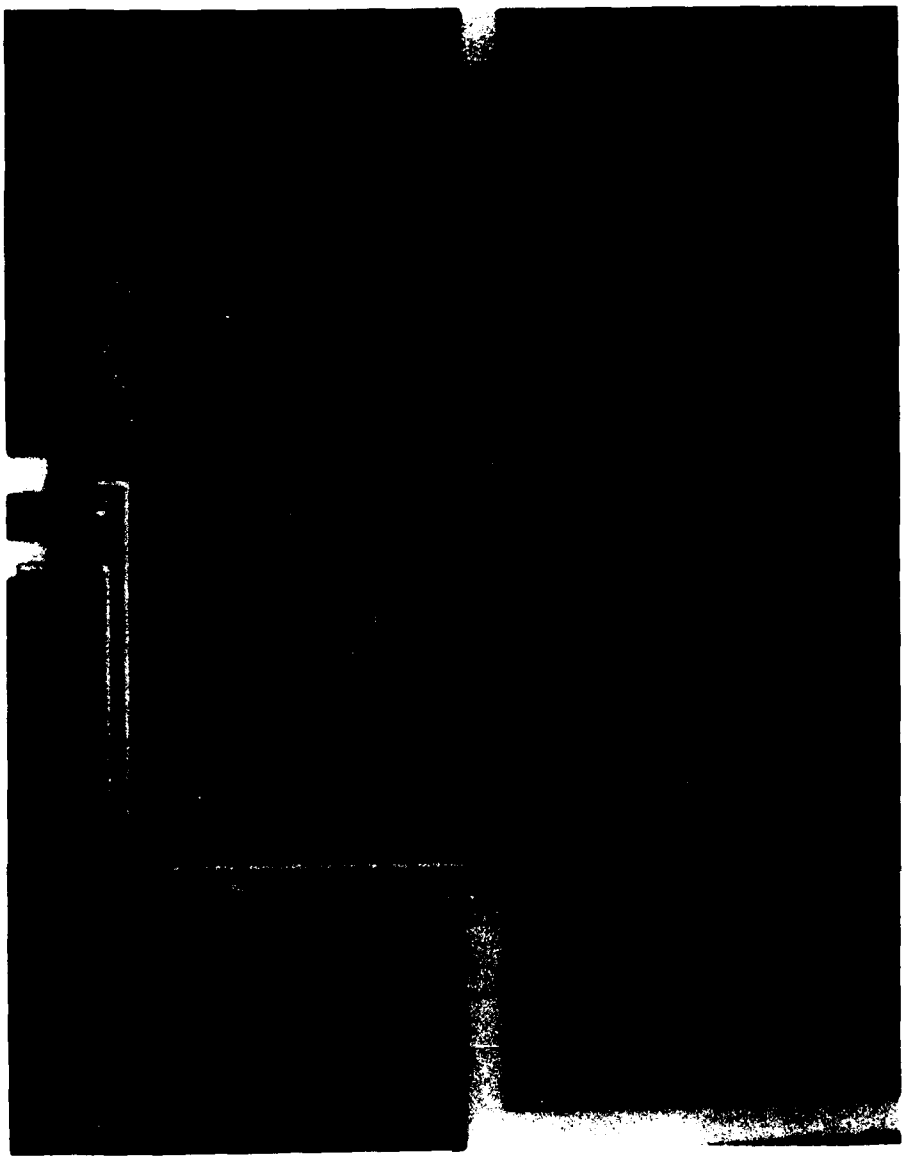

Fig. AII.2. Top view of a completed Nb-Al_2O_3-Nb junction dc SQUID. The 50μm-wide Nb at the top and bottom are the current-bias leads. The dark square (180μm on a side) in the center is the hole in the SQUID washer. The 50-turn Nb close-coupled input coil (with 2.5μm pitch) lies on top of the SQUID with its current leads entering and exiting on the left. The two junctions, one on either side of the washer slit, and the counter electrode are at the bottom edge of the washer (a blow-up of the junction region is shown in Fig. AII.3). The input coil leads (center left) and the current bias leads (top and bottom) eventually connect to large (1x2mm) contact pads on the SQUID chip (see Fig. AII.5). The curvature at the edges of the picture and the dark spots at the top and right are due to the microscope optics.

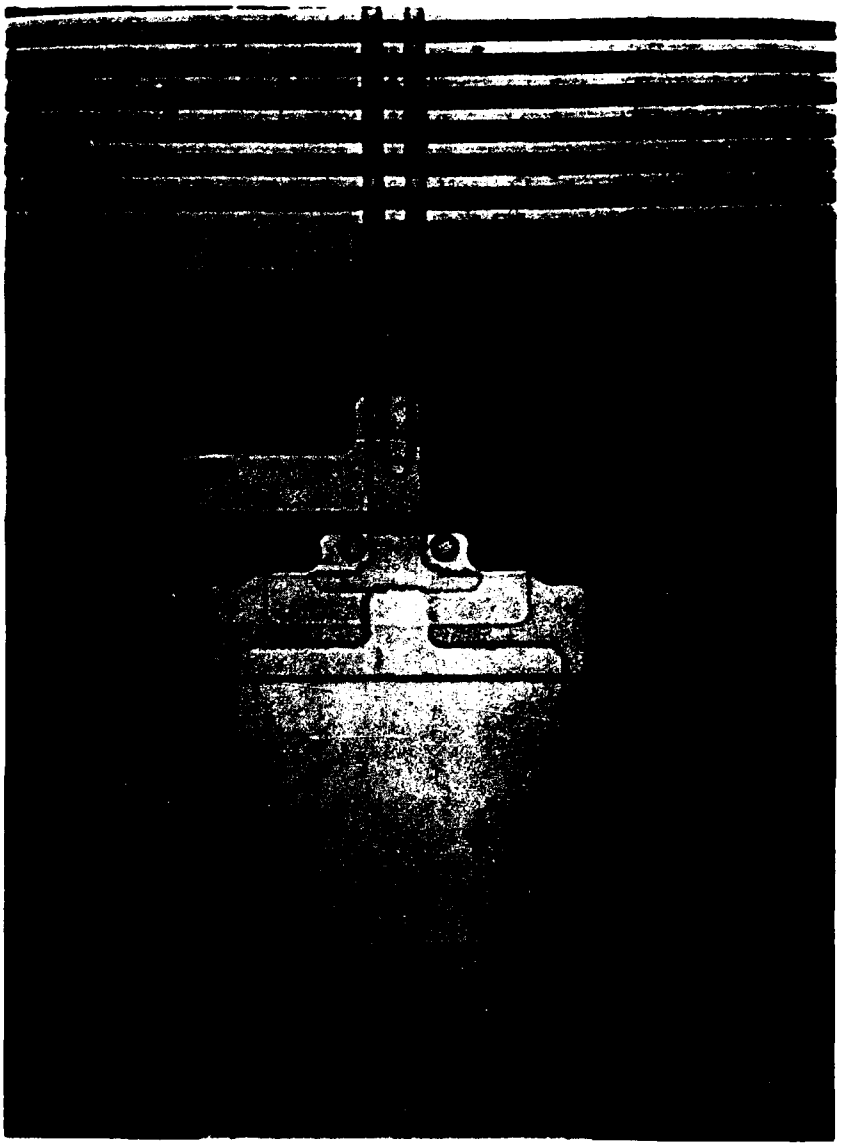

Fig. AII.3. Close-up of junction region of one of our dc SQUIDs. The 2.5μm-diameter (circular) windows that define the Nb-Al_2O_3-Nb junctions are seen in the center of the picture. The counter electrode connects to the junction windows and the slightly narrower current removal lead at the bottom. The outline of the U-shaped $Cu_{.6}Au_{.4}$ layer that forms the two shunt resistors can be seen connecting the bottom edge of the washer to a tap extending up from the current-removal lead. Part of the outer six turns of the 50-turn input coil (with 2.5μm pitch) can be seen at the top of the photograph. The vertical 4μm Nb strip, that connects the inside of the coil back to the outside, can be seen lying in the 10μm-wide slit of the washer and connecting to the horizontal 10μm-wide Nb lead through a window in the SiO layer.

D. DC SQUID Voltmeter

The design of our dc SQUID voltmeter is modelled after the rf SQUID voltmeter used by McWane *et al.* in 1966 (see also Giffard *et al.*, 1972, and Davidson *et al.*, 1974). We have modified this design for dc SQUIDs by incorporating the 100kHz flux-locked-loop (FLL) electronics used by Clarke *et al.* (1976). The circuit design of the FLL electronics that we use was provided by Mück *et al.* (1987), but built in our lab. A simple schematic of the complete voltmeter with electronics is shown in Fig. AII.4. When the SQUID is current biased, somewhere near $I_{bias} \approx 2i_c$, the change in its voltage as a function of flux (V-Φ) is a maximum. This V-Φ curve will be nearly sinusoidal (for SQUIDs with identical junctions), having maxima and minima when $\Phi = n\Phi_0$ and $(n+1/2)\Phi_0$, respectively (see Clarke *et al.*, 1976, or Ketchen, 1981). If a 100kHz modulation (amplitude $\sim\Phi_0/4$) is applied to the SQUID when it is biased exactly at one of these extrema (through the external modulation coil), the voltage across the SQUID will oscillate at 200kHz with no component at 100kHz (see Clarke *et al.*, 1976). If the voltage across the array (or any other sample to be measured) is changed so that it is different from the voltage across the standard resistor, R_S (see Fig. AII.4), then an error current, I_e, will flow through the close-coupled input coil on the SQUID chip. This changes the flux through the SQUID away from the extrema, so that the voltage across the SQUID now has a component at 100kHz. This signal is detected by a 100kHz resonant input circuit and then lock-in detected through the two amplifiers and the mixer. The output of the mixer will be proportional to the amplitude of the detected 100kHz signal. If the negative-feedback loop is closed, the current through the standard resistor will increase until the error current goes to zero. This negative-feedback loop through the dc SQUID forces the SQUID to lock to the original value of flux through the SQUID, *i.e.* one of the extrema, $n\Phi_0$ or $(n+1/2)\Phi_0$, originally set by the external modulation coil. The current through the feedback resistor, R_F, will be proportional to the change in the magnetic field through the SQUID, and thus

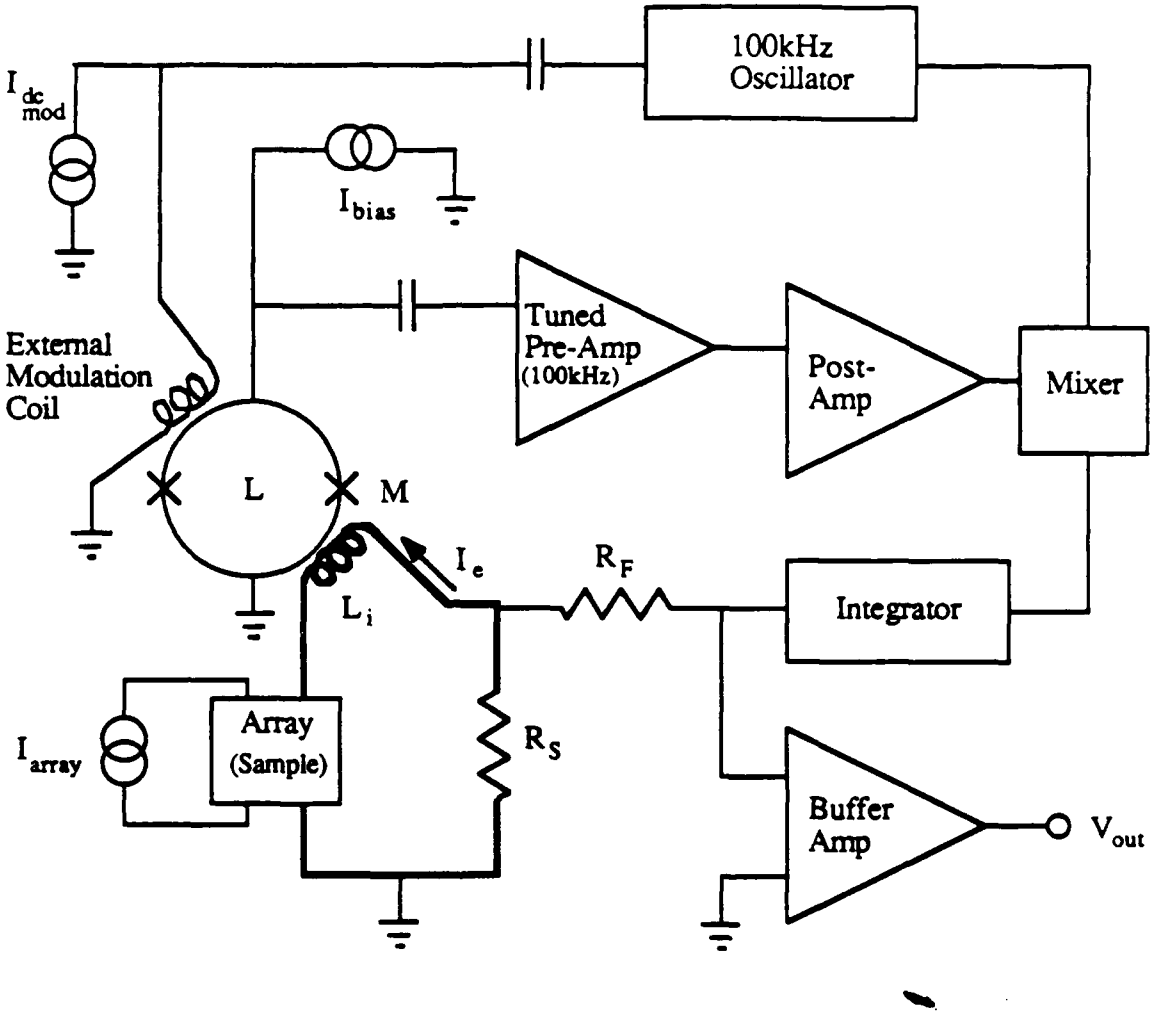

Fig. AII.4. DC SQUID voltmeter schematic, using flux-locked loop (FLL) electronics. The array is in a superconducting bridge circuit (bold line) with the 'close-coupled' input coil (L_i) and the standard resistor, R_S. The SQUID is kept at a constant dc current bias, but a constant offset field (from $I_{dc\ mod}$) with a 100kHz ripple (with amplitude $\sim\Phi_o/4$) is coupled to the SQUID through the external modulation coil. The offset field adjusts the flux in the SQUID so that its voltage is at an extremum, $n\Phi_o$ or $(n+1/2)\Phi_o$. The tuned amplifier detects a 100kHz signal when the flux from the bridge circuit $L_iI_e \neq 0$. The FLL electronics tries to keep the voltage across the array equal to the voltage across R_S by sending a feedback current through the feedback resistor, R_F, whenever the error current, I_e, is nonzero. When the flux through the SQUID is locked (I_e=0), the the voltage across R_F, as measured by the buffer amplifier, is proportional to the change in the array voltage.

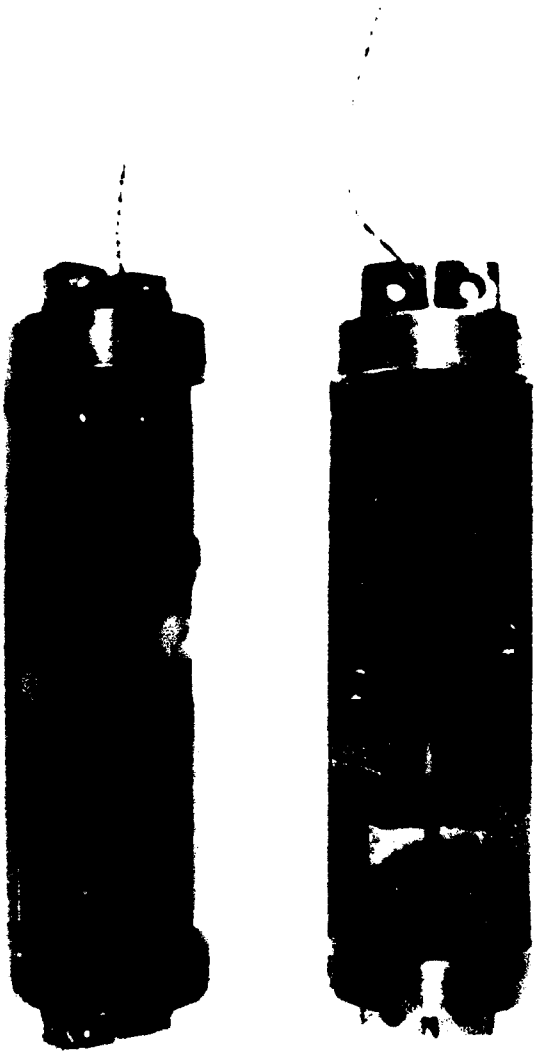

Fig. AII.5. Two copper 'slugs' that mount in the modified SHE (now BTI, Inc.) rf SQUID probe for our dc SQUID voltmeter. One of the completed 7x10mm dc SQUID chips is mounted in the left slug with Teflon bolts. The SQUID current-bias leads (which are also the voltage leads) are Al-wire bonded to a pair of copper bars, which will be attached to wires in the SQUID probe with the brass bolts at the bottom. The two pads at the top of the Si chip are connected to the close-coupled input coil. These pads will be (although not shown) connected to the pair of Nb bars at the top of the slug with superconducting wire, using the brass bolts on the Nb bars and either indium dots or superconducting solder on the chip. The copper external modulation coil lies under the SQUID chip inside a slot in the slug, as seen in the right slug. Its twisted pair of wires emerges from the top of the slug, exiting above the Nb bars.

proportional to the change in voltage across the array. The negative feedback also provides the high input impedance that is essential for the voltmeter. (See Giffard *et al.*, 1972, for various calculations of the input impedance and gain of the voltmeter circuit.)

We have modified an rf SQUID voltmeter probe (SHE Corp., now BTI) for use with our dc SQUID voltmeter, because it already has an internal low-resistance standard resistor ($R_S \approx 30\mu\Omega$) and a superconducting Nb shield. This entire probe mounts in an array measurement rig similar to the one described in Section 2.2. The dc SQUID chip is mounted on a copper 'slug' (see Fig. AII.5) where the close-coupled coil is connected to two Nb bars through superconducting wires and the external modulation coil lies directly beneath the SQUID washer. The slug is mounted in the original rf SQUID slug chamber where it is enclosed by the Nb shield. The current-bias leads to the SQUID and the external modulation coil are connected to existing (slightly modified) wiring in the probe that is then attached to the room temperature FLL electronics. The close-coupled coil is connected to the existing standard resistor at the bottom of the probe and to the array through superconducting wires to avoid thermal emf's that would cause unwanted error currents. Since the standard resistor must be small (see Giffard *et al.*, 1972) it is very important to minimize the contact resistance to the standard resistor. By using the already optimized circuit connections to the existing standard resistor from the rf SQUID probe we do not have to worry about this potential problem, because all the other connections are made between superconductors using pressed-contacts on Nb bars or with indium dots and solder.

ACKNOWLEDGEMENTS

I would like to express my appreciation to the professors, colleagues, and friends who have supported my research and who have made my years of graduate study at Harvard a stimulating and enjoyable experience.

I am fortunate to have had two superb mentors during my graduate career. I am very grateful to Prof. Michael Tinkham for taking me into his group during my very first semester, thus allowing me to immediately begin pursuing my interests in superconductivity. His managing style provided me with the best possible environment for my growth as a physicist. He allowed me to work freely and independently on projects of my choice, while providing me with financial support and excellent research facilities. His depth of physical insight and intuition were very helpful when we began to interpret the experimental results. Prof. Christopher J. Lobb was responsible for much of my development and direction towards a thesis project. I am greatly indebted to him for encouraging me to work on 2D arrays and for suggesting that there may be some interesting physics in them at high frequencies. Chris is one of the best teachers with whom I have had the privilege to work, and has been a great friend and an inspirational force during these past years. Without his day-to-day advice and reassuring words, I would not have had the confidence and persistence to have discovered the fractional giant steps.

Martin Forrester is responsible for peaking my interest in 2D arrays and for designing and making many of the array masks. I thoroughly enjoyed our collaborations on the disordered array simulations, and thank him for the many helpful and demystifying discussions. Horst Rogalla was instrumental in the design and construction of the magnetron sputtering system. His expertise in fabrication and other technical advice were

invaluable to my understanding sputtering and reactive ion etching and to developing these technologies in the lab.

Mark Rzchowski has been a very helpful collaborator and I have greatly benefited from our many discussions on arrays. It was a real pleasure to work with John Free, as we used his program to simulate the fractional giant steps in record time. I thank Charlie Johnson and Marco Iansiti for teaching me 'the ropes' when I joined the group. I am grateful to Walter Smith for always being available to lend a helping hand and for the friendly atmosphere that he instilled in the group by initiating the Friday party. I thank Gabe Spalding for his advice and suggestions regarding my questions about materials and characterization techniques. Many thanks go to Li Ji and Tom Tighe for their generous help around the lab and for those late-night nitrogen fills. I thank Lydia Sohn for helping me keep my sense of humor during the past months, and for her fabulous cooking.

I had a number of helpful discussions about the rf properties of junctions with Miguel Octavio, and am grateful to him for clearing up my confusion with factors of 2 in the steps widths. Bob Westervelt, Paul Sokol, David Vanderbilt and Bob Mead deserve many thanks for sharing their computer time and for their support of the Apollo network. Louis DeFeo masterfully turned my drawings, and sometimes only verbal descriptions, into beautiful and useful instruments. Most of the sputtering machine parts are credited to his handiwork and machining expertise. Ralph Generazzo and Bob Graham were each a tremendous help in purchasing the new RIE system. Elizabeth Hemingway's Thursday teas were always a welcome break towards the end of the week.

Finally, I would like to thank my family. I am deeply grateful to my parents for their many years of unconditional support and confidence in me. This work is dedicated to them. I thank my wife Elizabeth for her continued love, support, .nd understanding, even during my busy, and occasionally nocturnal, research hours. My brother Steve has also been a source of strength during these years.

This research was supported in part by National Science Foundation Grant Nos. DMR-84-04489, DMR-86-14003 and DMR-89-12927, Office of Naval Research Grant No. N00014-89-J-1565, and Joint Services Electronics Program Grant No. N00014-89-J-1023. I am also very grateful for a fellowship from the R. J. McElroy Trust during my first three years.